D6.5 - Design guidance on the use of shared moorings in compact arrays

DATE: June 2018

PROJECT COORDINATOR:

WavEC Offshore

GRANT AGREEMENT NR: 641334

PROJECT: WETFEET

The WETFEET – Wave Energy Transition to Future by Evolution of Engineering and Technology project has received funding from the European Union's Horizon 2020 programme under grant agreement No 641334.

Design guidance on the use of shared moorings in compact arrays			
Project	WETFEET – Wave Energy Transition to Future by Evolution of Engineering and Technology		
WP No.	6	WP Title	Array Breakthrough: Sharing Moorings (and Electrical Cables)
Deliverable No.		6.5	
Nature (R: *Report*, P: *Prototype*, O: *Other*)		R	
Dissemination level (PU, PP, RE, CO)		PU	
Lead beneficiary:		University of Plymouth	
Contributing partners		UOP, IST, INNOSEA, Aurora Ventures	
Authors List:		Keri Collins (UoP) Ben Howey (UoP) Deborah Greaves (UoP) Martyn Hann (UoP) Gregorio Iglesias (UoP) Rui Gomes (IST) Violette Harnois (Innosea)	
Quality reviewer		Peter Fraenkel	
Status (F: final; D: draft; RD: revised draft):		F	
Due Delivery Date:		31/12/2017	
Actual Delivery Date:		11 June 2018	

Version no.	Dates and comments
1	Mar-2017 Deliverable structure defined
2	Jun-2017 Flexible results added
3	Nov-2017 Rigid results added
4	Mar-2018 PF initial review
5	11-Jun-2018 Revised and submitted

Contents

Figures

Tables

EXECUTIVE SUMMARY

Deliverable 6.5 of the WETFEET H2020 project, Design guidance on the use of shared moorings in compact arrays, reports on the physical modelling and experimentation that was undertaken as part of Work Package 6. The goal of Work Package 6 as a whole was to examine the pros and cons of the sharing of mooring and anchor infrastructure in wave energy converter (WEC) arrays.

As part of D6.5, physical modelling of two types of WEC was used to examine inter-mooring strategies of WEC arrays at 1:40 scale. The first type of WEC was an oscillating water column (OWC) designed to be rigidly fixed to a common platform housing five sub-units. These sub-units were arranged in a die format and rigidly fixed to each other with a spacing between the centres of the central and a corner device of 1.5 times the diameter of a sub-unit. The baseline comparison for this array was a single, isolated sub-unit and heave plate. Four catenary moorings were used to secure both the isolated device and the array.

The second type of WEC was a floating OWC, also arranged in a five-device array but with a spacing of ~9.5 times the diameter between the centres of the central and corner devices. There were two baseline conditions for this: an isolated device at the same position as the central device of the arrays and an array of five individually moored devices. Three interconnected configurations were tested, each with the same device geometry but with different numbers of bed lines and interconnecting lines. Bed mooring lines for the flexibly interconnected arrays were hybrid designs; a catenary portion was connected to the anchor, connected to a synthetic fibre line that incorporated floats and clump weights before attaching to the devices. Interconnecting lines were synthetic fibre lines with clump weights attached to their centre points.

Capture width ratios (CWRs) were used to assess the performance capabilities of both types of array (referred to as the rigid and flexible arrays) in regular and irregular waves based on the wave climate at Leixões, off the coast of Portugal. In regular waves, the CWRs of the rigid array sub-units were generally higher than those of the isolated device, although this was dependent on the frequency of the incident waves. The CWRs were shown to be affected by the positions of the device in the array, with the front row having larger CWRs than those at the rear and the central device. In irregular waves, the CWRs of the rigid array were larger than five times those of the isolated device for three of the four irregular sea states tested (and were the same for the final sea state) with an increase in total array CWR of between 0.032 and 0.042, which was between a 31% and a 64% increase on five times the isolated device CWR. Again clear differences were seen in the CWR of the sub-units with the front row outperforming the central device.

Extreme sea states were used to examine the mooring line loading and motions of the arrays. While there were large surge and pitch motions associated with the extreme sea states, the largest line load was ~30 N for one of the front bed lines (1920 kN full scale) and ~10 N for the rear lines (640 kN).

The CWRs of the flexible arrays were very similar to each other in regular waves. There was a shift in the peak frequency from around 0.62 Hz for the individually moored array to around

0.7 Hz for the interconnected arrays. At their respective peaks, the CWRs were ~0.25 for the individually moored array and in excess of 0.50 for the sum of each flexible interconnected array. There was evidence of a basin effect at 0.63 Hz that was prevalent throughout the regular wave results, which caused lower values of motions, CWRs and loads. Heave magnitude and phasing with respect to the incident waves was shown to be a good predictor of the CWR.

In irregular waves, the flexible interconnected arrays had larger CWRs than five times the isolated device and the sum of the individually moored array for all sea states tested. CWR values in regular and irregular waves were found to be comparable and so the capture width curves from the regular wave experiments were used along with the Leixões wave probability matrix to estimate annual yield of a full-scale array of five devices. The individually moored array was estimated to produce 1.4 GWh, whereas the interconnected arrays were estimated to produce ~2.5 GWh annually (an increase of nearly 80%) based on a total available resource of 15 GWh. Owing to the more complicated motions of the devices, heave was no longer a good predictor of the CWR and the relationship between the moorings, motions and CWRs is one that should be examined further.

For the flexible arrays, the loads in the lines and the motions of the devices were larger and more complicated than their rigid equivalents. Since the mooring lines were specific to each array, with the flexible interconnected arrays typically having heavier chain and clump weights, the cyclic component of the line load was compared. Whilst the performance of the flexible interconnected arrays was very similar, the cyclic loading of the bed lines in irregular waves and extreme waves was different. The loads on the interconnecting lines were high and snatching was observed in the extreme sea states.

Neither the devices nor the mooring configurations used in the physical modelling were proposed as the optimised solution for flexible interconnecting arrays and yet the increases in the CWR ratios, above the levels of the array effects found, show that there is scope for marked improvements to be made to the current technology. The CWRs calculated for the two types of array were within the range of those reported for typical floating OWC.

The flexible interconnected arrays showed the largest performance increase but this was at the expense of large motions and line loads. This may be mitigated with different mooring line designs but the prevailing wave direction must be taken into account. Expansion of the arrays to more devices would be difficult for the flexible arrays owing to the interaction between the mooring lines, the motions and loads and the CWRs. It is recommended that numerical modelling be used in the first instance to address this problem.

The rigid arrays had simpler moorings and the motions and loads were lower than those of the flexible arrays, though so too were the CWRs. Further investigation is necessary to discover the effects of the motions on the CWRs and to determine a practical limit of device expansion taking into account wave shadowing, platform motion and structural loads. Experimentation is suggested for the performance characterisation but numerical models may be used for the wave shadowing and structural calculations.

LIST OF ACRONYMS

D	Deliverable
CAD	Computer-aided design
CAPEX	Capital expenditure
COB	Centre of buoyancy
COM	Centre of mass
CWR	Capture width ratio
FPSO	Floating production storage and offloading (vessel)
LCOE	Levelised cost of energy
MWL	Mean water line
NE	North east
NW	North west
O&M	Operations and maintenance
OPEX	Operational expenditures
OWC	Oscillating water column
PTO	Power take-off
RAO	Response amplitude operator
RMS	Root mean square
SE	South east
SW	South west
SWL	Still water line
TM	Test model, used for designation of spar buoy models TM0 – TM5
TPL	Technology Performance Level
TRL	Technology Readiness Level
UHMWPE	Ultra-high molecular weight polyethylene
WEC	Wave energy converter
WP	Work package

1 INTRODUCTION

The WETFEET project was conceived to address the perceived barriers that impede the successful development of wave energy conversion. The project has studied four technological solutions to assess their potential to lead to a credible breakthrough in the areas: survivability, operations and maintenance (O&M), power take-off (PTO) and arrays. This report (Deliverable 6.5) details the results of Work Package (WP) 6, which concentrated on the array breakthrough: sharing moorings and electrical cables.

The technology involved in wave energy has not yet converged to a single design as with wind turbines and the cost savings associated with common components and efficiencies in the supply chain do not yet exist. Furthermore, devices remain small in terms of capacity compared to wind turbines. Since there are likely to be financial and environmental benefits as a result of increasing the energy generation per unit are of sea bed [1], arrays of WECs are seen as a potential solution to increased generation.

To date, wave energy is still a more expensive technology compared to other low-carbon and renewable sources. As reported in D6.1 [2], the moorings represent a significant fraction of the project costs for a wave energy deployment. This is not just a CAPEX consideration, more mooring lines and more complicated arrangements will lead to longer and more intricate installations. Together, moorings, installation and O&M have been estimated as accounting for 40% to 45% of the life time costs of a project [3, 4] and so any cost savings that can be achieved through inter-mooring of devices will lead to significant savings.

The principal goal of WP6 is to consider the effects of inter-mooring devices in an array to reduce costs through mooring component sharing. The goal of the first part of WP6 was to consider how arrays of devices may be interlinked. Deliverable D6.1 [2] focuses on the non-rigid inter-mooring of five spar buoy oscillating water column (OWC) devices. The report's conclusion was to propose one array geometry and three inter-mooring configurations for testing; these are described further in Section 2. Equivalently, D6.2 [5] analyses the potential configurations for rigidly-connected devices with a proposed coaxial OWC. The aim of the second part of WP6 was to undertake numerical and physical modelling of the devices in the various configurations to be able to assess how different inter-mooring strategies affected the performance, motions and loads of the arrays.

The work presented here focuses on the physical modelling undertaken as part of WP6, but draws on the previous Deliverables. The creation of the models is summarised from D6.3 [6] and the experimental set up is described in Section 2. To reflect the two inter-mooring strategies covered by WP6, *viz.* rigid and flexible, the Results section (Section 3) is split into two principal parts. A discussion of the results and how they can be interpreted in the context of the breakthrough criterion appears in Section 4 with conclusions drawn in Section 5.

Owing to the amount of detail that is tied in to the work presented here, much of the work undertaken is given in the Appendices including summaries of the methods used in the analysis of the data.

1.1 Physical modelling tests and indicators of success

The choice of the physical modelling scale was motivated in part by the need to undertake the experiments in the University of Plymouth Ocean Basin, Figure 1-1. The Ocean Basin is a deep-water wave and current facility in the COAST laboratory of the University of Plymouth. It has nominal dimensions of 15.5 m wide and 35 m long. The central floor section of the basin may be fixed at any position from the surface to 3 m deep.

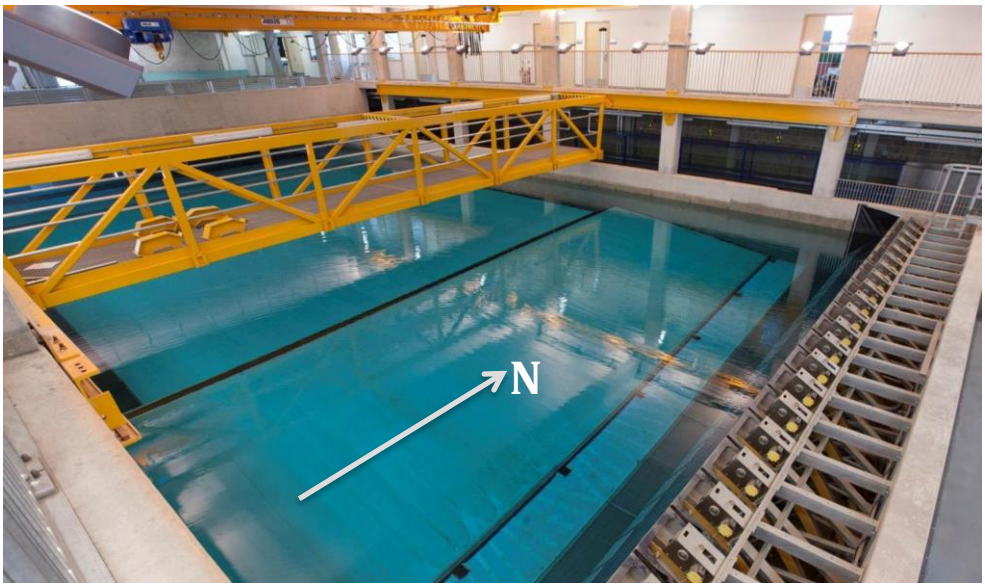

FIGURE 1-1 VIEW OF THE UNIVERSITY OF PLYMOUTH OCEAN BASIN

The Ocean Basin is equipped with 24 flap-type paddles with a hinge depth of 2 m (Edinburgh Designs Ltd.). The wave files are created with the Njord Wave Synthesis program and are managed by the basin control software (both Edinburgh Designs Ltd.) to create waves in the basin.

A combination of numerical and physical modelling was chosen to study the performance of the devices and arrays and to study the loading on the mooring lines. Experiments were run during four experimental sessions: October 2015, December 2015/January 2016, July 2017.

Regular waves were used to examine the capture width of the devices and arrays, while the irregular waves were used to examine performance, motions and loads under more realistic conditions. Larger sea states were used primarily to provide data as to how the devices moved and the tension experienced in the mooring lines under extreme conditions.

The irregular sea states were based on the wave climate encountered at Leixões, as reported in D6.1 [2] for which the resource diagram is shown in (Figure 1-2). Waves were generated with the Njord Wave Synthesis program based on a Pierson Moskovitz spectrum. The survivability waves represented the 10-, 25-, 50- and 100-year return periods based on the same spectral shape.

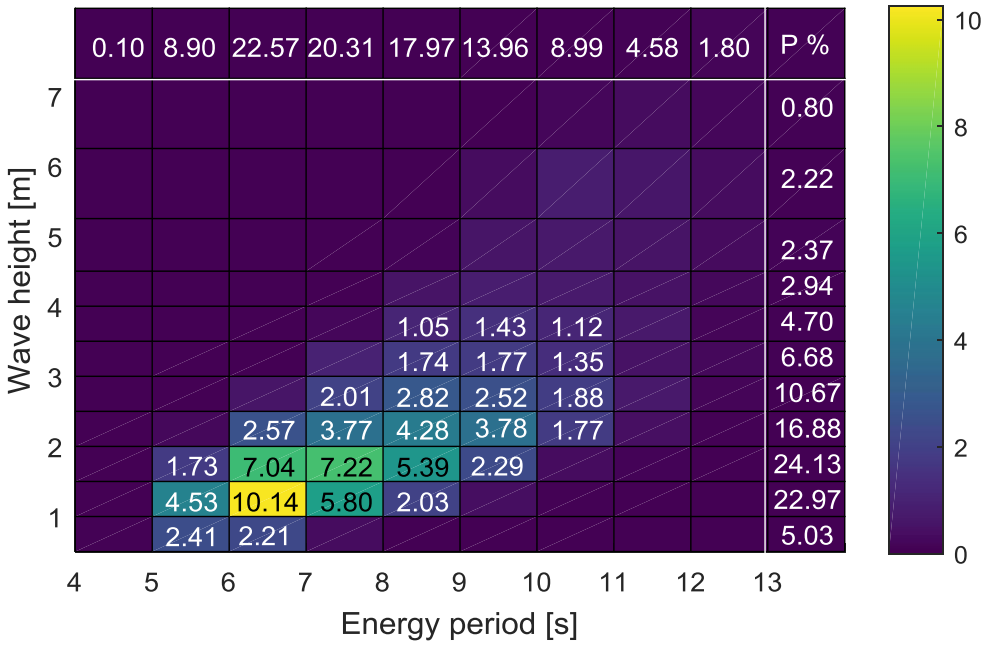

FIGURE 1-2 SCATTER PLOT FOR SEA STATE PROBABILITY AT THE SITE OF LEIXÕES, PORTUGAL

2 Physical models and configurations

In WP6, two WEC devices were used to investigate the performance and survivability of the device arrays: the spar buoy OWC and a rigid coaxial OWC. The spar buoy OWC was identified at the beginning of the WETFFET project as a potential test device, whereas the rigid coaxial device was developed during the project by IST, which allowed less time to develop the model in comparison with the spar buoy.

The 1:40 scale-models were designed from full-scale drawings provided by IST[1], with no constraints given on the choice of materials. Test models were designed and manufactured primarily at the University of Plymouth. WETFEET D6.3 [6] details the design and manufacturing procedure of the physical models and this process is summarised in this Section.

2.1 Rigid coaxial modes

Full-scale designs of the coaxial OWC model were provided by IST [6]. The designed OWC consists of two concentric, partially overlapping cylinders, shown in Figure 2-1, with a ratio

[1] Instituto Superior Técnico, Lisbon

between the diameters such that the inner area of the smaller cylinder was the same as the area of the annulus between the cylinders. The cylinder walls are made from 15 mm thick steel and are hollow to achieve the correct density properties for the design. The two shaded areas in Figure 2-1 are filled to provide ballast.

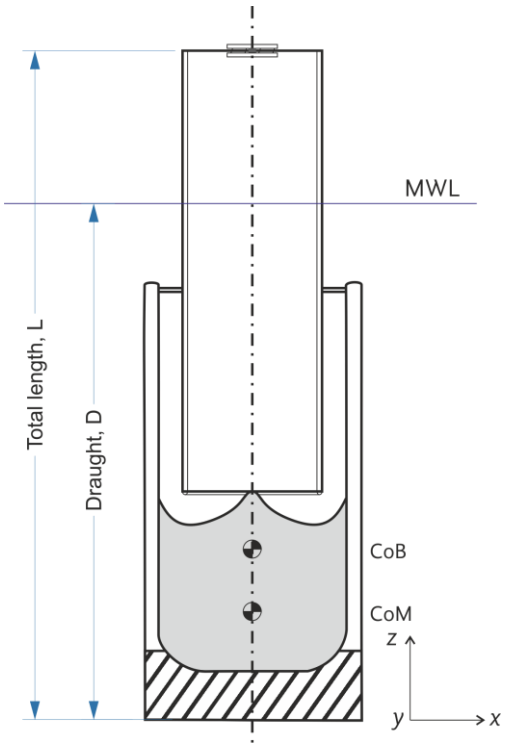

FIGURE 2-1 SECTION VIEW OF THE MAIN UNIT OF THE COAXIAL OWC

The device is not designed to oscillate in heave but as the waves approach, the change in water pressure causes the water to oscillate in both cylinders, in opposite directions. There is a curved profile that sits in the bottom cylinder, which is used to provide a path of constant section for the water moving between the cylinders. The bottom section of the lower cylinder, shown hatched in Figure 2-1, is anticipated to be the main ballast section.

From the design of the main unit, three configurations, shown in Figure 2-2, were proposed: an isolated device with heave plate (a), an array of devices (b) and an array of devices with a concrete base plate (c). For each configuration, the MWL falls at the same place on the model with respect to the top of the inner cylinder. To achieve this, the ballast would to be altered for each model.

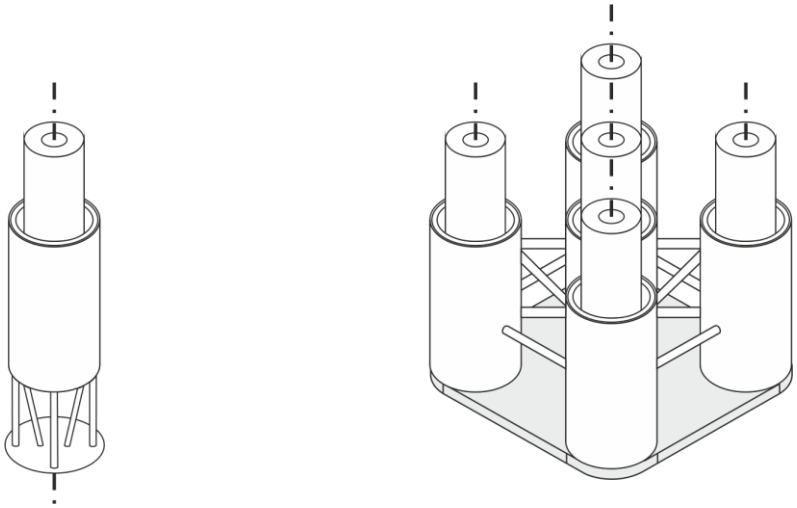

FIGURE 2-2 DIFFERENT CONFIGURATIONS TO BE CONSIDERED: INDIVIDUAL DEVICE WITH HEAVE PLATE (LEFT); FIVE-DEVICE ARRAY WITH PLATE (RIGHT).

A four-point catenary mooring was used to secure the devices to the basin floor. These were placed orthogonally to one another, approximately coincident with the COM in the *Z*-direction shown in Figure 2-1. For the isolated device, all four mooring lines are attached to the lower cylinder. For the arrays of devices, each corner unit accommodated one mooring line and details of the models and mooring lines made can be found in the Appendix.

The set-up of the rigid coaxial device array was simpler than for the spar buoy experiments and only two configurations were tested: an isolated device and a rigid array of five devices. Both models were moored such that the centre of the device was coincident with the centre of the basin. Anchor points radiated 6 m from the basin centre and a four-point catenary mooring was used to secure the devices as shown in Figure 2-3, with the inset figure giving the numbering of the individual base units comprising the array.

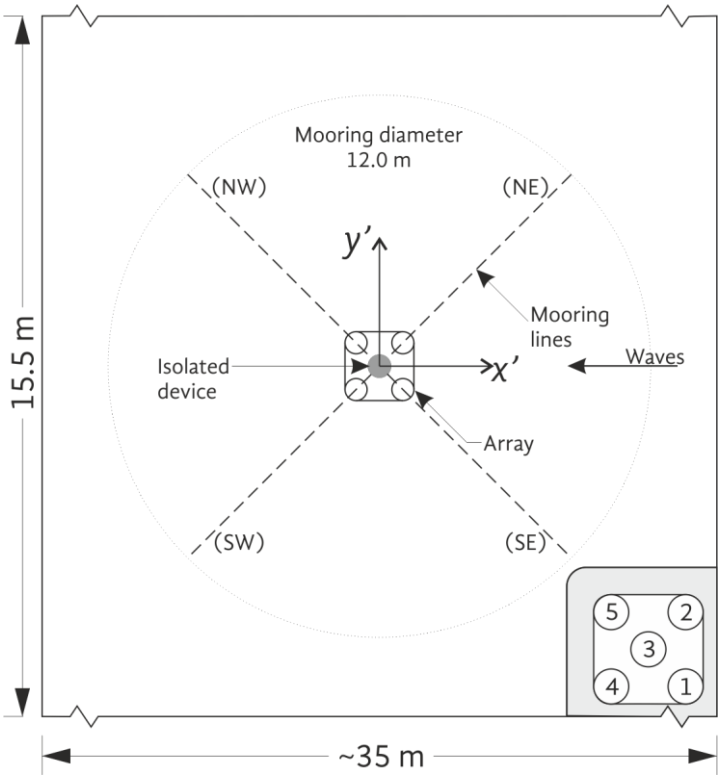

FIGURE 2-3 RIGID COAXIAL DEVICE SET-UP FOR THE ISOLATED DEVICE AND THE ARRAY OF DEVICES

Despite the anchor radius being the same in the isolated device and the array configuration, the mooring line lengths were slightly different owing to the differences in the fairlead radii and masses of the devices. In each case, chains were within 1% of the target length with details given in

Table 7-3 in the Appendix. A force sensor was mounted between the each of the chains and the device fairleads in both cases.

2.2 Spar buoy models

The OWC spar buoy was chosen as one of the test model designs as it has previously been investigated by members of the consortium and it was deemed a lower risk technology compared with others, as described in WETFEET D2.1 [7]. The full description of the design and manufacture of the scale models is given in D6.3 [6] and is summarised here.

Geometry for the full-scale design was based on that defined in WP2 (D2.1 citing [8]); and the 12 m diameter, 36 m draught version of the spar buoy was chosen. The full-scale drawing given in [9] was used as the basis for the scaling of the model spar buoy and Figure 2-4 shows the OWC spar buoy design with some of the features labelled.

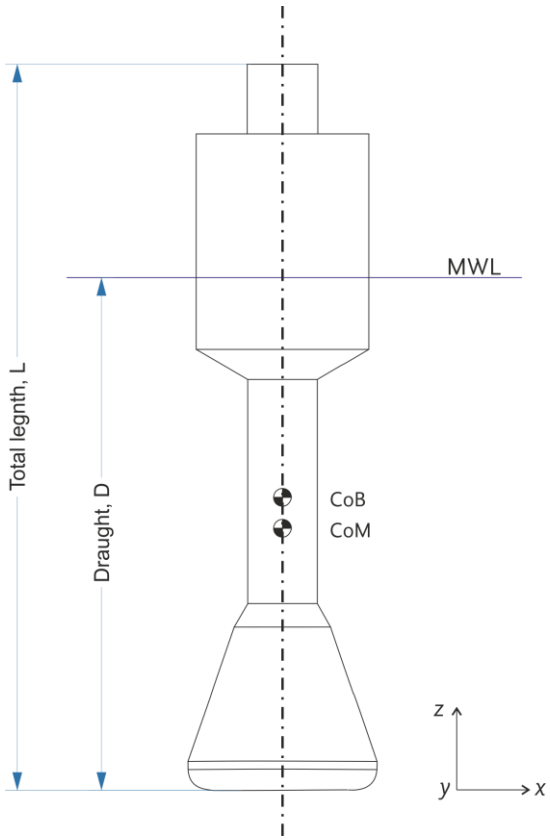

FIGURE 2-4 OVERVIEW OF THE FULL-SCALE OWC SPAR BUOY DESIGN

To ensure dynamic similarity with the full-scale design, Froude scaling was used to determine the 1:40 scaled geometry, ensuring that the gravity forces were scaled correctly. The new geometry was used as the framework for the geometry for the model as built. For the length measurements, the values were divided by the scale factor, λ, to the power of one. For mass, the full-scale values were divided by λ^3 and the mass moments of inertia were divided by λ^5. Figure 2-5 shows an image from CAD model and a photograph of one of the finished models. The devices were approximately 1.25 m high and had a mass of 19 kg. Details of the model properties are given in D6.3 [6] and summarised in the Appendix.

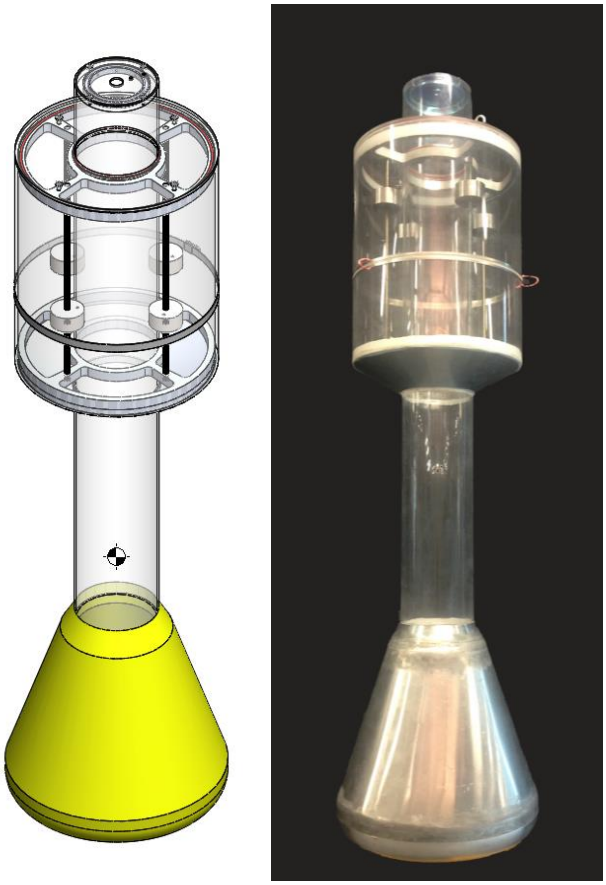

FIGURE 2-5 ISOMETRIC VIEW OF THE OWC SPAR BUOY DESIGN (LEFT) AND PHOTOGRAPH OF THE TM0 MODEL (RIGHT)

Five spar buoy models were built for the arrays, named TM1 – TM5, with TM3 being also used in the experiments with a single, isolated device. The models were built at the University of Plymouth with only the bottom cone made externally. In all experiments, the same model was used in the same array position.

The selection process of the configurations for the flexibly-moored device experiments was the subject of D6.1 [2]. An arrangement of five spar buoy devices was chosen to be arranged in a die format (⁘) with an inter-device spacing of 13 times the radius. The two benchmark cases were used: an isolated device with a three-point mooring to test array effects, and an array of five devices in the same array positions but each with a three-point mooring to test the effects of interconnection. The three inter-moored schemes (Configurations B, C and D) are shown in Figure 2-6 along with the individually-moored array: Configuration A.

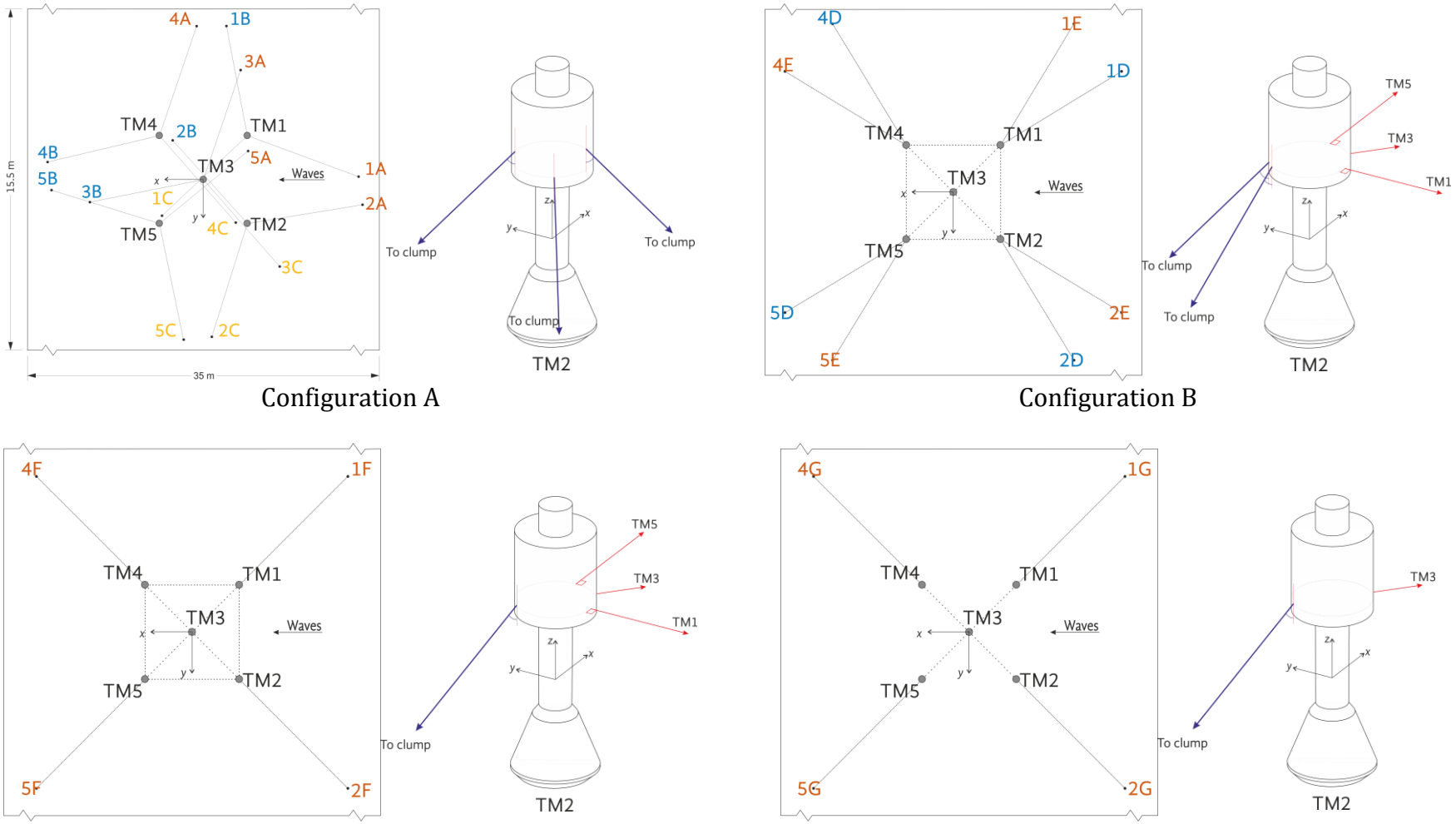

FIGURE 2-6 ARRAY CONFIGURATIONS OF THE SPAR BUOY OWCS

As stated in D6.1 [2], the configurations were not chosen to represent the optimum design, rather to provide realistic scenarios that would allow the sharing of infrastructure to be investigated.

The moorings for the spar buoy devices comprised two types: bottom-lines, connecting each device to the basin floor; and interconnecting lines; connecting two devices together. Bottom lines were a hybrid mooring: chain, and synthetic line with floats and clump weights as shown in Figure 2-7. Synthetic lines were tied to chain and to fairleads or force sensors where appropriate. Interconnecting lines were made from synthetic line and a clump weight was attached to the middle of each line. Details of the lines, floats and clump weights are given for each configuration in Appendix 8 on page 58.

FIGURE 2-7 VIEW OF THE THREE-POINT HYBRID MOORING OF THE SPAR BUOY

3 SELECTED RESULTS

The results presented in this Section cover the major findings of the power capture, device motions and line loads, with supporting material in the Appendix. Base line conditions for the flexible and the rigid arrays were different. The spar buoy arrays were compared to two different baseline conditions. First, a single device was used to determine the characteristic loads, motions and performance with no array effects present. A second baseline was the individually-moored array of five spar buoys, used to examine the effects of flexibly inter-mooring the devices. The rigidly-fixed array of five base units was compare to a single base unit.

3.1 Rigid arrays

The rigid arrays consisted of five coaxial OWC devices connected to each other and mounted on a rigid platform. To evaluate the performance of the array, the comparison device was a single coaxial OWC unit that had a heave plate and these are shown in Figure 2-2 on page 5. The surface elevation velocity was used to calculate the power absorbed through the orifice as described in Section 9.3.

3.1.1 Device and array natural periods

Table 3-1 reports the mean values of T_n based on five tests along with the full-scale theoretical natural periods for the array.

TABLE 3-1 NATURAL PERIODS FOR SELECTED DEGREES OF FREEDOM FOR THE MOORED RIGID DEVICES

	Theoretical	Isolated device		Array	
DoF	Full scale [s] (Array only)	Mean T_n (s.d.) [s]	Full-scale equivalent [s]	Mean T_n (s.d.) [s]	Full-scale equivalent [s]
Surge	151.5	27.51 (0.110)	174.0	29.18 (0.160)	184.5
Heave	69	7.08 (0.015)	44.8	9.72 (0.026)	61.5
Roll	27.6	n.d.	n.d.	3.60 (0.007)	22.8
Pitch	27.6	2.96 (0.006)	18.7	3.62 (0.008)	22.9

N.D. – NO DATA

The decay tests showed very low values of standard deviation, indicating good repeatability, despite the inherent difficulties in perturbing the device only along one axis. The roll and the pitch natural periods of the array were very close to one other, with the pitch natural period being 0.02 s longer (0.1 s at full scale). This indicates that the axisymmetry of the array construction was good. The period of the pitch may have been longer owing to the trim weights fixed to the front edge of the ballast plate to ensure the array floated level in the water. Compared with the theoretical values, those recorded for the array showed some discrepancy: the surge period of the model was longer than predicted whilst the other motions measured, i.e. the heave, roll and pitch, had shorter natural periods.

The natural frequency of the water column was not measured but given a theoretical full-scale natural period of the water columns of 14.6 s (as designed), the 1:40-scale equivalent would have been 0.433 Hz.

3.1.2 Capture width ratio – regular waves

Regular waves were used to examine the performance of both the isolated device and the array of five devices by way of CWR curves, which show the ratio of the converted power to the incident wave power, normalised by the width of the device. For the isolated device, the capture width was normalised by the width of the lower tube (0.340 m). For the array, the CWR was calculated for each sub-unit and summed to give the whole-array value. Input wave power came from empty basin data with a gauge placed at the location of the centre of each device.

3.1.3 Vertical position in water affects CWR

Figure 3-1 shows the CWR plot for the isolated device for a range of frequencies at the smaller of the tested amplitudes (H = 0.05 m). The data plotted were from experiments conducted on different days for which the distance between the still water line, SWL, and the CoM of the device had changed owing to water ingress as discussed above. For frequencies ranging from 0.525 Hz to 0.725 Hz, three experiments were conducted per frequency. Experiments were conducted on non-consecutive days with the model left *in situ* in between. Figure 3-1 is plotted to account for the change to the SWL-CoM distance (shown by the colour of the marker) and it is clear that there is a difference between the results collected on day 1 and day 4, showing that the CWR is affected not only by the frequency of the incident waves but also the draught of the device.

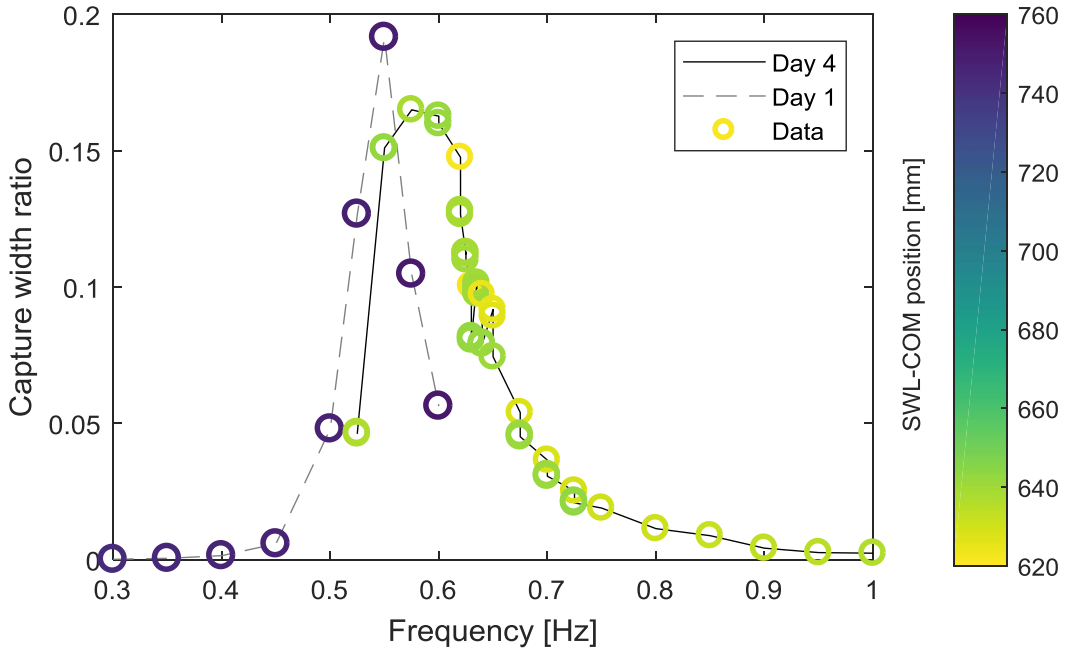

FIGURE 3-1 CAPTURE WIDTH RATIOS FOR THE ISOLATED RIGID DEVICE ENCOUNTERING MONOCHROMATIC WAVES. SERIES ARE SEPARATED BY EXPERIMENTAL DAY WITH MARKER COLOUR DENOTING SWL-COM DISTANCE.

Generally, there is a peak in the CWR between f = 0.5 Hz and f = 0.6 Hz, and a drop in the CWR at f = 0.630 Hz and f = 0.640 Hz for two of the three experiments. Figure 3-1 gives an indication of the performance in terms of the position of the device in the water: when the device was lower in the water, with a SWL-CoM distance of around 730 mm (on day 1), the CWR peaked at f = 0.550 Hz and the curve is narrow. The device draught is indicated by coloured markers that correspond to device draught given in the coloured scale. With a SWL-CoM distance of around 630 mm (on day 4), the peak of the capture width ratio was at f = 0.575 Hz. The values of capture width ratio at f = 0.525 Hz are very different between the two series. For the data with a SWL-CoM distance of around 630 mm, there are two data at

that frequency with the same value and so it may be assumed that these represent the correct CWR curve.

For the larger amplitude regular waves, with H = 0.1 m, there was less variation in the SWL-CoM distance, as detailed in Table 10-5, and this resulted in a more consistent CWR curve: Figure 3-2 shows the capture width data plotted against input frequency with the markers colour-coded based on the SWL-CoM value. A larger value indicates a model that was lower in the water. The grey curve joins data from one particular day (4th July, cf. Figure 10-3 in the Appendix) and is plotted to aid interpretation.

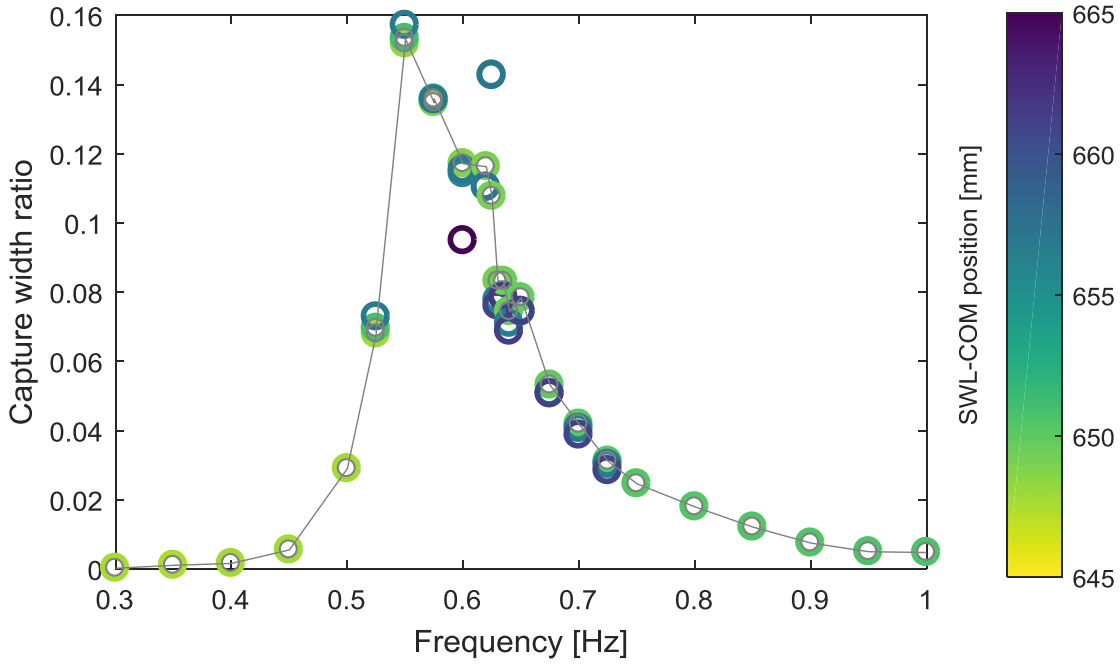

FIGURE 3-2 CWR FOR ISOLATED DEVICE; LARGER INCIDENT AMPLITUDE

As with the smaller amplitude waves, three experiments were conducted for frequencies in the range of f = 0.525 Hz – 0.725 Hz. The repeatability of the experiments is good but exceptions are apparent where there is a difference in the SWL-CoM value, such as between f = 0.600 Hz and f = 0.650 Hz. At f = 0.600 Hz, the drop in CWR is associated with a larger SWL-CoM value and this is the result of an experiment run after the first survivability wave test; the increased motion and wave loading may have permitted more water into the device, causing an increase in the SWL-CoM value and a drop in CWR. At f = 0.625 Hz, the higher marker represents data from two experiments with the same value. Here, a larger SWL-CoM value resulted in a larger CWR. Subsequently, for frequencies up to f = 0.725 Hz, larger SWL-CoM values are associated with lower CWRs.

The implications of changing model parameters are discussed in more detail in Section 4 and henceforth results are presented only when the model parameters are considered stable.

3.1.4 Increased input wave height leads to reduced CWR

Figure 3-3 shows that there was a decrease in the CWR as the wave amplitude increased. All input heights were tested three times, with the exception of H = 0.025 m which had an outlier removed (negative value) and H = 0.05 m, for which only two experiments were completed. The majority of the multiple-height experiments were done in a random order and at the end of the experimental session (see Figure 10-3 in the Appendix (page 79) for details on the order of the experiments). The exceptions to this are the data from the small and large regular wave experiments, which is why there is a large difference in the SWL-CoM values at H = 0.05 m. At other points in the parameter space, the variability of the SWL-CoM value does not seem to be responsible for the variability in the data.

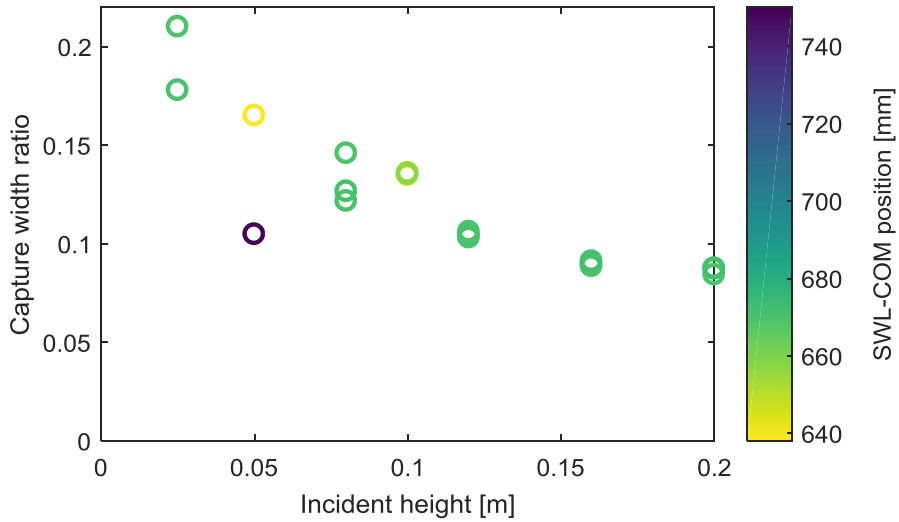

FIGURE 3-3 CAPTURE WIDTH RATIOS FOR THE ISOLATED DEVICE AT A SINGLE INPUT FREQUENCY AND MULTIPLE HEIGHTS. COLOUR INDICATES SWL-COM VALUE.

3.1.5 Devices in rigid array have different CWR

Since the variation in the SWL-CoM values was much less for the array than it was for the isolated device, the results for the array are presented without reference to the SWL-CoM distance. Selected plots are available in the Appendix to demonstrate this.

The CWR for each device in the array is shown in Figure 3-4 for the smaller waves (H = 0.05 m) and in Figure 3-5 for the larger waves (H = 0.10 m). In each figure, curves are drawn through the mean values for Devices 1 and 3 to aid interpretation. The numbering of the devices is given in Figure 2-3 on page 6.

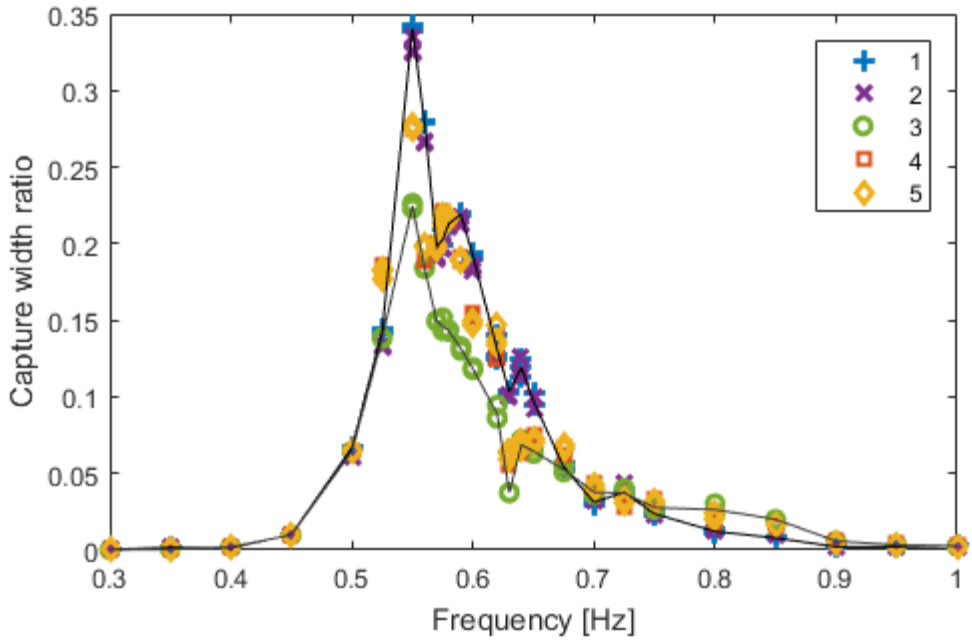

FIGURE 3-4 CAPTURE WIDTH RATIOS ARRAY UNITS WITH INPUT HEIGHT OF 0.05 M

Figure 3-4 and Figure 3-5 show peaks in CWR for all devices at f = 0.550 Hz, which coincides with the peak of the CWR for the isolated device (ignoring the experiments with very high SWL-CoM). Both figures indicate that this is a narrow peak and is concentrated around a small number of frequencies, somewhat in contrast to the isolated device, cf. Figure 3-1 and Figure 3-2. At f = 0.570 Hz, there is a drop in the capture width ratio for all devices, though for the smaller waves (Figure 3-4), this was not evident for the central device. There is a second drop in CWR at around f = 0.630 Hz for the smaller waves and this occurs for all devices. For the larger waves (Figure 3-5) the picture is less clear. As the experiments were conducted at f = (0.600, 0.625 and 0.650) Hz, a drop at f 0.630 Hz is not evident and there may have been some separation in the behaviour of the front (1 and 2) and back (4 and 5) devices in this range.

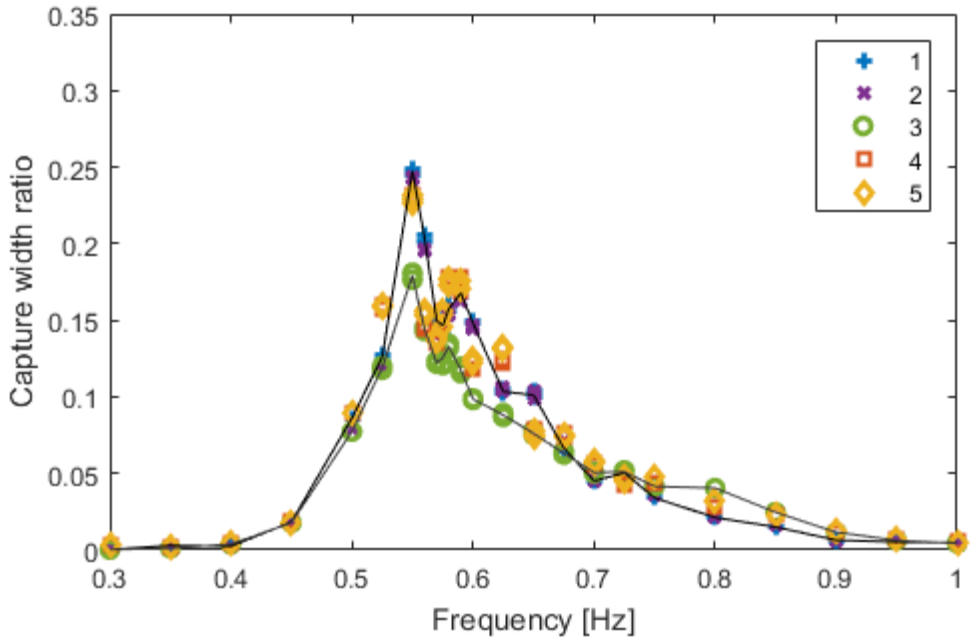

FIGURE 3-5 CAPTURE WIDTH RATIOS ARRAY UNITS WITH INPUT HEIGHT OF 0.10 M

As expected, there is little difference in the CWRs between the outside devices (1, 2, 4 and 5) and where separation is evident, the position of the device is what separates the values: devices 1 and 2, at the front of the array form one group and devices 4 and 5 at the back of the array form a second group. By contrast, the central device (Device 3) has a lower capture width ratio at almost all frequencies below $f = 0.700$ Hz, at which point it overtakes the outer devices to have the highest CWR. This is perhaps clearer in Figure 3-6 which shows the mean value curves for the isolated device and Devices 1 and 3 of the array for both sizes of regular waves.

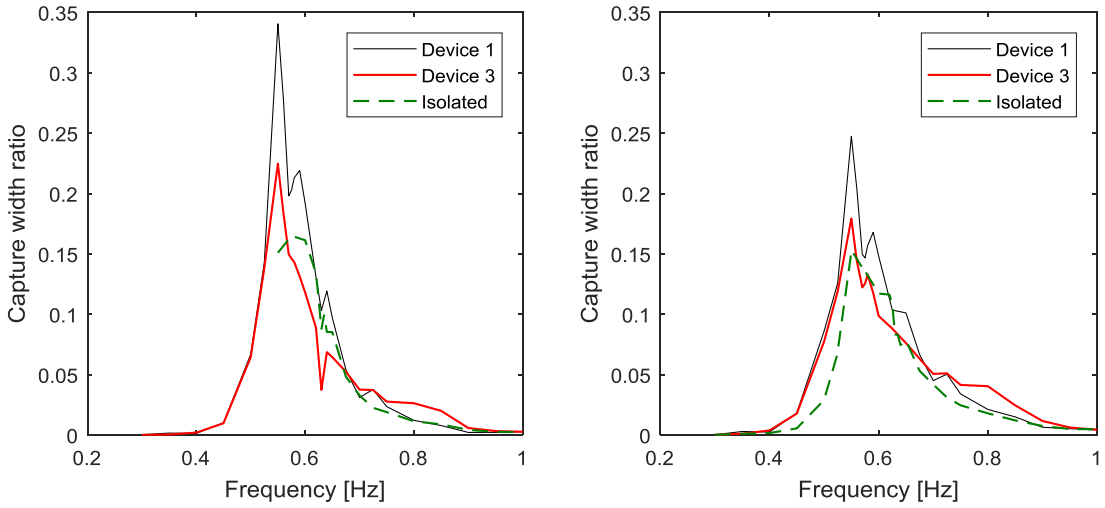

FIGURE 3-6 CWR OF THE DEVICES IN THE ARRAY COMPARED TO THAT OF THE ISOLATED DEVICE AT H = 0.05 M, (LEFT) AND H = 0.10 M (RIGHT)

Figure 3-6 echoes the results shown in Figure 3-3; larger input wave heights produced smaller CWRs and this was true for all devices. Figure 3-7 shows the effect of increasing the input wave height had on the CWR of all the devices in the array at f = 0.575 Hz. As with the previous results presented, the outer devices had a larger CWR than the central device, and this gap was greatest at small input heights. At the highest input height tested, H = 0.20 m, all the devices in the array had essentially the same CWR but this was larger than the corresponding CWR of the isolated device, *cf.* Figure 3-3.

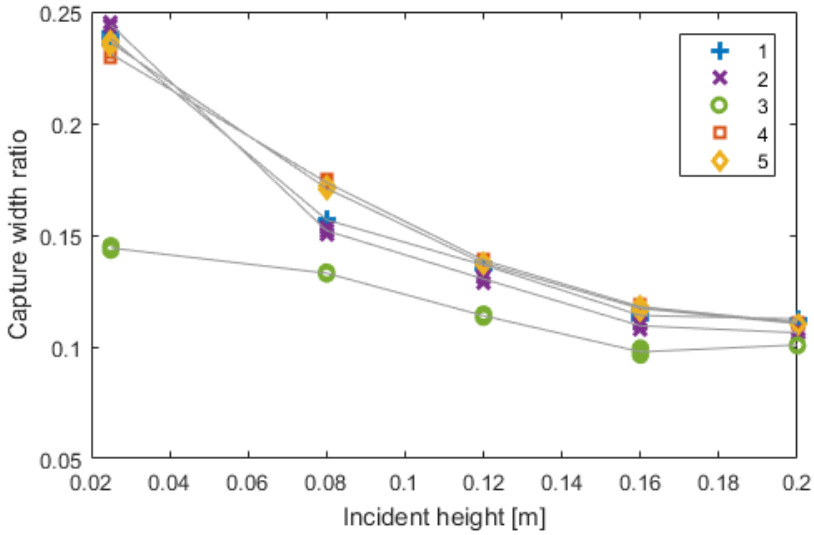

FIGURE 3-7 CAPTURE WIDTH RATIO FOR EACH SUB-UNIT OF THE ARRAY IN A RANGE OF INCIDENT WAVE HEIGHTS AT *F* = 0.575 HZ

3.1.6 Arrays have larger overall CWR

Irregular waves were used to examine the power capture of the device in realistic sea states. As explained in Section 3.1.5, the variation in the SWL-CoM value was considered low enough not to affect the results of each of the array experiments and so Figure 3-8 shows the capture width ratio for the sum of the whole rigid array compared to five times that of an isolated device.

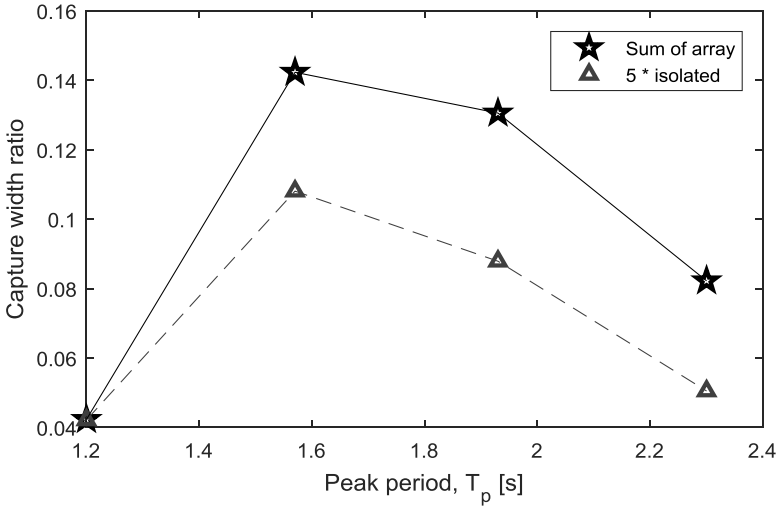

FIGURE 3-8 SUM OF THE CWR FOR ALL DEVICES IN THE ARRAY AND FIVE TIMES THE CWR OF THE ISOLATED DEVICE IN IRREGULAR WAVES

The CWRs values indicate that the array outperformed five isolated devices at all but the lowest value of T_p tested. It is likely that the CWR will continue to fall as the peak period increases for both the isolated case and the array. However, this range of irregular peak periods was chosen as 90% of the energy recorded at Leixões falls within the equivalent full-scale range, as shown in Figure 1-2, albeit at multiple significant wave heights. Table 3-2 shows the percentage increase of the CWR resulting from the array.

TABLE 3-2 DIFFERENCE IN CWR BETWEEN THE ISOLATED DEVICE AND THE ARRAY

Tp [s]	1.20	1.57	1.93	2.30
CWR 5*isolated	0.042	0.108	0.089	0.050
CWR array sum	0.042	0.142	0.131	0.082
% benefit	0%	31%	47%	64%

Figure 3-9 shows the capture width ratio for each of the devices in the array and the isolated device resulting from the irregular wave experiments with no reference to the SWL-CoM distance. The behaviour of the individual devices in the array was consistent with what has been previously presented: the outer devices have the same CWR and that was higher than that of the central device.

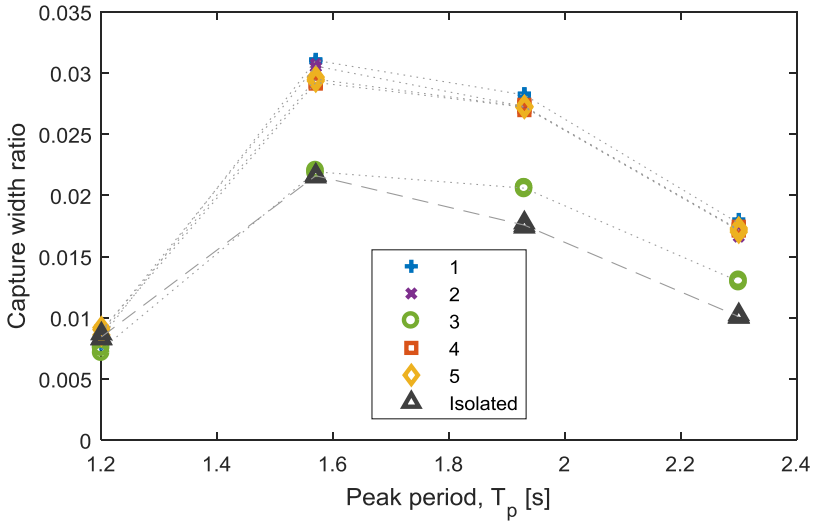

FIGURE 3-9 CAPTURE WIDTH RATIO FOR ALL DEVICES IN THE ARRAY AND THE ISOLATED DEVICE IN IRREGULAR WAVES

The CWR was at a maximum in the parameter space at the same point for all array units and the isolated device: T_p = 1.57 s. This is interesting because this peak period corresponds to 0.625 Hz and is one of the frequencies at which the regular wave experiments showed a drop in CWR, *q.v.v.* Figure 3-4 and Figure 3-5. After the peak at T_p = 1.57 s, the CWR decreased with increasing peak period for all devices.

The isolated device had the same CWR as the central array device (Device 3) for the two smaller peak periods tested, Figure 3-9 but a smaller capture width ratio at the higher T_p values.

Why the outer devices had a consistently higher CWR than the central device is not clear; with the available data it is not possible to discriminate between array effects and motion effects. Assuming that the motions of the devices had an effect on the CWR, Table 3-3 gives the possible scenarios.

TABLE 3-3 POSSIBLE CAUSES FOR DIFFERENCES IN CWR

	No array effects	**Array effects**
Same CWR	Motions the same	Array effects mitigated by difference in motions
Different CWR	Difference in motions AND Motions affect CWR	(Solely array effects AND No difference in motions) OR (Array effects AND Difference in motions)

Isolating the array effects from the effects of the motions is an important task that has implications on the performance of larger arrays of the same devices and this will be discussed further in Section 4.

3.1.7 Loads and motions in extreme seas

The behaviour of the isolated device and array were examined in a series of four extreme wave conditions, corresponding to the return periods of 10, 25, 50 and 100 years. During these extreme seas, waves were seen to overtop the device and so measuring the power extracted by the devices was no longer feasible. One such overtopping event is shown in Figure 3-10 from both above and below the water surface. In the subsurface photograph, on the right –hand side of Figure 3-10, the up-wave catenary lines are lifted much more from the sea bed than the down-wave lines.

FIGURE 3-10 OVERTOPPING WAVE SEEN DURING 10-YEAR RETURN PERIOD EXTREME SEA STATE

This behaviour of the catenary mooring lines was typical in the response of both the isolated device and the array of devices and this is seen in the loading time series shown in Figure 3-11. The surface elevation as recorded on the most up-wave gauge is shown for comparison and the event shown in Figure 3-10 is highlighted. The mooring line designation refers to the corner of the model and its position within the basin. The south east (SE) and north east (NE) mooring lines were up-wave of the device and the south west (SW) and north west (NW) mooring lines were down-wave of the device. Figure 3-11 shows that the mooring line loads were much higher up-wave of the device; the mooring line down-wave of the device did not deviate too far from their static load. The maximum load on the front lines was ~30 N, which is equal to 1920 kN at full scale, and ~10 N for the rear lines (640 kN at full scale). Grade 2 ("high strength" studlink anchoring chain can easily be found to fit this requirement even with a large safety factor.

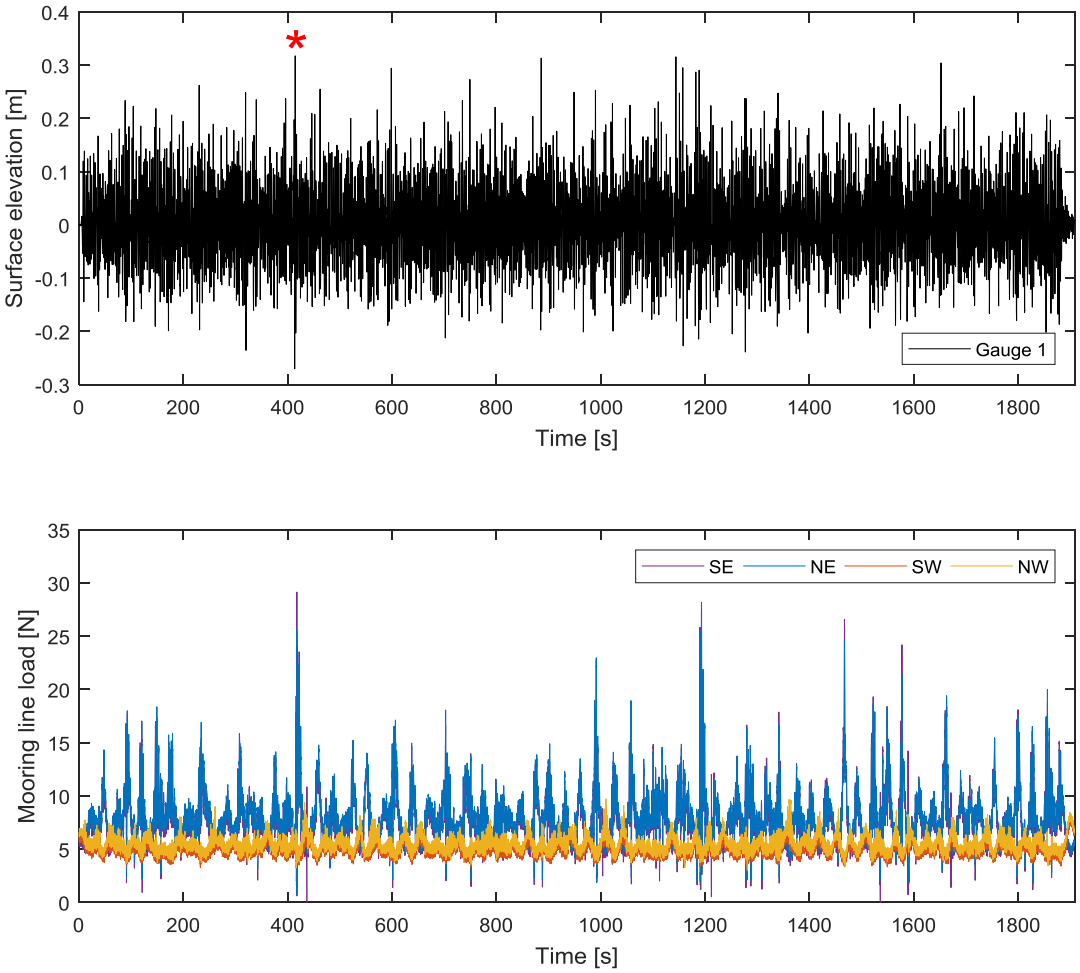

FIGURE 3-11 EXTREME WAVE SURFACE ELEVATION AND MOORING LINE LOAD

The amplitude spectrum of the waves and the loads recorded during the 10-year return period extreme sea state are shown in Figure 3-12, for which the frequency is plotted on a log scale. The peak wave frequency, in this case f_p = 0.38 Hz, seemed to have no effect on the loading of the mooring lines; nearly all the energy in the load signal appeared at frequencies lower than 0.1 Hz. For both the isolated device and the array of devices, there was a peak in the load amplitude spectrum of the up-wave lines at the surge natural frequencies (reported in Table 3-1). However, there was also a significant amount of energy in the mooring lines at much lower frequencies – corresponding to periods in the region of 40 s. The source of this remains unclear but it could be a coupled motion effect.

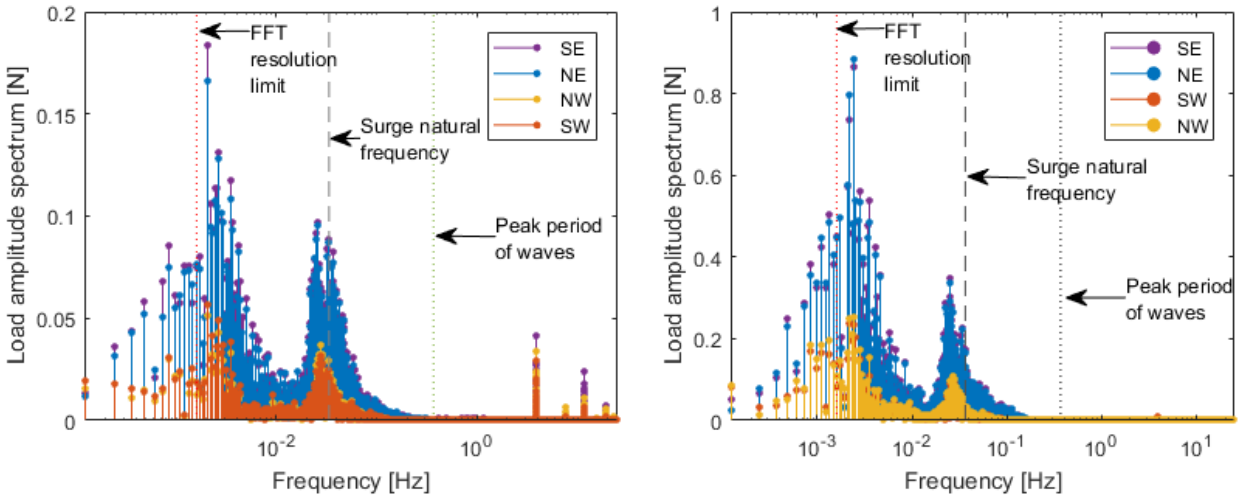

FIGURE 3-12 LOAD AMPLITUDE SPECTRA FOR THE ISOLATED DEVICE (LEFT) AND THE ARRAY OF DEVICES (RIGHT)

The amplitude spectra of three of the degrees of freedom: surge, heave and pitch, are shown in Figure 3-13. Data from regular wave experiments (not presented here) suggest that the magnitude of the surge response is not constant; nevertheless, the natural frequency of the surge motion dominated the response. There is a second peak in the surge motion response that occurred slightly below the peak frequency at f = 0.34 Hz (f_p = 0.38 Hz), with other surge motions between 0.20 Hz and 0.6 Hz. The majority of the heave motion response also occurred in this frequency range, with the lower frequency heave motion coincident with the heave natural frequency. The pitch motion amplitude spectrum has two peaks: one which occurred between the pitch natural frequency and the peak frequency of the wave spectrum; the other which occurred at approximately twice the pitch natural frequency.

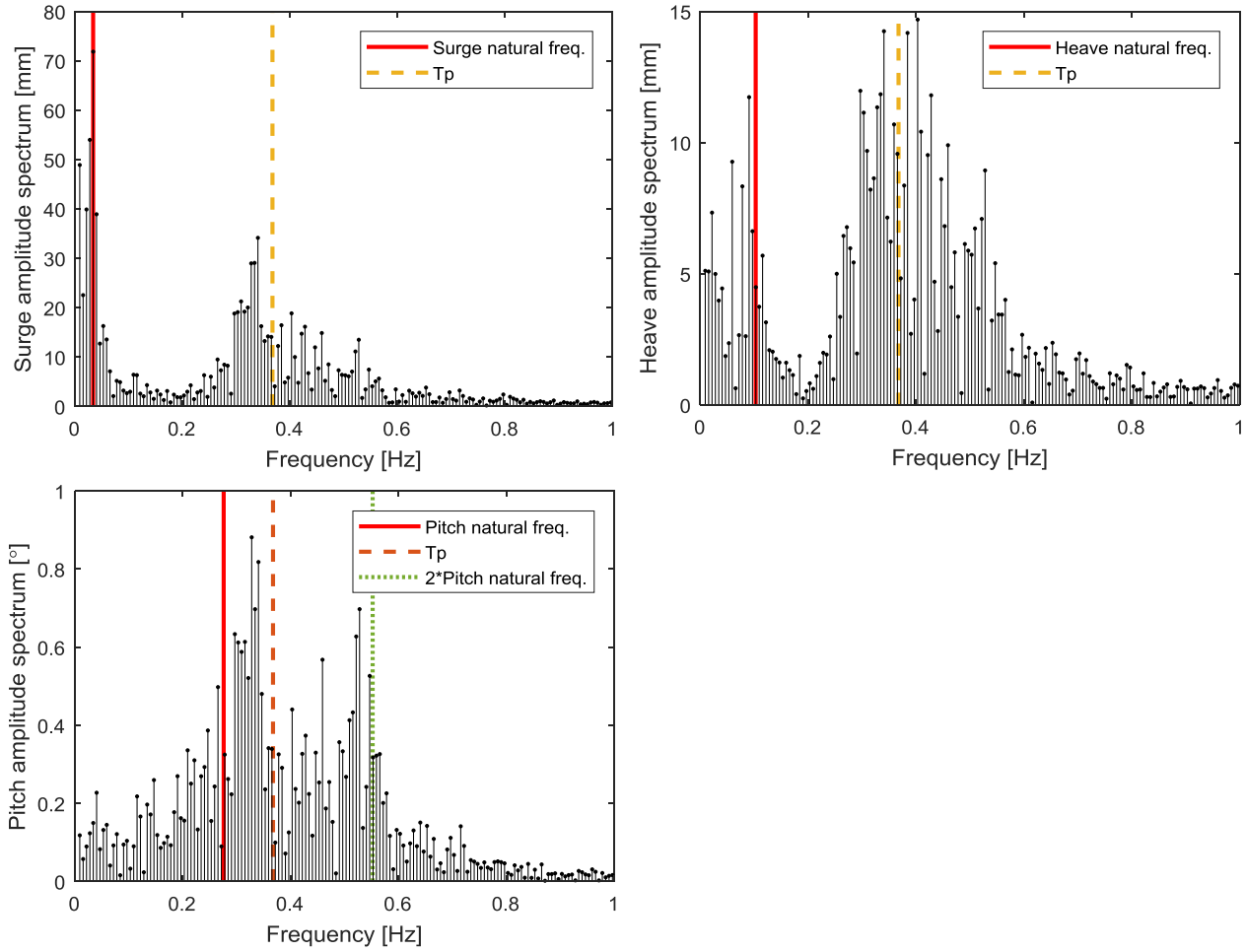

FIGURE 3-13 AMPLITUDE SPECTRA OF TWO MOTIONS AND A ROTATION OF THE RIGID DEVICE ARRAY

3.2 Flexible arrays of spar buoys

Owing to the larger number of configurations to be tested and the more numerous degrees of freedom that could describe each configuration, the spar buoy experiments were much more complicated than those of the rigid arrays. The same wave conditions were used for the flexible arrays as for the rigid array, except that regular waves were only run at one height. The extreme sea states caused more motions and overtopping of the flexible arrays and not all extreme sea states were completed.

3.2.1 Device and array natural periods

The values of natural period were calculated for all degrees of freedom except yaw for the isolated spar buoy and are reported in Table 3-4. The tolerance of the natural period was calculated as the 95% confidence interval to indicate the repeatability of testing in each

degree of freedom. The natural period of the internal water column was specified for the full-scale design as 11.33 s, equivalent to 1.79 s at 1:40 scale (0.56 Hz).

TABLE 3-4 NATURAL PERIODS FOR THE ISOLATED SPAR BUOY (TM3) DEVICE WITH A 95% CONFIDENCE INTERVAL

DoF	Surge	Sway	Heave	Roll	Pitch
Natural Period, *T* [s]	16.23	16.02	1.53	5.71	5.57
Tol [±s]	0.01	0.03	0.02	0.77	0.07

Due to the axisymmetric design of the device, the planar translations (surge and sway) and rotations (roll and pitch) were assumed to be the same: Table 3-4 shows that for the isolated spar buoy the natural periods of the roll and pitch and of the surge and sway were very similar. Small differences in the results were due to the orientation of the mooring restoring forces with respect to the axis of motion.

Table 3-5 shows the decay test results for surge and heave motions for the central array device (TM3) and a corner device (TM2) for all configurations, where Configuration A was the array of individually moored devices. The line arrangements of the Configurations are described in Appendix 8. The central device in the arrays was the same model as in the isolated case (TM3). Table 3-5 shows that small differences in heave and surge natural period were calculated between the isolated and array configurations.

TABLE 3-5 DECAY TEST RESULTS FOR ALL CONFIGURATIONS

	Surge natural period [s]		Heave natural period [s]	
	TM3	**TM2**	**TM3**	**TM2**
Config A	16.47	15.8	1.58	1.61
Config B	23.17	22.02	1.48	1.48
Config C	24.84	24.26	1.47	1.46
Config D	15.99	Unstable	1.47	1.48

For Configuration A, small differences between the corner device, TM2, and the central device, TM3, were calculated in the natural periods. There was a larger difference between the surge values than between the heave values since in the heave plane the restoring forces provided by the moorings were identical but along the surge axis the restoring forces acted at different angles owing to the mooring arrangement.

Compared to Configuration A, the interlinked Configurations (B, C and D) had lower heave periods for both the central and corner devices and the heave periods of the interlinked cases were all very similar, suggesting that if the interlinking lines are designed to provide similar static restoring forces, as they were in this case, the level of connectivity will not make a significant difference to the heave motion of the devices. As the spar buoy was designed to heave to achieve greater power conversion, this implies that interconnected arrays may have similar power conversion results; Sections 3.2.2 and 3.2.3 show this to be true.

3.2.2 Performance in regular waves

The capture width ratio, as described in Section 9.3.2, describes the length of wave crest, as a proportion of the device width, that contains the same incident power as that converted by the device. It can be used to evaluate the performance of a device, larger capture width ratios mean more wave energy is converted. Since it is a ratio, the capture width ratio remains the same between scale models and their full scale equivalents.

3.2.2.1 Array effects are generally small

Figure 3-14 shows the capture width ratio from the isolated device and the same device within Configuration A and five times the CWR of the isolated device with the sum of the CWR for all devices in Configuration A. Data from all experiments are plotted and a curve is drawn through the mean value at each frequency. The behaviour of the CWR in each of the cases is similar: as the frequency increased, the CWR increased, reached a peak between f = 0.60 Hz and f = 0.70 Hz and then decreased. The location of the peak frequency is somewhat complicated by the drop at f = 0.630 Hz. This frequency produced waves a quarter of the width of the basin and so produced cross waves in the basin. During experimentation, a cross wave was visible at this frequency and the effect on the incident wave field was noticeable in the wave data. Waves of this length are also approximately the same as the width of the array itself, explaining why the CWR of the array was much lower than that of the isolated device at this frequency. This result does not represent the expected behaviour at full-scale in open water, however the limitations of scaled physical experimentation makes this phenomenon very difficult to avoid. The numerical model described in WETFEET D6.4 [10] corroborated this; there were no decreases in the motions at this frequency in any of the simulations. In future, numerical modelling may be used to assess the effect of the basin walls on the results.

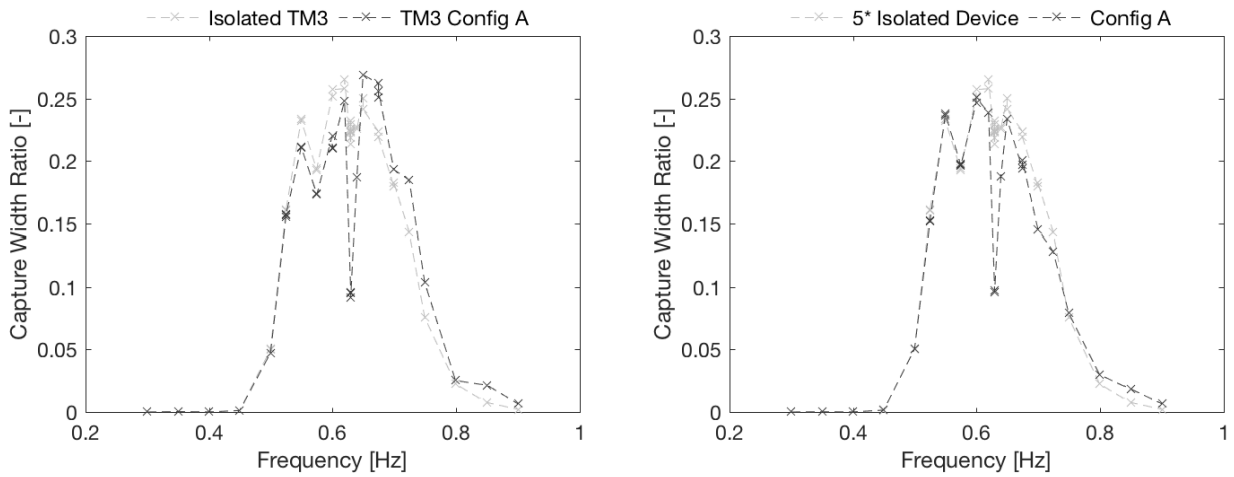

FIGURE 3-14 CAPTURE WIDTH RATIO FOR THE ISOLATED DEVICE, TM3, AND THE SAME DEVICE WITHIN CONFIGURATION A (LEFT) AND FOR ALL DEVICES OF CONFIGURATION A AND FIVE TIMES AN ISOLATED DEVICE (RIGHT)

The whole array CWR for Configuration A is also compared to five times the isolated device CWR in Figure 3-14. Similarly to the single device results, at low frequencies (f < 0.45 Hz)

Configuration A and the isolated device show negligible power outputs. There do not appear to be any array effects on the capture width ratio below f = 0.50 Hz. At f = 0.55 Hz, close to the internal water column natural frequency, a local peak is seen for both Configuration A and the isolated case. This suggests that the inner and outer devices in the array had similar resonance and response characteristics.

The influence of the cross waves was also seen in the RAOs; Figure 3-15 shows the heave RAO for both the isolated and the central device of Configuration A. As with the CWR, the heave RAO was much lower at f = 0.630 Hz for the array than for the isolated device, having dropped by ~25% of adjacent frequency values compared to ~10%. This indicates that heave is a good predictor of performance in regular waves.

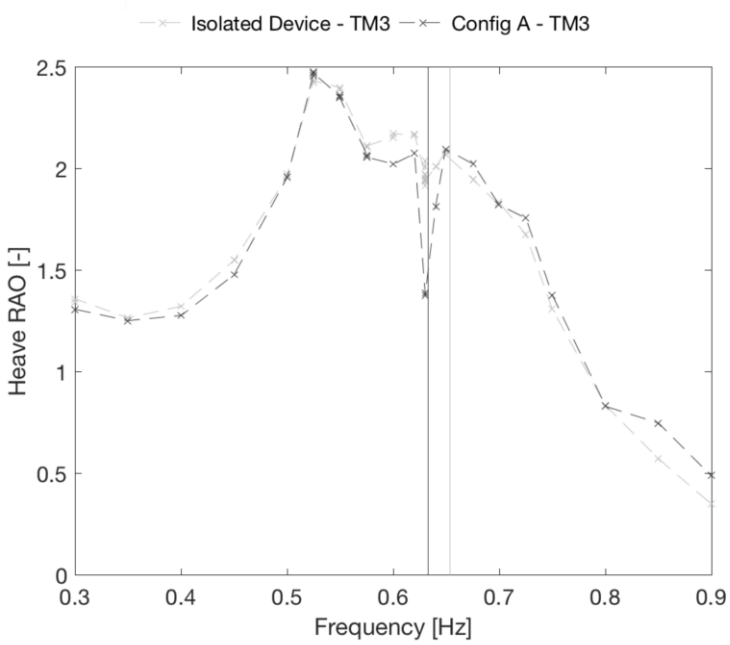

FIGURE 3-15 HEAVE RESPONSE AMPLITUDE OPERATOR FOR THE ISOLATED DEVICE AND THE SAME DEVICE IN CONFIGURATION A

For the other degrees of freedom, the presence of the other devices within the array configurations caused few differences in the motion responses of the central device compared to the isolated case; the RAOs for all six degrees of freedom are given in Figure 10-5 in the Appendix. Within the limits of repeatability and the limits of the motion tracking system, the surge and sway motions were the same for both the isolated and the central device in the array.

3.2.2.2 Interconnection improves capture width ratio

Figure 3-16 shows the CWR as a function of wave frequency for the central device (TM3) of all configurations and for all devices in the array. The magnitude of the CWR for the interconnected Configurations is more than twice that of the individually moored array (Configuration A) at the peak. It is clear when comparing the heave natural frequencies from the decay test results in Section 3.2.1 that interconnection of the devices led to a higher

natural frequency compared to the individually-moored Configuration (0.63 Hz compared to 0.68 Hz). The peaks in the CWR values for the interconnected arrays were coincident at this higher natural frequency.

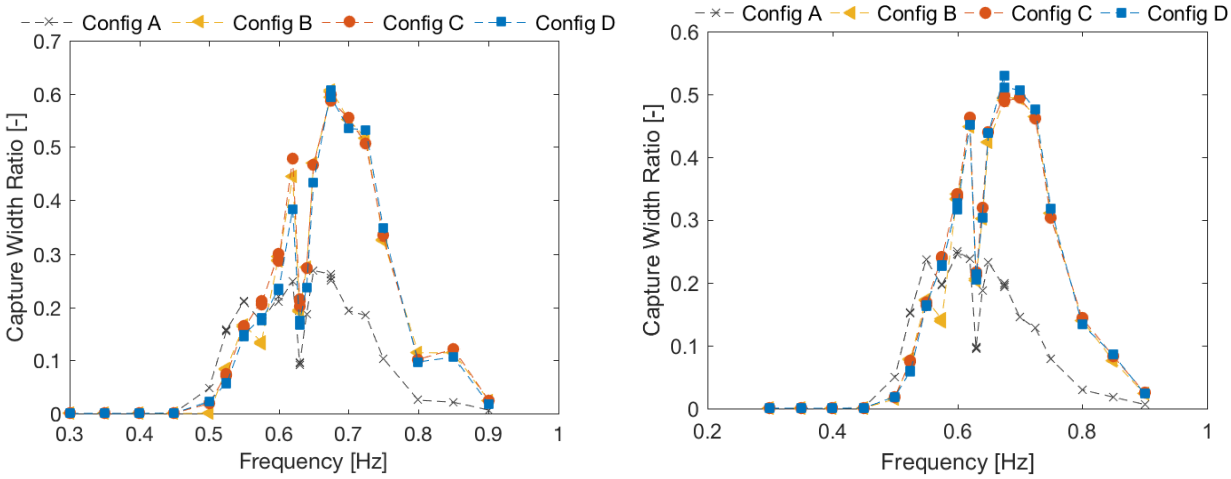

FIGURE 3-16 CAPTURE WIDTH RATIO OF THE CENTRAL DEVICE, TM3, (LEFT) AND FOR THE WHOLE ARRAY (RIGHT) IN ALL ARRAY CONFIGURATIONS

The heave motion responses under the same conditions are plotted in Figure 3-17 for the inner (TM3) device and one outer device (TM2). At lower incident wave frequencies, the interconnected cases heaved less than the individually moored device did. The differences in the heave RAOs were not as large as those in the CWRs (Figure 3-16), but they show that the peak motions of the interconnected arrays occurred at higher frequencies than for the individually moored array. This resonance shift for the interconnected cases was supported by the numerical model described in D6.4 [10]. Figure 3-17 shows that the effects of cross waves in the basin were also apparent in the array heave RAOs.

The interconnected cases also appear to have a much broader-banded CWR compared to Configuration A, which is beneficial to the energy extraction potential of a device deployed in the sea. For the target deployment site of Leixões, the higher frequency resonance of the interconnected arrays would lead to higher annual energy extraction due to the high probability of low-period wave conditions, as shown in the scatter matrix in Section 1. This is discussed further in Section 4.

Whilst the heave magnitude is a good predictor of CWR, it is clear from Figure 3-16 and Figure 3-17 that it is not the only factor governing the response; the heave of TM3 at f = 0.70 Hz was 44% higher in the interconnected configurations compared to Configuration A but at that frequency the CWR was over 200% larger than that of Configuration A. This is likely linked to the relative motion of the internal water column and the device; if the motion of the device and the water column are in phase then there will be no flow through the orifice and a CWR will be zero. The largest flow will occur when the phase is π radians, so it is likely that this

increase in CWR at the higher frequencies is due to the motion phasing. This relationship is explored further in Appendix 10.4.

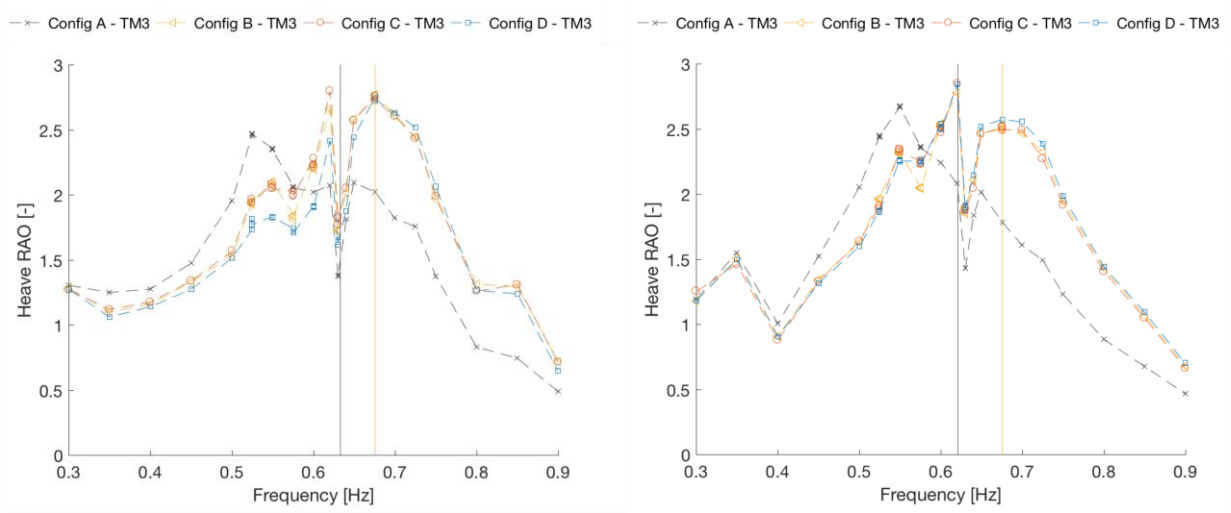

FIGURE 3-17 HEAVE RESPONSE AMPLITUDE OPERATORS FOR THE INNER DEVICE (LEFT) AND THE MEAN OF THE OUTER DEVICES (RIGHT)

3.2.2.3 Loads and motions

The cyclic tension for the most up-wave sea bed line at each frequency was compared for all Configurations. As with the heave motion responses shown in the previous Section, the amplitude of the cyclic tension of the isolated device and the individually-moored array, were the same apart from a reduction at $f = 0.63$ Hz and a greater reduction was seen for Configuration A than for the isolated device (this is shown in Figure 10-11,10.4).

For the arrays, the mooring layouts were specific to each Configuration, meaning the position of the anchor points and the fairleads of the most up-wave line changed between Configurations, with the exception of the bed lines in Configurations C and D. In addition, the chain diameters, clump weights and floats were specific to each Configuration to match the static surge stiffness of the isolated case, therefore Configuration A's large cyclic tension values are affected by the use of smaller diameter chain than for the interconnected Configurations. Information on the layout and composition of the lines is given in the Appendix (starting on page 58).

Figure 3-18 shows the dynamic load on the most up-wave line for each of the arrays in regular waves as a function of wave frequency. The line tension for Configuration A follows a similar form to those already seen in the CWR (Figure 3-16) and the heave motion (Figure 3-17) whereas the tension in the most up-wave line is very different for the interconnected arrays.

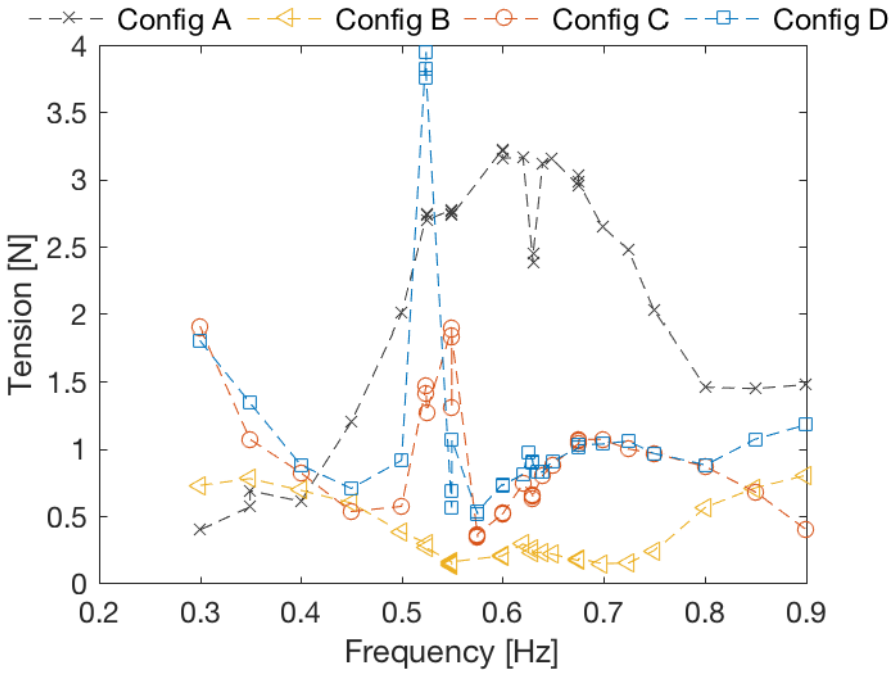

FIGURE 3-18 AMPLITUDE OF CYCLIC TENSION RESPONSE TO REGULAR WAVES FOR THE MOST UP-WAVE MOORING LINE

It can be seen from Figure 3-18 that by interconnecting the array, the cyclic tension was generally reduced for the front-most seabed line at frequencies above $f = 0.4$ Hz. This is a highly desirable characteristic for WEC development due to the reduced risk of fatigue failures and this is discussed further in Section 4. Spikes in the tension were apparent in the lines of Configurations C and D, with the latter exceeding that of the individually moored Configuration A. Configurations C and D both only had one bed line per corner device (see Figure 2-6, page 9) and so it was expected that they would undergo the largest line tensions in the bed lines as the loads were only taken by one line.

Figure 3-18 shows that the lowest cyclic tension for an interconnected array was associated with Configuration B; the motions of Configuration B, shown in Figure 3-19, were similar to those of the other interconnected arrays in every degree of freedom apart from pitch for which the RAOs were generally lower. This suggests that the pitching of the devices contributed significantly to the cyclic tension magnitude. It follows that reducing the pitch response of the devices could reduce the cyclic loading of the sea bed lines.

Figure 3-19 shows that peaks in the motions of the interconnected arrays often occurred at the same frequency regardless of the Configuration with the notable exceptions being the heave motion for all Configurations, which occurred at higher frequencies than the other motions, and the pitch for TM2 in Configuration C, which occurred at a higher frequency than the other peak motions for Configuration C. For the interconnected arrays, the spikes in the line tension typically corresponded to peaks in the motions of the outer device. However, for Configuration C, the largest line tension coincided with the largest pitch RAO further indicating that pitching was a key contributor to the line tension.

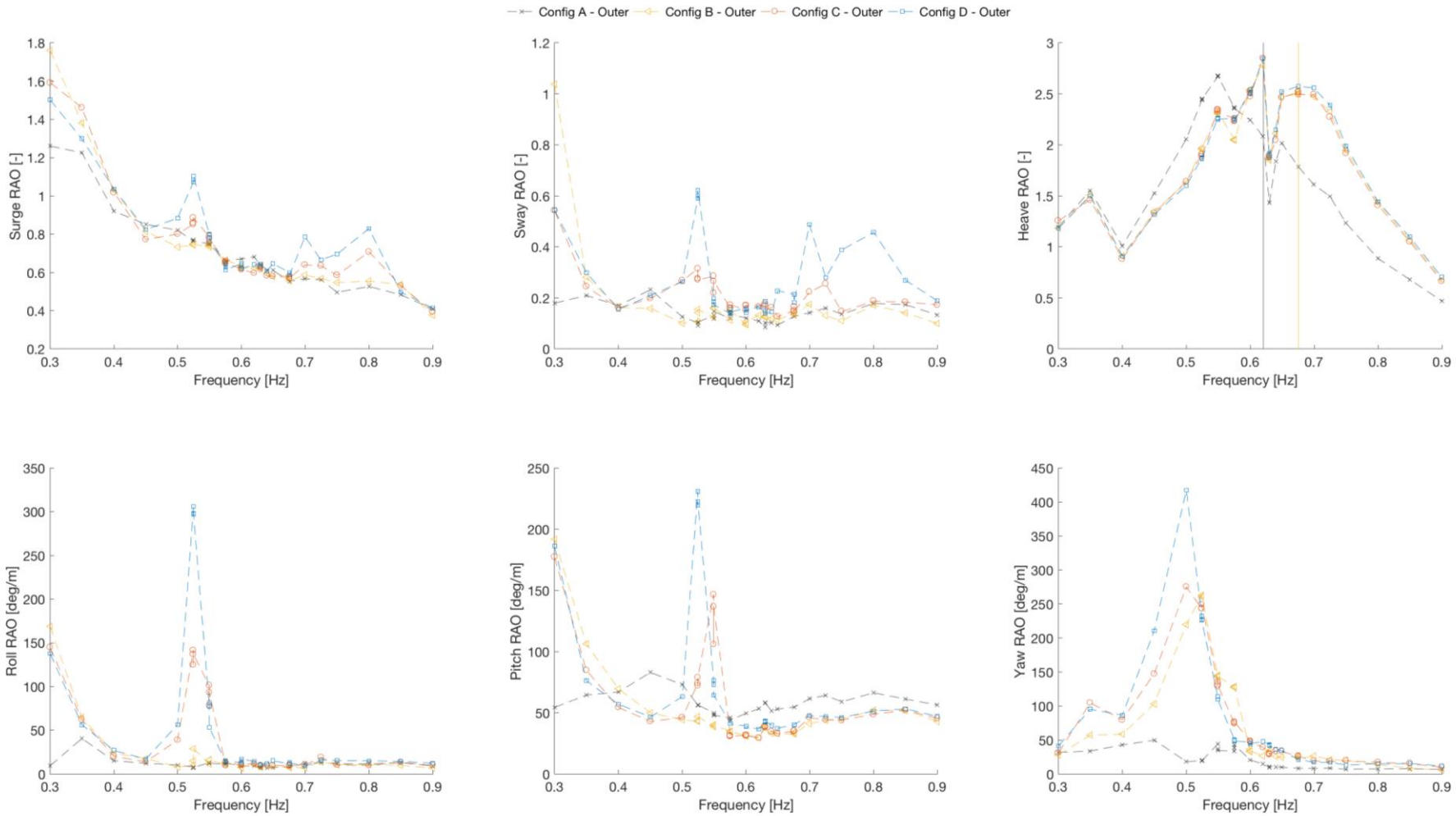

FIGURE 3-19 TIME-DOMAIN RESPONSES OF THE OUTER DEVICES FOR REGULAR WAVES OF CONSTANT HEIGHT (*H* = 0.05 M)

The spike in cyclic tensions in Configurations C and D at $f = 0.525$ Hz (Figure 3-18) corresponds to the similar spikes seen in the pitch and roll RAOs at the same frequencies (Figure 3-19). To investigate this further, a frequency domain analysis was undertaken and the amplitude spectrum of the line load is plotted at each incident wave frequency in Figure 3-20. Data are interpolated between frequencies to provide continuous colours in the plot.

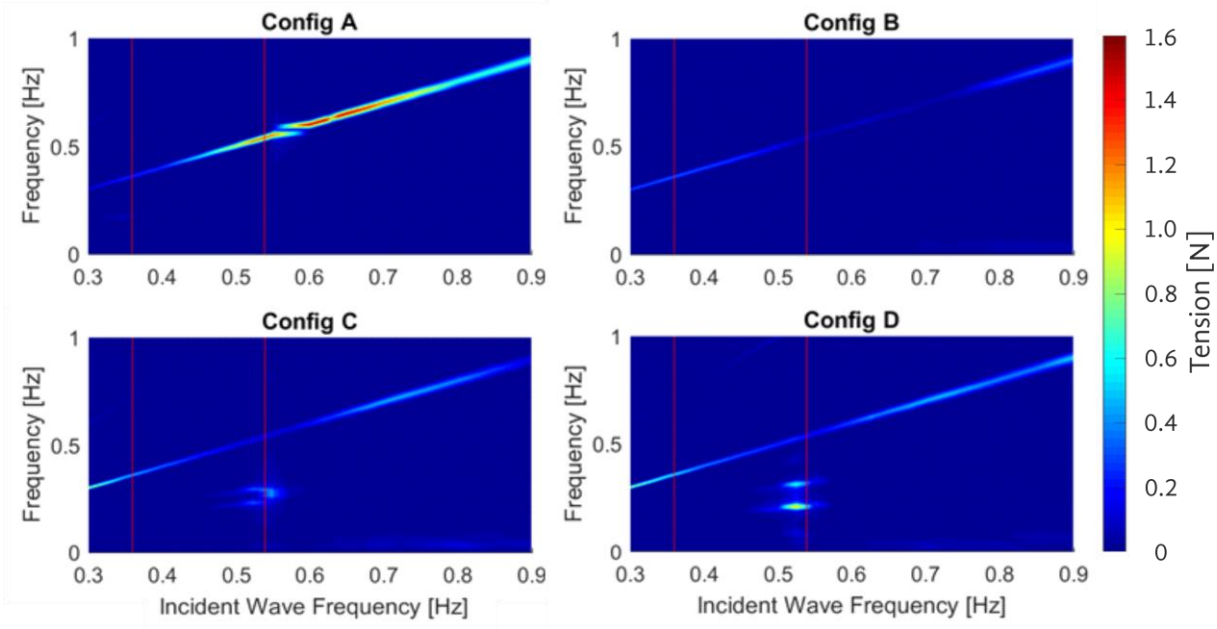

FIGURE 3-20 INTENSITY OF TENSION AMPLITUDE SPECTRA FOR EVERY WAVE FREQUENCY TESTED WITH 2ND AND 3RD HARMONICS OF THE PITCH NATURAL FREQUENCY OVERLAIN IN RED

Figure 3-20 shows that the frequency of the tension response could occur at frequencies other than that of the incident wave frequency. When the number of seabed lines was reduced from two to one (Configuration B to C), a response around $f = 0.2$ Hz was excited with incident waves of $f = 0.525$ Hz. This non-linear behaviour is also seen in the surge and pitch motions of the outer device in Configurations C and D, plotted in Figure 10-8 in the Appendix. The intensity of the motion and the line tension at $f = 0.2$ Hz was greatest for Configuration D, suggesting that the interconnecting lines perpendicular to the wave front in Configuration C were restricting the motions responsible for this low-frequency non-linear response.

From Figure 3-20 it can also be seen that the non-linear response appeared close to the third harmonic of the pitch natural frequency of the individually moored device. Whilst the natural pitch frequencies of the devices moored in Configurations B, C and D might be different; this supports the hypothesis that pitching is a major contributor to the dynamic load on the bed lines.

For the central device the motion RAOs, shown in the Appendix in Figure 10-6, were similar to those of the outer device for all but the yaw response. Whilst it is out of the scope of this report to fully investigate the relationship between the loads and motions, the large rotations

of the device, and in particular the pitch, have been shown to be significant in the bed line tension. The interconnecting line tensions are described in Section 3.2.4 which concerns the loads and motions in extreme sea states.

3.2.2.4 Regular Wave Conclusions

The potential benefits to energy extraction achievable through interlinked arrays have been highlighted through the regular wave testing capture width curve results. These benefits only become realized on deployment of the array in a suitably matched wave climate. The performance is closely linked to the heave response of the devices; however, the frequency of the heave response is also a key factor in the array performance due to the phase difference between the device and the water column motion. The cyclic line tension profiles dramatically change in the interconnected cases; where Configuration B showed improved characteristics across nearly all frequencies tested. By reducing the number of seabed lines to one, the pitch restoring forces were reduced, resulting in large tension spikes in Configuration C, and more so in Configuration D.

3.2.3 Performance in irregular waves

Similarly to the regular wave performance calculations, the array output from the irregular sea states were calculated as an average over the test time. Figure 3-21 shows the capture width ratios of the arrays and isolated device for sea states with three values of T_p. The range of T_p values is equivalent to 0.52 Hz – 0.83 Hz and so similarities exist between the regular and irregular wave results. In general, the capture width ratios were lower for the irregular sea states than the regular cases since the irregular spectra have energy at frequencies that did not excite the devices.

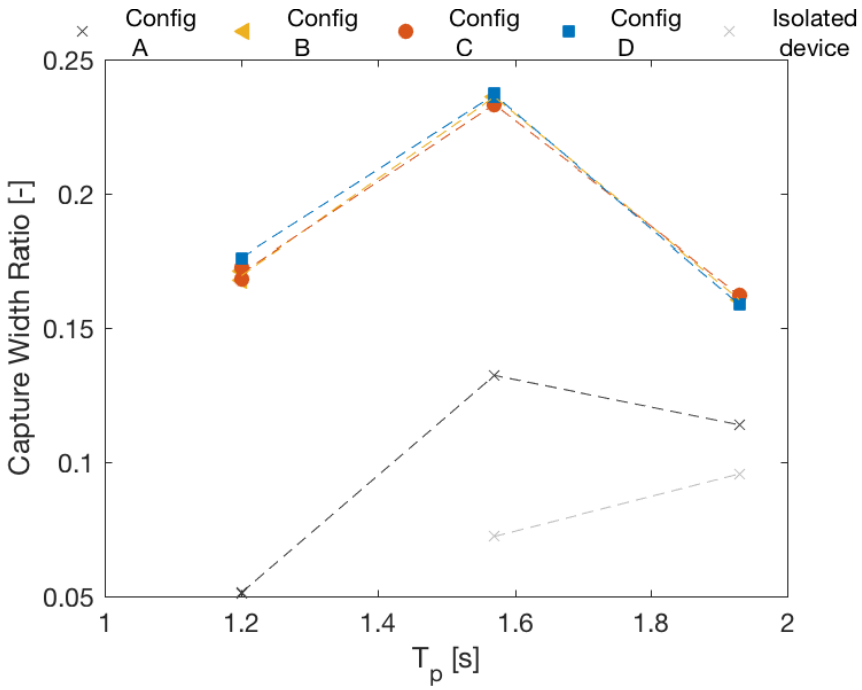

FIGURE 3-21 CWR OF THE ARRAYS IN IRREGULAR SEA STATES OF VARYING PEAK PERIOD AND CONSTANT H_S = 0.05625 M

It can be seen from Figure 3-21 that the interconnected cases had significantly larger CWRs than both the individually-moored and isolated cases. The increase in CWR from the isolated case and Configuration A should be interpreted with caution: the regular CWR curves and motion responses showed that the array configuration excited basin resonances resulting in large changes to the CWR. The largest difference in performance between the isolated device and Configuration A was at a peak period of T_p = 1.57 s, which was very close to this frequency. This difference becomes less at the higher peak period of T_p = 1.93 s suggesting that basin effects may have contributed to the differences seen.

The performance difference between the interconnected and individually moored cases was frequency-dependant and the improvement diminished towards the higher frequencies tested. At peak frequencies outside of the range tested, there may be no difference between the individually moored array performance and those of the interconnected Configurations. This should be verified with further numerical or physical modelling using different realisations of sea states with the same H_s and T_p values and an expansion the parameter space.

The heave RAOs are shown in Figure 3-22 for the irregular sea states. The mean RAO of all the devices (excluding TM1) is plotted along with a shaded envelope representing the range of all RAO values for devices in a given array. In general, the heave RAO increased as T_p increased. The isolated case had lower mean values than the interconnected arrays at all values of T_p and the ranges of heave motions were small. By contrast, the pitch motions, right-hand plot in Figure 3-22, exhibited very large ranges within the arrays.

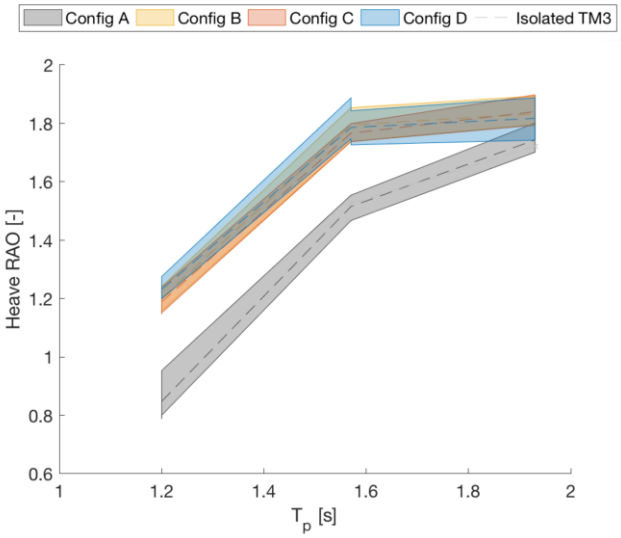

FIGURE 3-22 HEAVE RESPONSE AMPLITUDE OPERATORS, SHADING INDICATES THE EXTENT OF THE MAXIMUM AND MINIMUM

Similarly with the CWR (Figure 3-21), there was separation in the heave RAOs between the individually moored case (Configuration A) and the interconnected cases (Configurations B, C and D). Under irregular wave action, Figure 3-22 and Figure 3-21 show that the four Configurations had very similar heave RAOs but that there was a difference between the CWR of the individually moored and interconnected Configurations.

In regular waves, described in Section 3.2.2, heave motion was shown to be a reasonable predictor of CWR but the phasing of the internal water column motion should also be taken into account (details in Appendix, page 92); smaller heave motions may be associated with higher CWR if the heave of the device and the internal water column motion are out of phase. For the individually moored array (Configuration A), the phase between the device heave and the internal water column motion is a function of the device and mooring dynamics and the incident waves. For the interconnected arrays not only were the moorings changed resulting different natural periods of the arrays (see Section 3.2.1), but the influence of the up-wave devices' motions would also have been a factor.

An external force moving the devices (from the interconnection between devices) would change the phasing between the wave-induced heaving and the water column motion if the motion was along the axis of wave propagation and so Figure 3-23 shows the surge RAOs for the irregular sea states. The RAOs for all six degrees of freedom are given in the Appendix (Figure 10-10, page 90). The array average surge RAOs for the interconnected Configurations were much higher than that of the individually moored array (Configuration A) and greater than one for all sea states tested. For Configuration D, the range of surge RAOs around the array was larger than for any other Configuration despite Figure 3-21 showing no real difference between the interconnected Configurations' CWRs. For the interconnected arrays, it is not possible to attribute performance to motion in one degree of freedom.

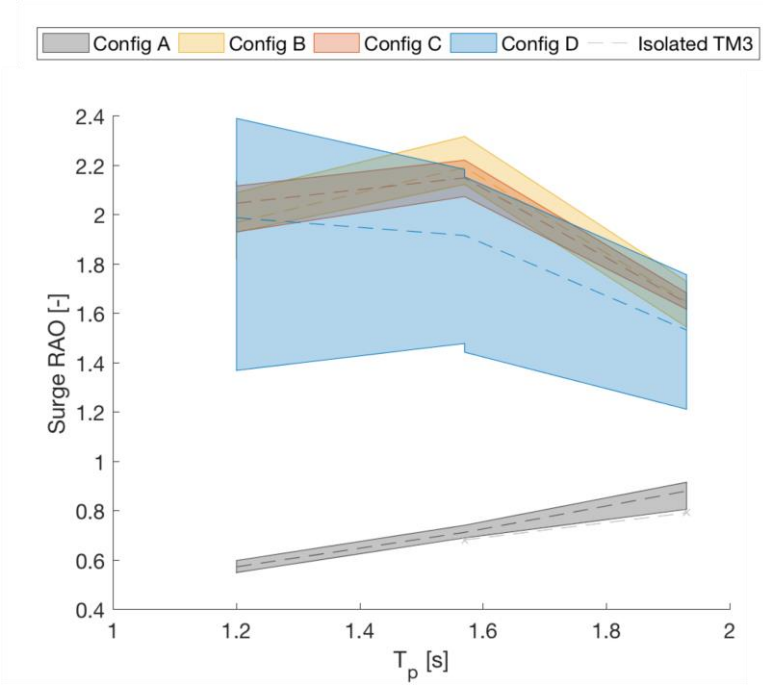

FIGURE 3-23 SURGE RESPONSE AMPLITUDE OPERATORS, SHADING INDICATES THE EXTENT OF THE MAXIMUM AND MINIMUM

3.2.3.1 Performance within the array

Array effects can be quantified by calculating an interaction factor, also known as a *q*-factor, which compares the power generated by a device in an array to the power generated by *n* isolated devices, where *n* is the number of devices in the array. Interaction factor values greater than one show constructive interaction within the array.

The *q*-factors for an irregular sea state (H_s = 0.05625 m, T_p = 1.93 Hz) were calculated for each of the array Configurations. These are plotted in Figure 3-24 along with the percentage of the total array power attributable to each device within the array. A total array *q*-factor is also listed. The individually moored array (Configuration A) had a total array *q*-factor of 1.19 showing that there was considerable constructive array interaction and this resulted in the individually moored case yielding a higher power output than five isolated devices as shown in Figure 3-14. The overall *q*-factor suggests a 20% performance enhancement due to array interaction, which is consistent with Figure 3-21. All the *q*-factors were greater than one, indicating that all the devices within the array out-performed the isolated device for this specific sea state.

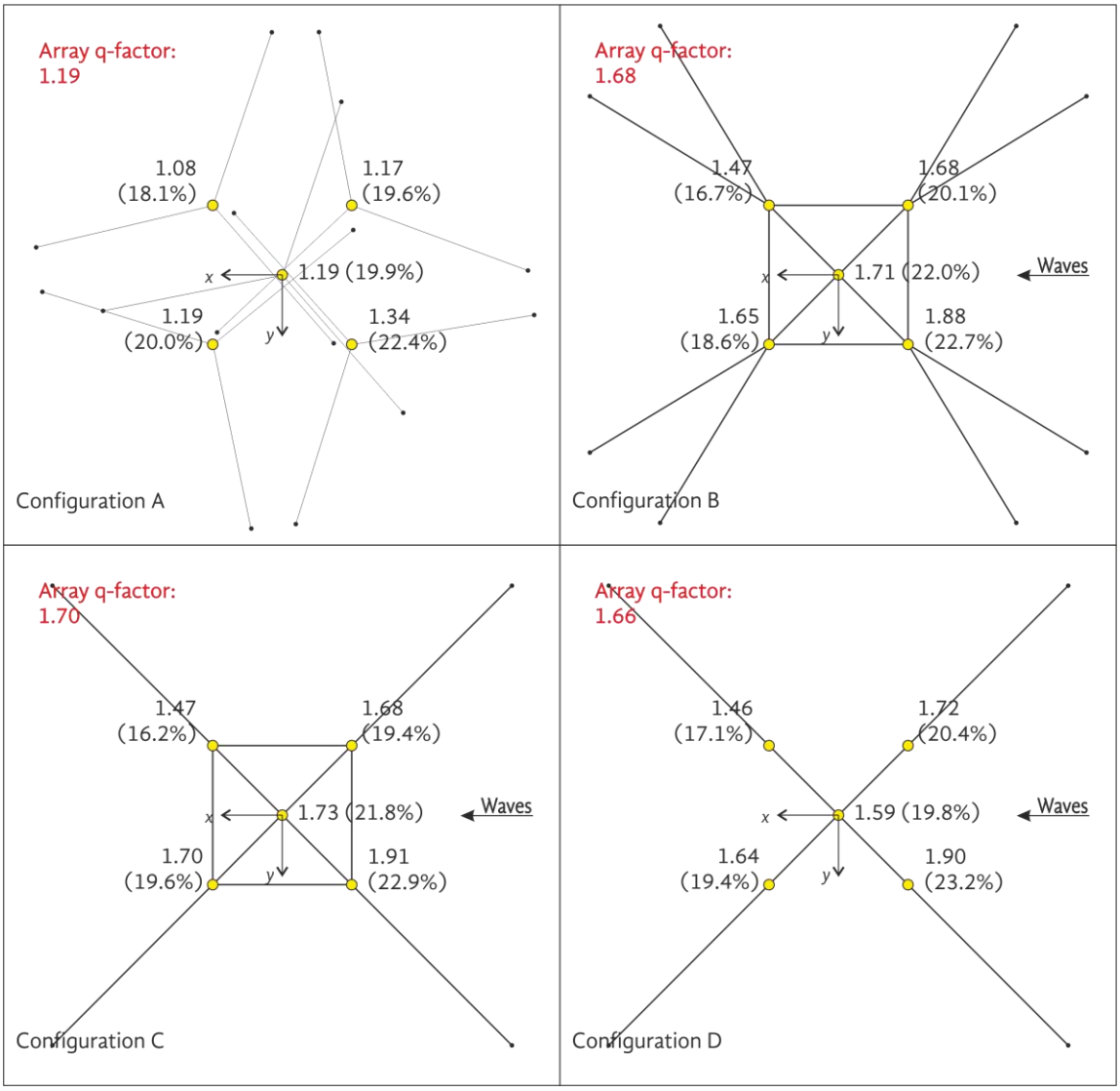

FIGURE 3-24 Q-FACTORS AND PERCENTAGE CONTRIBUTION TO OVERALL POWER OUTPUT FOR AN IRREGULAR SEA STATE WITH T_P = 1.93 S

The *q*-factors for the interconnected cases showed significant performance enhancements, as was seen in the regular conditions; all interconnected *q*-factors were higher than those of the individually moored Configuration. In addition, the front row of the array seemed to benefit more than the back row of the array. The *q*-factor of the central device (TM3) was lower in Configuration D than in the other interconnected Configurations. Configuration D had only one line connecting each corner device to TM3 which was not aligned with the direction of wave propagation. By having fewer connections between the front and the back of the array, the first row's motions would have less of an influence on the motions of the other devices. This supports the hypothesis that the other motions of the devices in interconnected arrays, not just the heave, have a significant effect on the power conversion. To capitalise on this effectively, the relationship between the internal water column motion and the device heave motion needs to be formally proven and the effects of interconnection on this relationship needs to be explored.

The difference between the power generated by the devices is further highlighted in Table 3-6, which shows the power converted by each device in Configuration A and the resulting *q*-factors for each device classified by their position in the array. The *q*-factors along the rear/middle/front axis of Configuration A, Table 3-6, show that there was a drop in power between the front and rear of the array, indicating the requirement for individual device tuning with respect to location within the array.

TABLE 3-6 POWER AND RESULTING Q-FACTORS FOR ROWS AND COLUMNS OF CONFIGURATION A FOR AN IRREGULAR SEA STATE OF T_P = 1.93 S

Power [W]	Rear	Middle	Front	Total Power [W]	q-factor
-*y*	0.07		0.08	0.1500	1.09
CL		0.08		0.08	1.16
+*y*	0.08		0.09	0.1700	1.23
Total Power [W]	0.1500	0.0800	0.1700	**0.4000**	
***q*-factor**	1.09	1.16	1.23		**1.16**

Configurations B, C and D had similar *q*-factors, both laterally and longitudinally and so Table 3-7 shows the power converted by each device in Configuration D and the resulting *q*-factors for each device classified by their position in the array. By inspecting the *q*-factors separated by the rows and columns, as shown in Table 3-7, similar trends to those of Configuration A can be seen in the power output, albeit with larger values.

TABLE 3-7 POWER AND RESULTING Q-FACTORS FOR ROWS AND COLUMNS OF CONFIGURATION D FOR AN IRREGULAR SEA STATE OF T_P = 1.93 S

Power [W]	Rear	Middle	Front	Total Power [W]	q-factor
-*y*	0.10		0.12	0.2200	1.60
CL		0.11		0.11	1.60
+*y*	0.11		0.13	0.2400	1.74
Total Power [W]	0.2100	0.1100	0.2500	**0.5700**	
***q*-factor**	1.52	1.60	1.81		**1.65**

For all the interconnected arrays, the power attenuation from front to back of the array was larger than for the individually moored case, with nearly 20% difference between front and back compared to 12%. This higher rate of power attenuation with respect to the length of the interconnected arrays suggests that the power output may be more dependent on the device spacing than in a standard individually moored array.

3.2.3.2 Annual yield

Comparing the irregular CWRs in Figure 3-21 with those reported in Figure 3-16, it can be seen that the CWR values were consistent in magnitude for a given input (peak) frequency. This suggests that performance differences between the individually moored array and the interconnected arrays are not reliant on the wave type. If this relationship holds between the regular and irregular CWR hold for the rest of the parameter space, it also implies that at $T_p \approx 1.4$ s, the CWRs would be much higher than those shown in Figure 3-21. This is significant since at full-scale (for which the equivalent energy period would be ~7.5 s), Figure 1-2 shows that just over 20% of the waves occur around this period.

Using the relationship between the CWR in regular and irregular waves, an annual yield was predicted for each Configuration using the CWR curves derived from regular wave tests and the wave scatter diagram shown in Figure 1-2. This process is described in more detail in the Appendix (page 68), where it is shown that the annual energy extraction was within ±2% of the measured values per Configuration across all the irregular sea states tested. Whilst this method relies on the assumption of linearity, it helps to put the results in context.

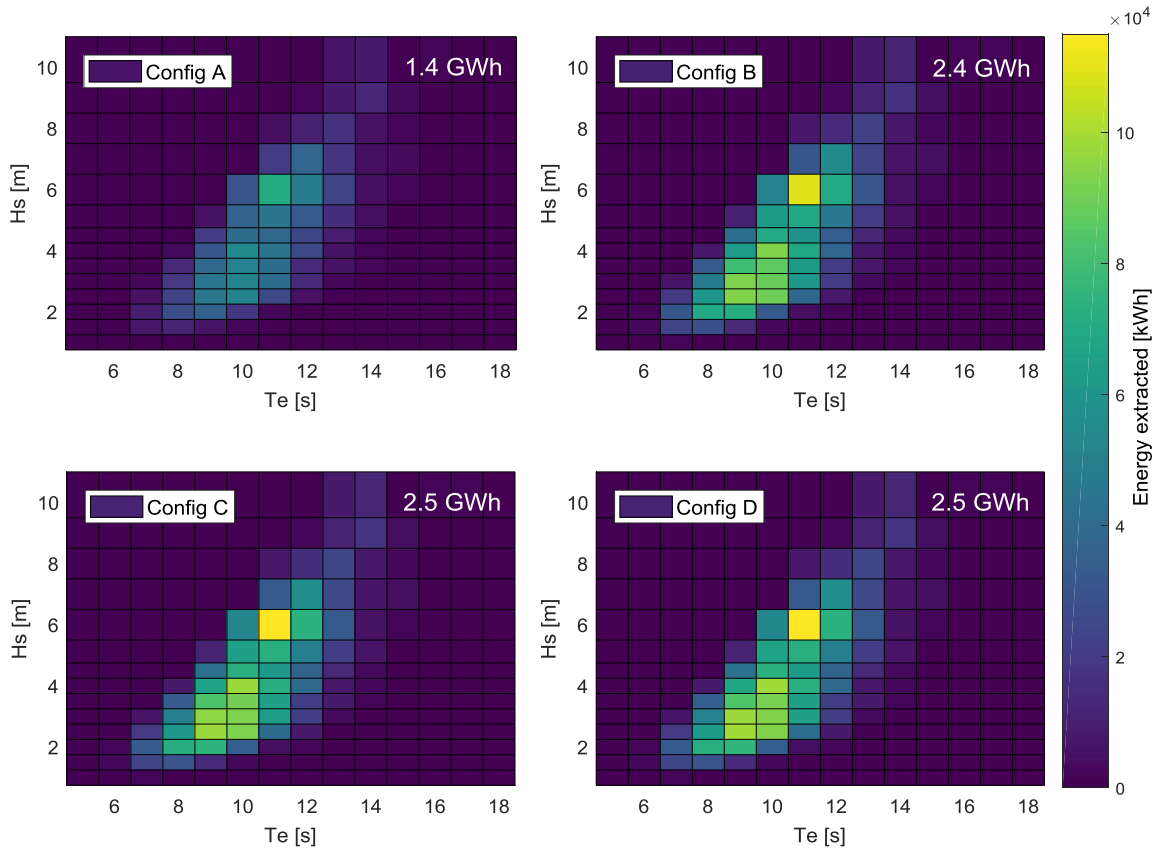

FIGURE 3-25 ENERGY EXTRACTION FOR EACH CONFIGURATION AT THE PROPOSED SITE IN PORTUGAL

A distinct difference can be seen from Figure 3-25 between the individually moored and the interconnected Configurations. The interconnected cases extract much more energy over all, particularly in the lower period sea states, as expected due to the higher peaks seen in the regular capture widths. Using the wave probability matrix given in Figure 1-2, the total annual energy available at the site was estimated to be 15 GWh, thus the overall extraction efficiencies would be 9%, 16%, 16% and 16% for Configurations A to D respectively. Five times the isolated device, representing an array with large inter-device spacing, would achieve 9% extraction efficiency. Although these efficiencies seem low, it is very difficult to achieve high efficiencies owing to the very broadband nature of the resource. To give perspective to the potential efficiency gains through interlinked compact arrays. According to Ofgem, the average UK household consumes 3300 kWh of electrical energy per year [11]. The individually moored configuration has the potential to power around 400 homes every year of service. By interlinking the devices together in any of the configurations tested the number of homes increases to circa 700.

Despite good agreement between the CWRs in regular and irregular waves, this is likely to be an overestimate. In regular waves, the incident wave height was shown to adversely affect the CWR of the rigid device array and even though it is likely that the flexible and rigid arrays had different modes of operation, it is possible that the spar buoy device performance was affected by the incident wave height. With regard to comparisons between the interconnected cases, the results suggest that the level of interconnection does not particularly alter the annual energy extraction. It is possible to significantly increase energy extraction through the interlinking of device and these theoretical predictions contextualize these improvements.

3.2.3.3 Line loads and motions

The average magnitude of the cyclic line tension in the worst-case bed line normalised by the wave elevation is presented in Figure 3-26. As with the data presented for the regular wave cyclic tension, Figure 3-18, the interconnected Configurations had lower average cyclic tension values for all sea states tested, resulting in part to the components used in the mooring lines (see Appendix 8 for details). Configuration B also had lower average cyclic line tension values than the other two interconnected Configurations, probably owing Configuration B having two bed lines per corner device, but also to the angle of the line with respect to the oncoming waves.

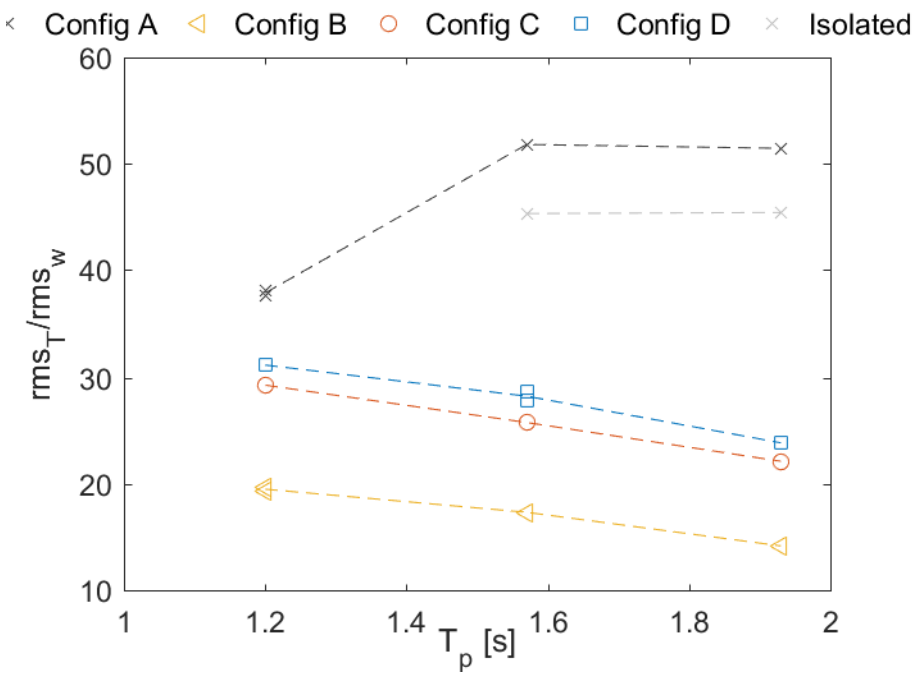

FIGURE 3-26 CYCLIC TENSION IN THE WORST-CASE SEABED LINE FOR EACH ARRAY CONFIGURATION IN IRREGULAR SEA STATES OF CONSTANT H_S = 0.05625 M

Figure 3-27 shows the pitch RAO for device TM2, which was the corner device connected to the bed lines shown in Figure 3-26, with the RAOs from the other degrees of freedom plotted in Figure 10-9 in the Appendix.

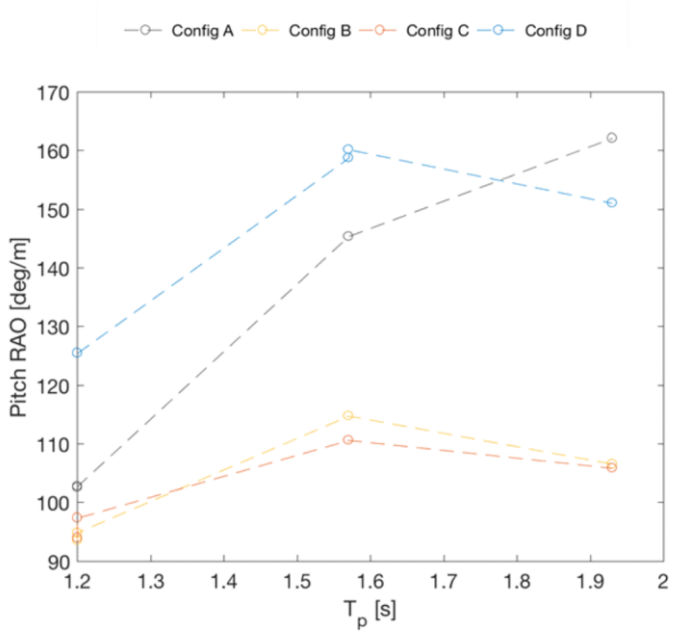

FIGURE 3-27 PITCH RESPONSE AMPLITUDE OPERATORS FOR OUTER DEVICE (TM2)

As the T_p value increased, the average pitch RAO increased for the individually moored array (Configuration A) but the pitch RAOs of the interconnected arrays had a peak at the middle value of T_p tested. In Section 3.2.2.3, the pitch motions were highlighted as a key contributor to the bed line tension but, as with the heave no longer being the only predictor of performance in the irregular waves (see page 34), the pitch motions were not solely responsible for the line tensions in the bed lines. This suggests how complicated the motions of the devices under irregular wave forcing were.

Figure 3-28 shows that the average pitch RAOs were typically larger than in regular waves but that the range of RAOs was large within the interconnected arrays. The range of pitch RAOs for Configuration A was small in comparison to those of the interconnected arrays and from this it can be inferred that the outer devices of the array (TM1, TM2, TM4 and TM5) are responsible for the large range of motions.

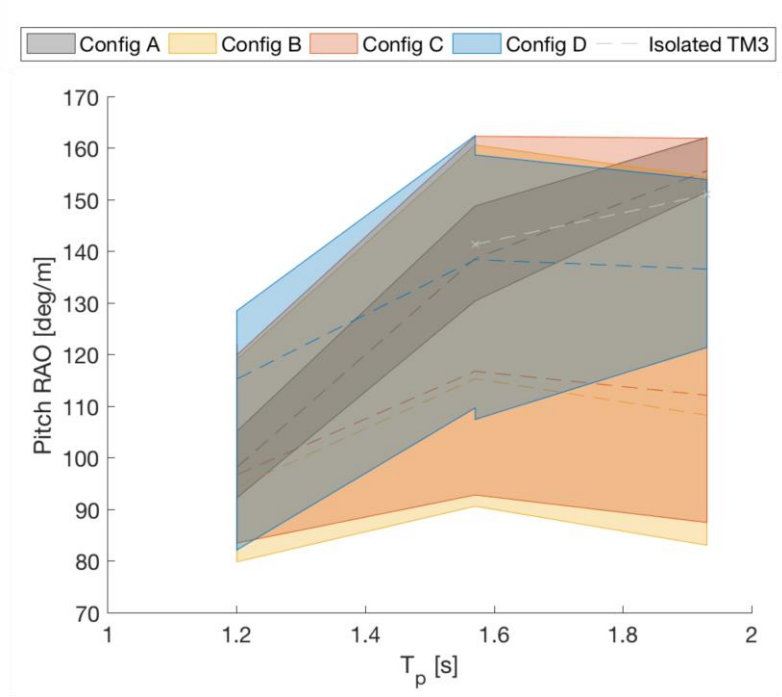

FIGURE 3-28 PITCH RESPONSE AMPLITUDE OPERATORS, SHADING INDICATES THE EXTENT OF THE MAXIMUM AND MINIMUM

To summarize, the use of interconnected mooring systems can be used to reduce the cyclic loading on the seabed mooring lines, although a greater static load will be imparted from the use of heavier clump weights and floats along the line lengths. The interconnected Configurations' bed lines used heavier chain, which will have increased the static loading but also would incur a higher cost. Since the loading did not approach values of failure, it could be that more cost-effective moorings could be designed by reducing the chain unit length and adding more weight in line as clumps.

3.2.4 Survivability in extreme seas

The survivability experiments subjected the devices to extreme irregular waves to simulate a 3-hour full-scale storm condition. Return periods of 10, 50 and 100 years were used to create the waves based on a Pierson Moskovitz spectrum. Overtopping of the devices was expected, and frequently occurred, during the experiments so performance data was not calculated for the experiments. The large motions of the devices, coupled with the overtopping events meant that some motion data had to be interpolated.

Table 3-8 gives the RMS tension values in the bed line attached to TM2 for all return periods tested as well as the RMS motions in each of the degrees of freedom for both TM2 and the central device (TM3). The difference between the TM2 bed line tension values across Configurations was dependent on the return period; for the sea states tested, longer return periods led to smaller differences between Configurations A and C. This is likely to be affected by the specific realisation of the sea states that were used for experimentation and has implications for many of the analysis of this report; these are discussed further in Section 4.

The results show that there was a significant difference in the motion response between the individually moored and the interconnected arrays for many of the degrees of freedom and for both the central and outer devices. In particular, surge was lower in Configuration A than for the interconnected Configurations, while pitch was generally higher. The four point interconnection on the device reduced the surge restriction and allowed for nearly 16% increase in cyclic surge between Configuration A and Configurations B and C. Interestingly, the removal of the square interconnections (Configuration D) appeared to limit the surge motion across all extreme sea states. The central device of Configurations B and C responded very similarly, as would be expected due to the similar line lay-out, in particular weave of the central device (TM3) was consistent across all Configurations.

TABLE 3-8 RMS MOTION RESPONSE FOR THE FRONT MOST OUTER (TM2) AND CENTRAL (TM3) DEVICE AND CYCLIC TENSION OF THE WORST-CASE SEABED LINE

Return period	**TM2**				**TM3**			
	10 years, H_s = 0.300 m, T_p = 2.72 s							
Configuration	**A**	**B**	**C**	**D**	**A**	**B**	**C**	**D**
Surge [-]	1.37	1.73	1.72	1.58	1.49	1.73	1.78	1.65
Sway [-]	0.57	0.75	0.77	0.86	0.36	0.53	0.55	0.38
Heave [-]	1.28	1.31	1.29	1.21	1.28	1.27	1.28	1.28
Roll [deg/m]	58.8	70.6	88.3	89.5	50.6	42.3	45.2	31.7
Pitch [deg/m]	184.0	168.1	170.0	177.5	220.4	175.2	181.2	166.8
Yaw [deg/m]	134.2	100.4	111.0	174.7	81.6	82.8	79.7	55.6
Tension [N]	38.2	46.1	76.3	56.9	-	-	-	-

Return period	50 years, H_s = 0.325 m, T_p = 2.91 s							
Configuration	**A**	**B**	**C**	**D**	**A**	**B**	**C**	**D**
Surge [-]	1.39	1.69	1.67	1.51	1.44	1.67	1.67	1.61
Sway [-]	0.56	0.69	0.75	0.84	0.34	0.48	0.54	0.38
Heave [-]	1.25	1.27	1.25	1.20	1.26	1.26	1.26	1.25
Roll [deg/m]	54.5	63.3	85.1	85.2	47.5	33.7	43.0	28.3
Pitch [deg/m]	182.1	163.9	161.8	160.5	201.8	169.1	170.5	164.5
Yaw [deg/m]	120.8	89.7	99.4	159.9	81.8	69.8	69.7	49.5
Tension [N]	40.9	44.9	73.7	53.4	-	-	-	-
Return period	**100 years, H_s = 0.350 m, T_p = 3.06 s**							
Configuration	**A**	**B**	**C**	**D**	**A**	**B**	**C**	**D**
Surge [-]	1.36	1.66	1.68	1.44	1.45	1.65	1.64	1.59
Sway [-]	0.51	0.65	0.69	0.80	0.41	0.45	0.50	0.34
Heave [-]	1.24	1.26	1.25	1.17	1.25	1.27	1.27	1.25
Roll [deg/m]	50.7	61.1	75.3	80.9	48.9	34.1	43.7	28.9
Pitch [deg/m]	168.1	156.2	158.7	146.5	189.5	168.3	161.9	161.0
Yaw [deg/m]	116.1	86.3	93.3	150.7	84.3	65.0	65.2	46.8
Tension [N]	43.7	44.9	67.4	55.8	-	-	-	-

As with the irregular cases reported in Section 3.2.3, it is not possible to definitively attribute the loading in the bed lines to one specific motion. Whilst the loading in the bed line attached to TM2 was highest for Configuration C across all return periods, many of the motions were either similar in magnitude or smaller than those recorded for the other interconnected Configurations.

In extreme sea states, WEC moorings are likely to experience large load spikes in addition to large cyclic loading and this is examined in Figure 3-29 for the 10-year return period sea state, which seemed to be the worst case of those tested owing to the very large single wave event mentioned Section 3.1. Figure 3-29 shows the root mean square (RMS) cyclic line tension, T_L, normalised by the RMS wave surface elevation, η, experienced by all the lines during the 10-year return period sea state with a global colour scale to represent the magnitude of the tension response. The thickness of the line is also used to describe tensions. The values of the tension for each configuration can be compared in Table 10-7, in Appendix 10.6.

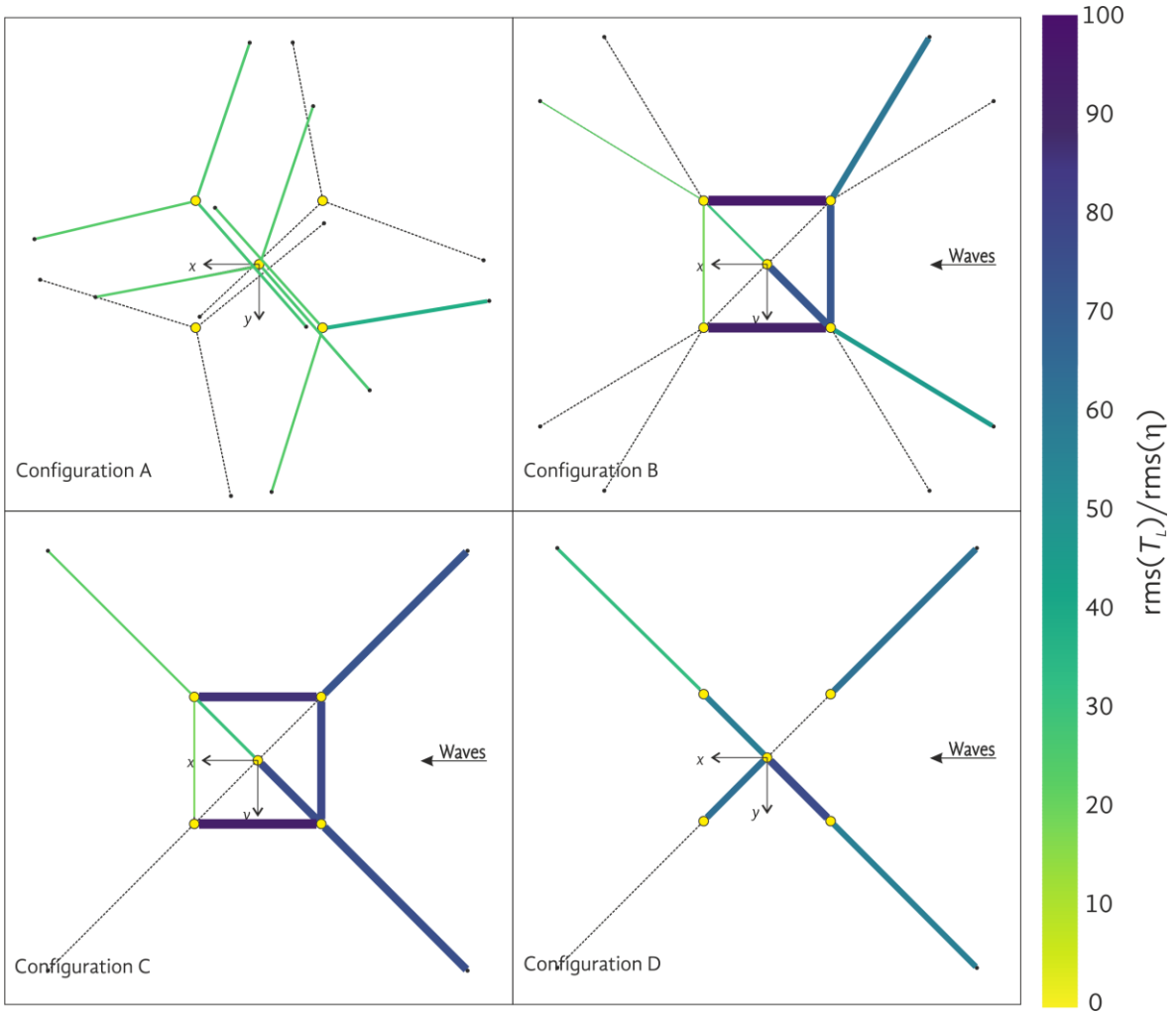

FIGURE 3-29 LINE TENSION NORMALISED BY SURFACE ELEVATION FOR THE 10-YEAR RETURN PERIOD SURVIVABILITY. DASHED LINES WERE NOT INSTRUMENTED.

Figure 3-29 shows that the interconnection of the devices increased the cyclic tension compared to Configuration A. The seabed line tension of Configuration B was increased with respect to Configuration A, as shown in Table 3-8. The largest increase in the load seen was moving from Configuration B to Configuration C, in which a seabed line was removed. This resulted in an increase in line load of around 66%. High cyclic tensions were recorded in the interconnecting lines, particularly in the square connections for Configurations B and C. Snatch loading was seen for many of the interconnecting lines, in particular those parallel to the direction of wave propagation (square interconnections).

Table 3-8 shows that the removal of the square interconnections reduced the surge response of both TM2 and TM3 in Configuration D compared to Configuration C for all sea states. This seems counter-intuitive but by removing the square interlinking lines, large excursions of the up-wave devices were less likely to propagate through the array. This may help to explain why the up-wave bed line tension was reduced in Configuration D compared to Configuration C: when large waves hit devices at the back of the array, the load was not transmitted as directly to the up-wave line. Figure 3-30 shows an image of Configuration C during the 10-

year return period sea state, with waves propagating from right to left of the image. Highlighted in the image are the square interconnection lines around the point of snatch. It is clear that there is a significant pitching of all devices in the array, in particular TM3 and that there was also significant roll and surge motion. From the video recordings, it is possible to see the abrupt end to the surge motions of the devices at the rear of the array owing to line snatch.

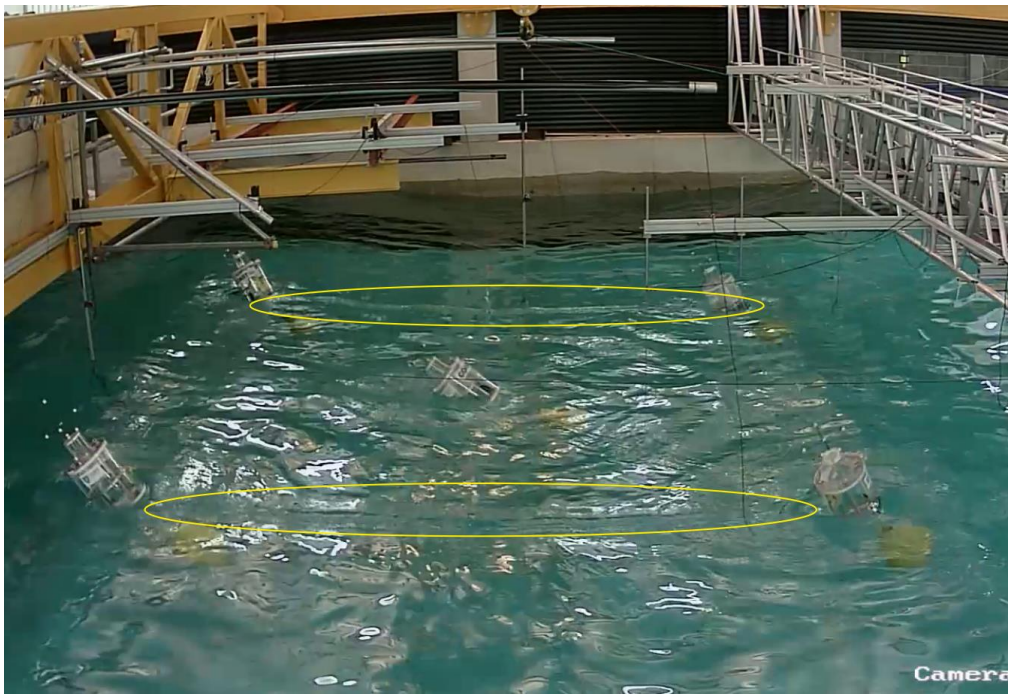

FIGURE 3-30 CONFIGURATION C IN THE 10-YEAR RETURN PERIOD SEA STATE

To summarize the findings of the line loading in extreme sea states, the results show that interconnecting of devices is possible but does result in higher cyclic loading compared to a similar individually moored array. Results particularly highlighted the interconnecting lines as high cyclic tension areas. This indicates that interconnecting mooring lines need to be specifically designed to their intended location within an array. This provides opportunity for cost reductions in that more cost effective materials, with lower fatigue life characteristics can be used in areas of low cyclic tension.

4 DISCUSSION

Experiments were conducted on two types of array – a flexibly interconnected array of spar buoy devices and a rigid array of coaxial OWC devices. For the flexibly inter-moored devices, three inter-moored Configurations were tested, each with a different level of interconnectivity. Each array was compared to the baseline of a single corresponding device in the same location as the geometric centre of the array. The flexibly inter-moored array was also compared to an array of five devices individually moored in the basin.

The performance of the devices was assessed, via the CWR, in regular and irregular waves and motions and loads on the mooring line were also recorded. The experiments also included experiments with extreme sea states to characterise the motions and mooring line loads in storm conditions.

In general, the interconnection of the devices, whether flexible or rigid, led to increases in the CWR of more than 50%. Even without considering the potential savings on the mooring line materials costs, this is a significant result.

For both the flexible and rigid arrays, array effects were positive for the chosen spacing. It was shown in Section 3.2.2 that the central device in the individually moored array (Configuration A) had a higher CWR than the isolated device. This was expected since the spacing of the arrays was chosen to permit favourable array interactions. The rigid device also showed increase in the CWR for each of the devices in the array in comparison with the single device.

4.1 Interconnection positively affects the power capture

The goal of WP6 was to examine the potential for savings in mooring infrastructure costs and to investigate the effects this had on the performance, device motions and mooring line loads. For the rigid device array for which the device spacing remained constant, it was assumed at the beginning of the project that there would be a performance benefit equal to the array effect. However, for the flexibly moored devices, the hypothesis was that potential cost savings would be mitigated by an overall drop in performance owing to the interconnections. However, the performance differences resulting from interconnection have proven not only to be positive but to be significantly higher than the array effect in the case of the flexibly moored devices.

Sections 3.1 and 3.2 showed that both arrays were found to have a neutral or positive effect on power capture compared with their respective isolated devices. The magnitude of the benefit was related to the position of the device in the arrays. For the rigidly-connected devices, that were constrained to move as a single unit, the corner devices had larger CWRs compared with the central device. There was evidence that the front two devices had larger CWRs at certain regular wave frequencies and certain peak frequencies for the irregular waves. Whilst the uncertainty in the measurements suggests that this would benefit from

further investigation, the trends corroborate those seen for the flexibly-moored arrays; that the first row of the array had larger CWRs.

Given that for the experiments conducted, there was no condition in which a device in the rigid array performed worse that the isolated device, it was no surprise that the total array performance exceeded five times that of the isolated device. For the regular waves, the rigid array CWR not only had a larger peak value, for the larger amplitude waves it was also more broad-banded than five times the isolated device. For the irregular waves, which are a more realistic appraisal of the device performance, the rigid array showed higher CWRs in the centre of the range of peak periods tested, with no benefit over five times the isolated device at the lowest peak period (T_p = 1.2 s).

For the flexibly interconnected arrays, whilst the initial array effect was negligible for the regular waves, it was significant for the irregular waves (q-factor = 1.19), indicating that there was a non-linear element to the array interaction. However, the most significant result of this study is that the array effects are small compared to the effects of inter-mooring the devices in the array with q-factors in excess of 1.9. Surprisingly, the level of interconnection made little difference to the array as a whole operating in irregular seas. Differences were seen within the array, as with the rigid device, and this was affected by the level of interconnection between the devices.

The devices and the chosen array geometries were not proposed to be optimal solutions to either the design of OWC WECs or array layouts. In Section 3.2.3, the array effect of the interconnected devices in irregular waves was quantified by way of a q-factor. Whilst a value of 1.16 indicated a positive effect for the individually moored array (Configuration A), q-factors in excess of two were the result of an array optimisation via genetic algorithm procedure [12]. For the interconnected Configurations, the q factor was 1.96. In numerical simulations of three buoys, the ratio of the q-factors from an inter-moored to individually moored configuration was found to be 1.09, far smaller than recorded here but deemed significant by the authors [13]

By interconnecting the devices, essentially the interaction factor is altered by changing the way the devices move and respond under wave forcing. It is unclear at this stage whether these changes are a result of a spatial change, a temporal change or both. For the flexible arrays, an example of a spatial change would be the displacement of the devices relative to the incident waves, resulting in an altered phase between the device heave and the water column motion. The q-factor results from around the arrays given in Table 3-6 and Table 3-7 indicate that this is unlikely to be the cause of the larger CWRs seen for the interconnected Configurations as there was a larger difference in power capture between the front and rear rows of the arrays for the interconnected cases than for the individually moored array. As it was, the interconnected Configurations' smallest q-factors were higher than the largest q-factors for the individually moored array. Furthermore, the level of interconnection made very little difference to the CWRs of the flexible arrays in regular or irregular arrays. This was an unexpected result, especially when the motion response amplitude operators (RAOs) presented in the main body and the Appendix indicated that the devices behaved quite differently. The RAOs is a measure of the average response as a function of the incident wave

height and so is a general measure of the motion that relies on linear theory. It does not capture how the devices moved in time relative to each other and so it may be that the key to the interconnected Configurations' performance is due to temporal factors not captured with the current analysis. It is recommended that further study be undertaken to determine the cause of the increased CWRs.

Whilst average performance, motions and line loads were considered throughout much of the report, if temporal effects are important for high CWRs for the interconnected Configurations, the results must be considered in the light of sea state realisation. In the irregular and extreme wave experiments, only one instance of sea state was used per H_s and T_p value. While this allowed a direct comparison between the Configurations under the same incident waves, it may mask the effects that the random phasing of the waves had on the results. If a link between the device motions and the performance could be established, numerical models could be used to explore how arrays might perform in different realisations of the same sea state.

For the rigid array, for which the inter-device spacing did not change, the shared platform imposed different dynamics on the devices. This meant that although array effects were unlikely to be negligible, the motion of the whole platform also had a role. This could be classed as a combination of spatial and temporal effects. It would be interesting to compare the rigid array performance with that of a fixed array of the same devices. As the motions of the rigid array played a role in the power production, it is perhaps unfair to compare the results of the rigid array with those of the isolated device because their masses were so different. It should be possible to design a single isolated device that has the same mass and mass distribution to make a fairer comparison but this would either require materials with extremely large density values or compromises in the design that would reduce the similarity of other parameters. Numerical modelling would be ideally suited to this task but simulating both the motion and the internal water column remains a challenge for numerical models.

The CWRs for the rigidly and flexibly interconnected devices had peaks in the range of 0.15 – 0.25 for the irregular sea states. Since the CWR is the same at model-scale as at full-scale, these values can be compared to those of existing devices. Babarit [14] created a database of CWRs for various WECs from data available in the literature. Whilst this data should be used as a guide only, it was found that the mean CWR for OWCs of all types used in the study was 0.29 with a standard deviation of 0.13. Values reported for floating OWCs had a range of CWR ratios from 0.1 to ~0.22. This shows that not only do these experiments demonstrate credible capture width ratios but that they show pathways to the improvement of current floating OWC technology through the interconnection of devices.

4.2 Adverse effects

The caveat to the benefits seen with interconnections of arrays is the effects on the line loads and motions of the devices. For the flexibly interconnected configurations, the moorings were specific to each array and were designed to give the same static surge stiffness. Typically, as the interconnection decreased, chains and clump weights used were heavier, implying a greater material and installation cost. In the irregular sea states, Section 3.2.3 showed that

interconnection of the devices led to lower average cyclic loads. This has positive implications for the fatigue resistance of the line so the extra material cost may be outweighed by a longer service life.

In the extreme sea states, the cyclic component of the load was higher in the interconnected cases than for the individually moored configuration. In particular, the lines joining the devices underwent high cyclic loads and, from observation, the lines often snatched. Snatch loading of mooring line increases the tension on the lines by a considerable amount and can lead to failure. Removing the square interconnection lines, so that the corner devices were only tethered to the central device, as in Configuration D, decreased the loads in all of the lines since those that remained were not perpendicular to the incident wave crest. In a real deployment, the waves may have a predominant direction of travel but this should not be relied upon to prevent line snatch.

4.3 Performance in the field

The flexibly interconnected arrays have an obvious major drawback: sharing lines to reduce infrastructure costs increases the risk of a line failure having knock-on effects. Within the array configurations tested, the failure of a sea bed line would likely destroy the array if left unchecked. The design of future array deployments should investigate mooring line redundancy or a "fail safe" procedure, although these may outweigh any initial cost savings.

For the rigid array, the loss of a single mooring line would have less serious consequences. Even in the extreme wave events shown in Figure 3-10, the catenary moorings were only partially lifted. Should one of the up-wave catenaries fail, it is likely that a single up-wave catenary line would be adequate to hold the device in operational sea states, although this would have to be investigated for extreme waves.

For the flexibly interconnected devices, the line loading data have shown the necessity of designing a mooring system suitable for the array in question. This limits potential array expansion as, similarly to the rigid array, it will not be possible to attach more devices to an existing array. This has ramifications for the risk, capital costs and installation times associated with a project: an entire array of device would have to be deployed in one phase which would be costly and difficult owing to the windows in which the weather conditions permitted installation. A possible solution would be to deploy individually moored devices and use subsequent weather windows to interlink them.

The experiments conducted as part of WP6 only considered waves propagating on one direction. While there may be a prevailing wave direction associated with a particular site, the energy will typically fall within a range, e.g. for Leixões most of the energy recorded in 2009 was in a band of approximately 30° [15]. Incident wave angle was considered in [13] for time domain simulations of arrays of inter-moored buoys and showed that while a change of 30° compared to the axis of the array led to lower ratios of q-factors (inter-moored / individually moored), the ratios were still greater than one. This suggests that some variation in the prevailing wave direction will be tolerable from a performance point of view.

While the experiments here have shown that the interconnection of devices whether rigidly or flexibly can have benefits to the performance, the mechanisms for this are unclear. It is necessary to establish a link between the motions and the performance and between the moorings and the whole system dynamics to properly design future arrays to capitalise on the benefits.

To make a deployment of WEC attractive, it will need to generate substantial electricity. This can be done in two ways: scale up WEC devices so they capture more energy per device or create arrays of multiple devices. For the two devices considered here, both OWC, the conversion of energy relies on resonance of the internal water column and as such there is a practical limit to the size of the device. Ideally, the device would have a resonant period that was well matched to the wave resource at a particular site. For a typical OWC, the resonant period of the water column, T_{nat} is given by the following equation where g is the acceleration due to gravity and L_1 is the effective length; the distance between the still water line and the bottom of the device:

$$T_{nat} = 2\pi\sqrt{\frac{L_1}{g}}$$

For the spar buoy used in the flexible arrays, the resonant period of the water column at full scale was given as 11.3 s, equivalent to 1.8 s at 1:40 scale. At Leixões, nearly 93% of the available energy occurs at energy periods between 5 s and 11 s, Figure 1-2 and so increasing the size, which would increase the resonant period, may not be a sensible option. A very simple Froude scaling was used to examine the scaling of the spar buoy devices and Table 4-1 shows how increasing the effective length by 10% would lead to 40% increase in power but 33% increase in mass. Increasing the resonant period of the OWC by 10% would nearly double the power and the mass would increase by 77%. Bigger devices are preferable as the power and mass scale at different rates and Table 4-1 shows that the power per unit mass of the devices increases as the device gets bigger.

TABLE 4-1 POWER PRODUCTION AT DIFFERENT SCALES

	Mass	Effective length [m]	*T* [s]	*P* [W]	[W/kg]
1:40	18 kg	0.588	1.8	0.281	0.0156
Full scale	1183 tonnes	31.9	11.3	113540	0.0960
10% length increase	1575 tonnes	35	11.9	158498	0.1007
10% period increase	2096 tonnes	38.6	12.5	221258	0.1056
5 inter-connected full-scale devices	5916 tonnes	(31.9)	(11.33)	1135403	0.1919

(1) Based on regular wave with full-scale period of 1.53 s and full-scale height of 2 m, moorings not taken into account

The problem with this, and for all devices that use resonance, is that there will be a maximum size that the device can be for a given wave climate, especially when the probability of occurrence of the waves is taken into account. At Leixões, less than 2% of the wave energy

occurs at energy periods greater than 12 s, which would probably exclude the example device with a 12.5 s resonant period in Table 4-1 on the basis of economic unviability.

The alternative is to create arrays of WEC devices and this study has shown that interconnected arrays of WECs can have large benefits to the power production. Table 4-1 also includes a 5-device array example for which the CWR was twice as high as the isolated device at that point in the regular wave parameter space. The power generated is 10 times higher for five times the increase in mass, although this does not take into account the moorings, and consequently the power per unit mass of the array is higher than for the other examples given in Table 4-1. Floating OWCs were identified as the best out of four types of WEC in terms of power per unit mass [16]

Given the simple analysis in Table 4-1 and the annual yield calculation in Section 3.2.3, one may conclude that to compete with other offshore renewables, an array of 50–100 devices would be needed. For the rigid array, a full-scale array with the same pattern of devices would contain 61 units if there were six on each side. Assuming the same spacing between devices, such an array would be 157 m in both length and width: comparable with an oil rig platform. If the array were not square, one could imagine an array comparable in size to an FPSO vessel, which, while not moored in the most energetic seas, has mooring systems that are already proven. As yet unexplored are the effects of the rotations of the rigid array and the subsequent effect on the power produced. Rotations will result in larger motions of the devices the further the device is from the centre of rotation, whilst this may adversely affect the power available to a device, it also has implications for inspection and maintenance.

5 CONCLUSIONS

Wave energy conversion is an area of technology yet to reach maturity and to date, the cost of wave energy remains high. The Horizon 2020-funded WETFEET project identified several breakthrough solutions that were conceived to reduce the costs of wave energy to progress research and industry to the next level. This report covered the array breakthrough: sharing of mooring hardware and co-locating devices in two types of inter connected arrays.

Physical model experiments have shown that array interconnection has the potential to significantly increase power production and therefore reduce the costs associated with wave energy. For the flexible arrays, the benefits far outweighed the array effects, meaning that the interconnection was responsible for the increase. Unexpectedly, the level of interconnection made very little difference on the performance improvement, despite changes in device movement. This is encouraging for future developers as it suggests that many viable solutions to the problem of interconnection exist. Coupled with the fact that the array layouts investigated here were not chosen with hydrodynamic considerations in mind, the applicability of these results should be high.

Both the rigid and flexible arrays used devices that were oscillating water columns. Despite the rigid array having low motion compared with the flexible array, interconnection altered the motions of the arrays and this is what led to performance improvements. What remains unknown is whether spatial or temporal movements of the arrays are more important. For

other device types, particularly those that do not rely on resonance, it may be that interconnection would not offer performance benefits. However, inter-mooring of devices may still be an attractive solution to reduce capital expenditure if it could be shown that motions of such devise (for example, over topping devices) were not compromised.

The downside to the inter-mooring is the large line loads experienced by the arrays but particularly in the interconnecting lines where snatch loading was evident. It was shown that the up-wave lines experienced larger loads than those at the rear of the array but that the type of interconnection could reduce line loads; more study is needed to determine suitable interconnection strategies that allow for a spread of incident wave directions. Extreme wave events led to the interconnecting lines to snatch as the waves were loading two devices connected long the direction of wave forcing and so the least connected array, which had no interconnecting lines aligned with the wave propagation direction, had lower interconnecting line loads. Multiple stiffness mooring lines or added-in components such as springs and mooring compensators could be used to reduce the snatch loading in interconnecting lines, and this underscores the need to design appropriate mooring systems. Certainly, this will be more complicated for arrays than for single devices but, as stated previously, the actual interconnection type may not be a restrictive criterion for performance gains. If predicted mooring line loads are sufficient to cause a project to stall, there may be a practical limit to the number of devices that can be inter-moored with a given array geometry.

The rigid arrays showed less improvement than the flexible arrays did and it was not possible to distinguish array effects from the effects of the motions of the platform, however their simpler mooring lines, which would offer substantially lower installation costs than for a flexible array, and significantly lower line loads make the rigid array an attractive option, particularly in the shorter term. The benefit of rigid arrays of OWCs may stem from each sub-unit having the motion of a larger body imposed on it; amplifying the wave resource and so the dynamics of the whole array need to be considered when identifying a deployment location. If this is the case, rigid arrays are likely to be more narrow-banded than the flexible arrays, although sub-units with different resonant frequencies would mitigate this.

The experiments of WETFEET WP6, while only being a first step, have shown that array interconnection should be considered a breakthrough for the wave energy industry in its journey to make wave energy feasible through lower costs.

6 BIBLIOGRAPHY

1. Perez, C. and G. Iglesias, *Integration of wave energy converters and offshore windmills*, in *International Conference on Ocean Energy*. 2012: Dublin, Ireland.
2. *D6.1 - Analysis of different potential configurations of non-rigid inter-moored devices*, in WETFEET project. 2016
3. IRENA, *Wave Energy Technology Brief*, in 2014
4. Low Carbon Innovation Coordination Group, *Marine Energy Summary Report*, in Technology Innovation Needs Assessment. 2012
5. *D6.2 - Analysis of different potential configurations of rigidly inter-moored devices*, in WETFEET project. 2016
6. *D6.3 - Report on the 1:40 physical models*, in WETFEET project. 2017
7. *D2.1 Design and specification of an OWC able to integrate the negative spring*, in WETFEET project. 2016
8. Gomes, R.P.F., J.C.C. Henriques, L.M.C. Gato, and A.F.O. Falcão, *Hydrodynamic optimization of an axisymmetric floating oscillating water column for wave energy conversion.* Renewable Energy, 2012. **44**: p. 328-339.
9. IST, *OWC_Spar_buoy_WETFEET12x36_15mm_toPU_2016-06-03.pdf*, in *WETFEET project*. 2016, Instituto Superior Técnico. p. 2.
10. *D6.4 - Validated numerical simulation of hydrodynamic interaction between devices for different compact array layouts*, in WETFEET project. 2017
11. OFGEM, *Typical domestic energy consumption figures*, OFGEM, Editor. 2011, OFGEM.
12. Child, B.F.M. and V. Venugopal, *Optimal configurations of wave energy device arrays.* Ocean Engineering, 2010. **37**(16): p. 1402-1417.
13. Vicente, P.C., A.F. de O. Falcão, L.M.C. Gato, and P.A.P. Justino, *Dynamics of arrays of floating point-absorber wave energy converters with inter-body and bottom slack-mooring connections.* Applied Ocean Research, 2009. **31**(4): p. 267-281.
14. Babarit, A., *A database of capture width ratio of wave energy converters.* Renewable Energy, 2015. **80**: p. 610-628.
15. Bento, A.R., E. Rusu, P. Martinho, and C. Guedes Soares, *Assessment of the changes induced by a wave energy farm in the nearshore wave conditions.* Computers & Geosciences, 2014. **71**: p. 50-61.
16. Babarit, A., J. Todalshaug, A. Kurniawan, T. Moan, and J. Krokstad, *Power Absorption Measures and Comparisons of Selected Wave Energy Converters*. Vol. 5. 2011. 437-446.
17. Lamont-Kane, P., M. Folley, and T. Whittaker, *Investigating uncertainties in physical testing of wave energy converter arrays*, in *10th European Wave and Tidal Energy Conference* 2013: Aalborg, Denmark.
18. Mansard, E.P.D. and E.R. Funke. *The measurement of incident and reflected spectra using a least squares method*. in *17th Conference on Coastal Engineering*. 1980. Sydney, Australia: American Society of Civil Engineers.
19. Collins, K.M., G. Iglesias, D. Greaves, A. Toffoli, and S. Stripling. *The new COAST laboratory of Plymouth University: A world-class facility for marine energy*. in *ICE Coasts, Marine Structures and Breakwaters Conference*. 2013. Edinburgh.
20. O'Boyle, L., B. Elsaesser, M. Folley, and T. Whittaker, *Assessment of wave basin homogeneity for wave energy converter array studies*, in *9th European Wave and Tidal Energy Conference*. 2011: Southampton, UK.

APPENDICES

7 Physical model construction

7.1 Rigid devices

The properties of the full-scale moorings and devices are given in Table 7-1.

TABLE 7-1 FULL-SCALE PARAMETERS OF THE COAXIAL OWC

Parameter	Single device	Array
L [m]	58.0	43.0
D [m]	48.0	33.0
M including ballast [tonnes]	3039	18818
CoB to MWL [m]	22.6	24.2
CoM to MWL [m]	26.3	27.9
Mooring line length [m]	256	233
Anchor radius [m]	240	240

BASED ON A WATER DENSITY OF 1025 KG/M^3

Table 7-2 gives an overview of the physical parameters for each of the test models built. It was deemed more important to achieve values with small variation between the models than to adhere to the idealised values, so that model effects were small compared to array effects.

TABLE 7-2 PHYSICAL PROPERTIES OF THE FULL-SCALE, IDEALISED 1:40 SCALE AND CONSTRUCTED MODELS

	Isolated device with heave plate			Array with ballast plate		
Parameter	Idealised 1:40 scale	CAD model	Physical model	Idealised 1:40 scale	CAD model	Physical model
L [mm]	1450	1451	**1457**	1075(1)	1075	**1080** (mean value)
D [mm]	1200	1206(2)	1180(3)	837	840(2)	853 – 880(3)
Mass, M [kg]	44.7	42.3	**43.6**	231	232	**237** (05/10/2017) **243** (20/10/2017)(4)
I_{xx} [kg m^2]	2.81	2.79	n.d.	45	39.3	n.d.
CoB to MWL [mm](5)	565	568	n.d.	547	n.d.	n.d.
CoM to MWL [mm](6)	657	657	635	699	689	n.d.
Base of model to CoM [mm](7)	168	168	**170**	126	135	n.d.
Plate width [mm]	375	375	**374.5**	1061	1061	**1060**
Top of plate to fairleads [mm]	168	/	**168**(8)	168	/	**168**(8)

NOTES ON VALUES
VALUES IN BOLD FALL WITHIN OF THE RANGE OF VALUES SPECIFIED FOR THAT PARAMETER
(1) L FOR ARRAY TAKEN TO BASE OF DEVICES SINCE BALLAST PLATE DIMENSIONS WERE NOT ACHIEVABLE GIVEN MATERIALS BEING USED
(2) CAD DRAUGHT ESTIMATED USING THE ENCLOSED VOLUME OF THE MODEL AND THE MODEL MASS
(3) PHYSICAL MODEL DRAUGHT VALUES CHANGED OVER TIME OWING TO WATER INGRESS, SO ARE GIVEN FOR GUIDANCE ONLY
(4) EXTRA MASS WAS A RESULT OF TRIM WEIGHTS AND EXTRA FOAM USED TO GET DESIRED DRAUGHT DESPITE WATER INGRESS
(5) MWL IS IN REFERENCE TO THE VALUE OF DRAUGHT GIVEN IN THAT COLUMN
(6) COM VALUES ARE TAKEN FROM THE BASE OF THE DEVICE NOT INCLUDING ANY BALLAST PLATES
(7) DISCREPANCY IN CAD MODEL MAY BE DUE TO DEVIATION IN PROPERTIES OF FASTENERS
(8) FAIRLEADS WERE RUNG NUTS SCREWED ONTO AN EMBEDDED THREAD CENTRED ON A POINT 168 MM FROM THE BASE OF THE DEVICE

TABLE 7-3 MOORING CHAIN SPECIFICATION AND MEASURED VALUES

Mooring line	Isolated device Target length [m]	Isolated device Measured length [m]	Isolated device Measured dry mass [kg]	Array Target length [m]	Array Measured length [m]	Array Measured dry mass [kg]
NE	6.367	6.370	0.452	5.809	5.812	1.693
SE		6.374	0.452		5.806	1.695
SW		6.368	0.452		5.804	1.699
NW		6.375	0.454		5.806	1.694

NOMINAL DIAMETER FOR THE ISOLATED DEVICE MOORINGS CHAINS: 2 MM; FOR THE ARRAY LINES: 4 MM. THE LENGTH OF THE FORCE SENSOR AND MOUNTING SHACKLES ADDED AN EXTRA 68 MM TO THE OVERALL LENGTH OF THE LINE AND THIS WAS NOT ACCOUNTED FOR WHEN CUTTING THE CHAIN.

7.2 Spar buoys

Figure 2-5 shows an image from the CAD model of the device and a photograph of the completed spar buoy model. The model consisted of an aluminium ballast cone, which was solid in the semi-toroidal section at the base and hollow in the conic section. The main OWC chamber was an acrylic tube that was bonded into the bottom section. Around the main OWC tube, a larger tube, the floater, was mounted on an inverted aluminium cone. Within the floater, two aluminium spoked discs held four lengths of threaded bar onto which the upper ballast was screwed. An acrylic lid with o-ring sealed the floater and an orifice plate was screwed onto the top of the OWC chamber. Mooring line fairleads, made from UHMWPE rope (Dyneema), were attached to the floater via a large diameter hose-clip.

Off the shelf components and materials were used for the physical models where possible and this resulted in the relaxing of some of the Froude scaling on the geometry, in particular the outside diameter of the OWC main tube. Parameters were given an acceptable range of values [6] as follows:

- Mass: ±5% (17.93 kg – 19.81 kg, with respect to CAD model)
- CoM location:±5% (397 mm – 439 mm, with respect to base of idealised model)

- I_{xx}: ±20% (2.54 kg m^2 – 3.80 kg m^2, with respect to idealised model)

A goal of ±5 mm was used for the remaining length scales.

Table 7-4 gives an overview of the parameters for each of the test models built. It was deemed more important to achieve values with small variation between the models than to adhere to the idealised values, so that model effects were small compared to array effects. Froude scaling was used to calculate the model-scale parameters.

TABLE 7-4 PHYSICAL PROPERTIES OF THE FULL-SCALE, IDEALISED 1:40 SCALE AND CONSTRUCTED MODELS.

Parameter	Idealised 1:40 scale	CAD model TM1-5	Physical test models TM1	TM2	TM3	TM4	TM5
L [mm]	1275	1275 (1275)	**1275**	**1276**	**1277**	**1274**	**1275**
D [mm]	900	894	890	888	890	887	887
Mass, M [kg]	19.022	18.87 (18.87)	**18.73**	**18.77**	**18.92**	**18.83**	**18.74**
I_{xx} (I_{yy}) [kg m^2]	3.170	3.84 (3.89)	5.24	7.16	**3.86**	6.12	6.91
CoB to MWL [mm]	451	454	n.d.	n.d.	n.d.	n.d.	n.d.
CoM to MWL [mm]	482	476	**481**	**475**	**470**	**476**	**475**
Base to CoM [mm]	418	412 (418)	**409**	**413**	**420**	**411**	**412**

VALUES IN BOLD FALL WITHIN OF THE RANGE OF VALUES SPECIFIED FOR THAT PARAMETER.
DRAUGHT MEASUREMENTS ARE CONSIDERED TO HAVE AN UNCERTAINTY OF ±2 MM, OTHER DISTANCE MEASUREMENTS ARE ±1 MM.
N.D. = NO DATA; NOT MEASURED
DISTANCES RELATING TO THE MWL FOR THE CAD MODELS ARE RELATIVE TO THE CALCULATED MWL POSITION

8 Spar buoy mooring line properties and configurations

8.1 Isolated device

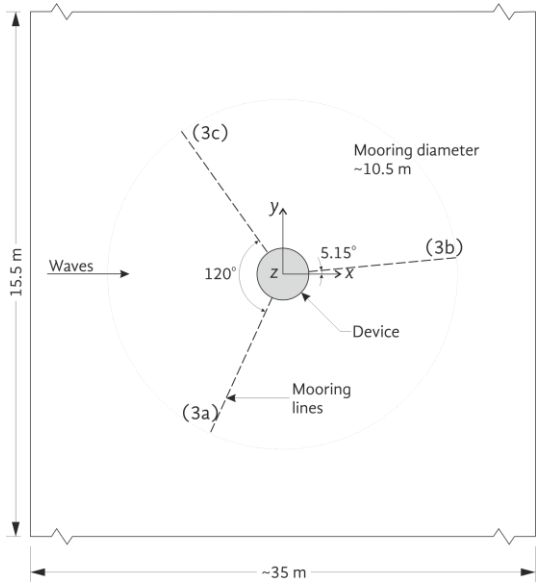

TABLE 8-1 PROPERTIES OF THE CONSTRUCTED MOORING LINES FOR THE ISOLATED SPAR BUOY CONFIGURATION

Line	Chain [m]	Fairlead to clump [m]	Total Dyneema [m]	Total line length [m]	Clump [kg]	Floats [g]
Target values	***1.155***	***1.289***	***5.012***	***6.167***	***1.807***	***6.5***
3A	1.126	1.256	4.955	6.081	1.806	6.5
3B	1.173	1.285	4.965	6.138	1.808	6.5
3C	1.173	1.310	4.980	6.153	1.807	6.5

LINE LENGTHS GIVEN UNASSEMBLED.
FLOATS WERE MEASURED BEFORE ASSEMBLY BUT THEIR INDIVIDUAL MEASUREMENTS WERE NOT RECORDED, ONCE ASSEMBLED MEASUREMENT NOT FEASIBLE SO TARGET VALUES ARE GIVEN.

Line	Force sensor number
3A	1.126
3B	1.173
3C	1.173

TABLE 8-2 PROPERTIES OF THE MOORING LINES FOR CONFIGURATION A

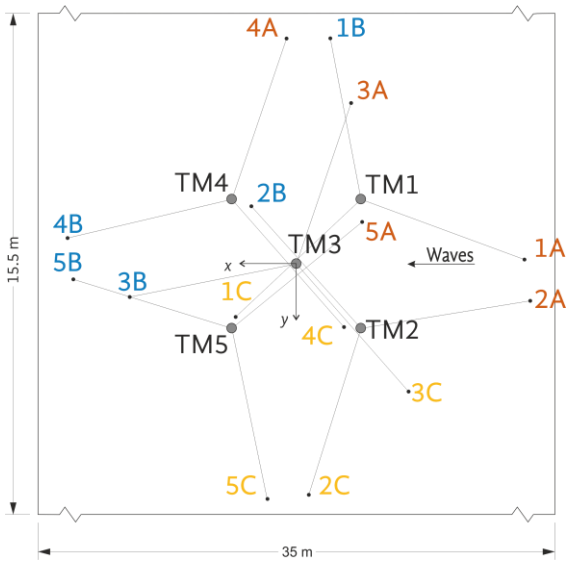

Line	Chain [m]	Fairlead to clump [m]	Total Dyneema [m]	Clump [kg]	Total line length [m]	Floats [g]	Force sensor
Target values	1.155	1.289	5.012	1.807	6.167	6.5	
1A	1.173	1.321	4.972	1.807	6.145	6.5	
1B	1.173	1.285	4.905	1.808	6.078	6.5	
1C	1.173	1.285	4.93	1.807	6.103	6.5	
2A	1.173	1.299	4.991	1.809	6.164	6.5	312
2B	1.173	1.270	4.915	1.807	6.088	6.5	313
2C	1.173	1.265	4.925	1.809	6.098	6.5	314
3A	1.126	1.256	4.955	1.806	6.081	6.5	315
3B	1.173	1.285	4.965	1.808	6.138	6.5	316
3C	1.173	1.310	4.980	1.807	6.153	6.5	317
4A	1.173	1.283	4.910	1.807	6.083	6.5	532
4B	1.173	1.265	4.965	1.800	6.138	6.5	534
4C	1.173	1.300	4.930	1.807	6.103	6.5	533
5A	1.173	1.264	4.930	1.807	6.103	6.5	
5B	1.173	1.270	4.905	1.806	6.078	6.5	
5C	1.173	1.285	4.930	1.806	6.103	6.5	

LINE LENGTHS GIVEN UNASSEMBLED
FLOATS WERE MEASURED BEFORE ASSEMBLY BUT THEIR INDIVIDUAL MEASUREMENTS WERE NOT RECORDED, ONCE ASSEMBLED MEASUREMENT NOT FEASIBLE SO TARGET VALUES ARE GIVEN.
Chain type: 4 mm short link

TABLE 8-3 PROPERTIES OF THE MOORING LINES FOR CONFIGURATION B

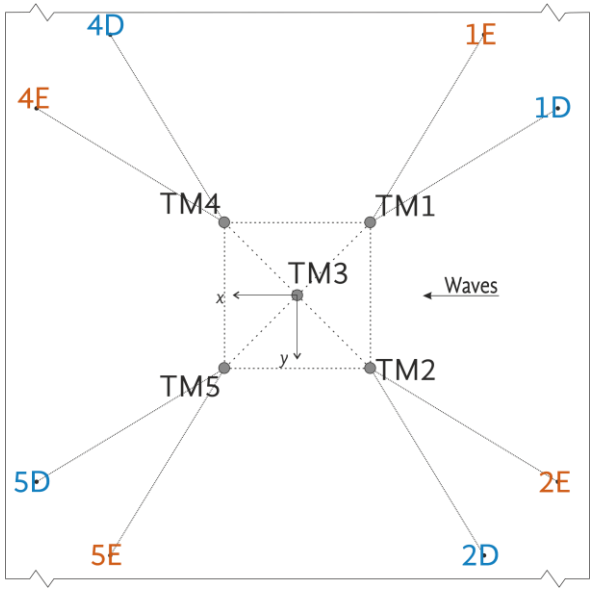

Bottom lines	Chain [m]	Fairlead to clump [m]	Total Dyneema	Clump [kg]	Total line length	Floats [g]	Force sensor
Target values	1.930	2.379	4.627	0.310	6.557	27.2	
1D	1.94	2.445	4.732	0.326	6.672	27.2	
1E	1.93	2.38	4.660	0.337	6.590	27.2	316
2D	1.94	2.403	4.668	0.337	6.608	27.2	
2E	1.941	2.45	4.865	0.334	6.806	27.2	312
4D	1.94	2.372	4.637	0.324	6.577	27.2	
4E	1.94	2.37	4.647	0.325	6.587	27.2	534
5D	1.93	2.4	4.673	0.325	6.603	27.2	
5E	1.939	2.35	4.598	0.327	6.537	27.2	
				Square lines			
Target values	--	--	3.789	0.163			--
1-4	--	--	3.832	0.168		--	315
4-5	--	--	3.970	0.169		--	533
5-2	--	--	3.830	0.169		--	314
2-1	--	--	3.799	0.169		--	313
				Diagonal lines			
Target values	--	--	2.628	0.389			--
1-3	--	--	2.699	0.385		--	
2-3	--	--	2.615	0.384		--	317
4-3	--	--	2.689	0.384		--	532
5-3	--	--	2.650	0.384		--	

SOURCE: LOGBOOK 2 PG 127, 153; LINE LENGTHS GIVEN UNASSEMBLED
FLOATS WERE MEASURED BEFORE ASSEMBLY BUT THEIR INDIVIDUAL MEASUREMENTS WERE NOT RECORDED, ONCE ASSEMBLED MEASUREMENT NOT FEASIBLE SO TARGET VALUES ARE GIVEN.
Chain type: 6 mm short link

TABLE 8-4 PROPERTIES OF THE MOORING LINES FOR CONFIGURATION C

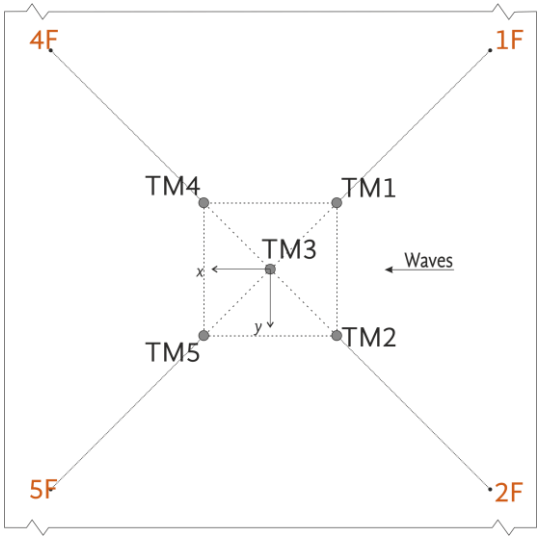

Bottom lines *Target values*	Chain [m]	Fairlead to clump [m]	Total Dyneema [m]	Total line length [m]	Clump [kg]	Floats [g]	Force sensor
	2.679	1.811	4.308	6.987	0.796	44.1	
1F	2.679	1.800	4.305	6.984	0.796	44.1	316
2F	2.679	1.805	4.305	6.984	0.796	44.1	312
4F	2.679	1.802	4.300	6.979	0.795	44.1	534
5F	2.679	1.810	4.308	0.794	6.987	44.1	
			Squares				
		--	3.791		0.169		
1—4	--	--	3.832	--	0.168	--	315
4—5	--	--	3.970	--	0.169	--	533
5—2	--	--	3.830	--	0.169	--	314
2—1	--	--	3.799	--	0.169	--	313
			Diagonals				
			2.633		0.384		
3—1	--	--	2.699	--	0.385	--	317
3—2	--	--	2.615	--	0.384	--	
3—4	--	--	2.689	--	0.384	--	532
3—5	--	--	2.650	--	0.384	--	

SOURCE: (LOGBOOK PG 152 -), LINE LENGTHS GIVEN UNASSEMBLED
FLOATS WERE MEASURED BEFORE ASSEMBLY BUT THEIR INDIVIDUAL MEASUREMENTS WERE NOT RECORDED, ONCE ASSEMBLED MEASUREMENT NOT FEASIBLE SO TARGET VALUES ARE GIVEN.
Chain type: 6 mm short link

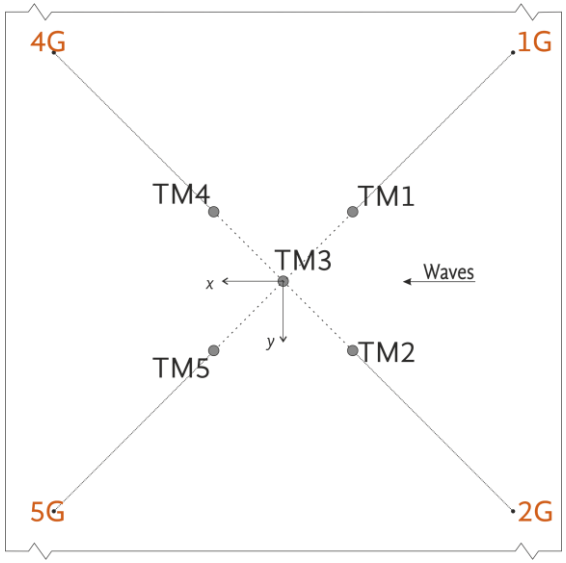

TABLE 8-5 PROPERTIES OF THE MOORING LINES FOR CONFIGURATION D

Bottom lines	Chain [m]	Fairlead to clump [m]	Total Dyneema [m]	Total line length [m]	Clump [kg]	Floats [g]	Force sensor
Target values	***3.399***	***2.127***	***3.589***	***6.988***	***0.533***	***53.1***	
1G	3.406	2.130	3.570	6.976	0.533	53.1	315
2G	3.408	2.136	3.578	6.986	0.528	53.1	312
4G	3.408	2.122	3.532	6.940	0.532	53.1	534
5G	3.400	2.128	3.560	6.960	0.534	53.1	
			Diagonals				
Target values			2.668		0.797		
3—1	--	--	2.699	--	0.796	--	
3—2	--	--	2.615	--	0.796	--	314, 317
3—4	--	--	2.689	--	0.795	--	532
3—5	--	--	2.650	--	0.794	--	313

LINE LENGTHS GIVEN UNASSEMBLED
FLOATS WERE MEASURED BEFORE ASSEMBLY BUT THEIR INDIVIDUAL MEASUREMENTS WERE NOT RECORDED, ONCE ASSEMBLED MEASUREMENT NOT FEASIBLE SO TARGET VALUES ARE GIVEN.
Chain type: 6 mm short link

9 Materials, methods and analysis details

9.1 Instrumentation

Data were collected from four different instruments: wave gauges, pressure sensors, load cells and from the 6 dof tracking system, along with four digital video cameras positioned both above and below the water. For most of the experimental campaign, data acquisition was synchronised between the various systems. Table 9-1 gives details of the data acquisition for the various systems. Examples of file headers are given in the Appendix.

TABLE 9-1 DETAILS OF INSTRUMENTATION AND DATA ACQUISITION

	Waves	Pressure	Load	Motions
Software	Edinburgh Designs Ltd.	Labview (bespoke)	Labview (bespoke)	Qualisys QTM v2.7
Hardware	Twin wire resistance wave gauges, Edinburgh Designs Ltd DAQ	Honeywell HSCSAAN010NDAA5 NI compact DAQ9191 Chassis	Futek LSB120 miniature s-bean load cell NI compact DAQ9191 Chassis	Qualisys
Start	Triggered by wave makers	Triggered by wave makers	Triggered by wave makers	Triggered by wave makers
Stop	Triggered 30 s after wave makers end	Automatic (manual for some spar buoy experiments)		
F_s [Hz]	128	1667	1667	128
Files	.txt	.lvm		.qtm and .tsv

The load cells were calibrated by the supply company (FUTEK) and each had a calibration certificate supplied. Details on linearity are given in the Appendix.

Uncertainties on the other instruments are as follows:

- Wave gauges: daily calibration of wave gauges gave error typically <0.0095 m
- Pressure sensor total error band: ±1% of full scale span (see data sheet for details)
- Qualisys positions: Residuals for markers are defined as the difference between the average error measured (mm) compared to the (initial) 6dof body definition and these are given in the output (.tsv) files

An uncertainty analysis on the measurements is described in Section 9.3.7.

9.2 Set up of experiments

9.2.1 Waves

Regular waves were run at two different wave heights: $H = 0.05$ m and $H = 0.10$ m, at frequencies between $f = 0.3$ Hz and $f = 1.0$ Hz for 3 minutes (180 s).

For each experimental set-up, the wave gauges were positioned around the basin as shown in Figure 9-1, with the precise positions given in the Appendix.

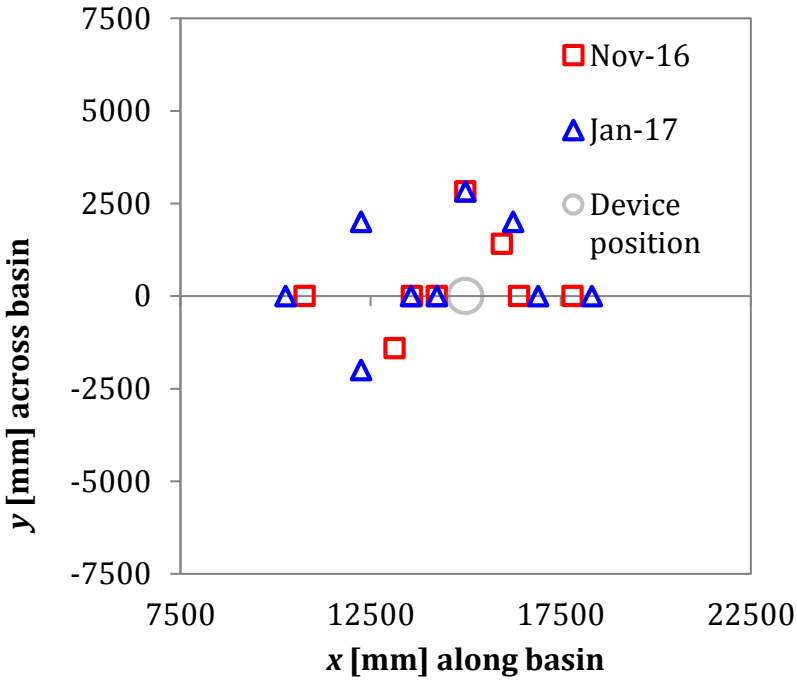

FIGURE 9-1 WAVE GAUGE POSITIONS FOR ALL SPAR BUOY EXPERIMENTS

In the case of the rigid coaxial devices, twin-wire wave gauges were built into the models to measure the internal wave surface elevation and hence the power captured by the devices. The same software was used to record from the model gauges but the gauges could not be calibrated in the same way. Instead, the gauges were manually calibrated at the beginning of each day (every other day for the isolated device experiments). A synthetic line was attached to the bottom of the model that ran through a pulley on the basin floor and up to an instrumentation gantry. Using this line, the model was submerged by a small amount. Readings were taken from the wave gauges and from the 6dof tracking system so that the submergence amount could be calculated. This process was continued until the top of the device was near the water surface. Details of this process are given in Appendix 9.2.5.

9.2.2 Pressures

In order to calculate the device power output and the pressure and flow rate through the OWC are required. The pressure in the cylinder was measured using a Honeywell HSC analogue differential sensor. A heavy-duty industrial sensor was attached to a device which was manually pushed in the water to assess the maximum and minimum expected pressures in the column. This was then used to select the Honeywell HSC sensor with a working pressure of ±2.5 KPa and an accuracy of 0.25% of the full-scale output. The sensor is a lightweight board mounted device. A housing was 3D printed to hold the sensor in place with the input port entering the internal pressure ring. The sensors were pre-calibrated by the manufacturer and came with the appropriate documentation. The analysis procedure for the power calculations are given in Section 9.3.3. The signal was acquired through a NIDAQ. As one chassis was used for both the line tension and pressure signals, the minimum sampling frequency of both sensors had to be used for both sensors. In this case the load cell frequency

was used of 1667 Hz. A timing trigger from the wave paddles was used to being data capture in order to align the beginning of all sensor outputs.

For the rigid device arrays, the sensors were mounted in a small housing with a small flexible tube leading into the device plenum.

9.2.3 Loads

The line loads were estimated from preliminary predictions from a numerical model using OrcaFlex. Knowledge of expected line tensions from previous array tests was also drawn upon to select an appropriate load cell. The LSB-210 Futek analogue submersible junior s-beam load cell was selected. The sensor has a range of ±445 N and a non-linearity of 0.2% and was deemed suitable for the proposed experimental plan. As with the pressure transducers, these load cells were pre-calibrated by the manufacturer and were provided with all the necessary certification. The signal was acquired at the minimum sampling frequency of 1667 Hz through a National Instruments data acquisition chassis and recorded using a custom LabVIEW data acquisition program. Again, a timing trigger from the wave paddles was used to initiate the recording.

Nine load cells were used and positions were chosen to maximize the information about each configuration. As there were not enough load cells for every line within the array, symmetry about the longitudinal centreline of the array was assumed for configuration C and D.

9.2.4 Motions

Reflective markers were fitted to the models on a small wand on the top of the orifice plate. In total five markers were fixed to each device in a unique layout in order to differentiate between each. A global origin was set up using a quadrangle in the centre of the basin. This origin defines the surge (x), sway (y) and heave (z) axis as well as the rotations about each respective axis as roll, pitch, and yaw. Each device was defined as a rigid body during calibration and the origin of the local co-ordinate system was translated to the centre of gravity of the device. All motions were recorded relative to the global system. Qualisys Track Manager© was used to track the markers for each wave run. The system comprised of five infrared cameras set up around the basin and a central laptop to run the acquisition software.

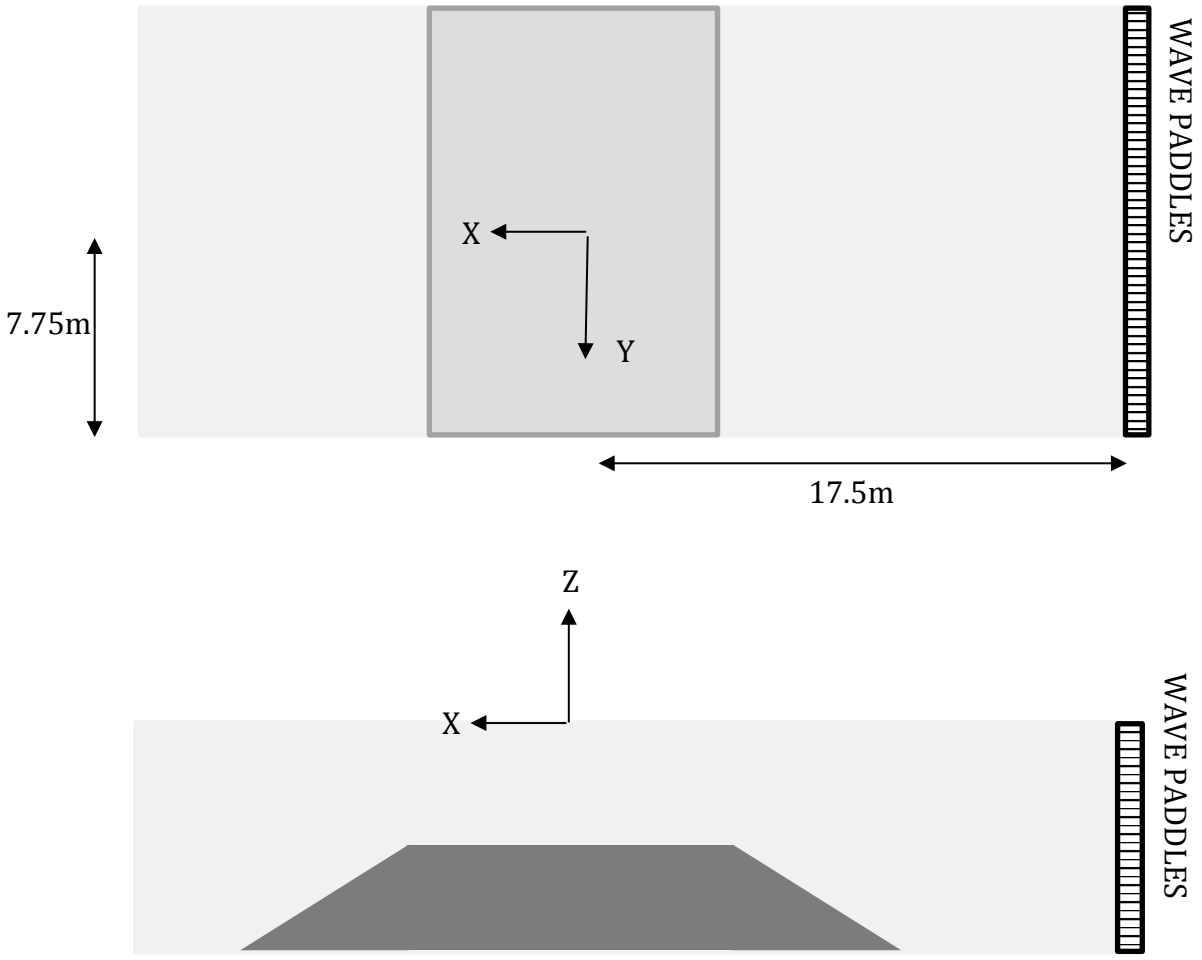

FIGURE 9-2 QUALISYS GLOBAL ORIGIN DEFINITION.

A sampling frequency of 128 Hz was used to match that of the wave probes and a timing trigger line from the wave paddles was used to initiate recording.

9.2.5 Calibration of internal wave gauges (rigid devices)

The device (isolated or array) was manually displaced in the heave direction by pulling on a line that ran through a pulley mounted to the floor of the basin and then attached to the bottom of the device. The voltage readings from the wave gauges and the position of the device as tracked by the 6 dof motion tracking system were recorded continuously during each test. For each calibration test, the device was displaced by progressively greater amounts, held in that position for a couple of seconds, until the device was almost totally submerged.

Constants related to each model were added to the positon data to express the data as the distance between the water line and the orifice plate, *Dwo*. A linear fit was applied to the

position and voltage data, *wgv*. From this the calibration coefficients, $c1$ and $c2$, were derived for each internal wave gauge where:

$$Dwo = c1 \times wgv + c2$$

An example of the coefficients is shown in Table 9-2 for the first calibration of the array.

TABLE 9-2 EXAMPLE CALIBRATION COEFFICIENTS FOR THE ARRAY

Date	**Gauge//Device**				
2017/10/09, 11:48:00	1	2	3	4	5
c1	0.7892	0.7427	0.7881	0.8033	0.8127
c2	-0.2534	-0.2530	-0.2520	-0.2523	-0.2514

9.3 Analysis Methods

Data recorded during the experiments was collated, filtered and calibration coefficients applied where necessary. In most cases, the mean offsets from static positions were removed so that all oscillations were about zero and results were relative to static equilibrium.

The capture width ratio was calculated by calculating the quotient of the absorbed power and the incident power per metre of wave crest and normalising by the device width. The value is an indication of the device efficiency as a function of the device width, allowing different devices to be compared to one another.

9.3.1 Wave climate

Regular wave experiments were analysed using a zero down-crossing method and a frequency domain spectral method was used to analyse the irregular sea-states. For the spar buoy experiments, the wave data were windowed based on the number of waves generated; the window ran from wave number 50 to wave number 75 to allow the basin to enter a steady state. This window was also used for the analysis of the pressure, mooring line tensions and motions. For the rigid devices, the regular wave experiment time was fixed at 180 s and the final 67 s were used as the data analysis window.

For the operational irregular sea states, the experiment time was fixed at 690 s and a 600 s-long window was chosen, equivalent to just over an hour at full-scale. The extreme sea state experiments ran for 1908 s and a window of 1708 s was chosen for the analysis: three hours at full scale.

This means that the time series loops back to the beginning of the run after 10 minutes, meaning that a window of 10 minutes can be selected anywhere in the time series and the full energy within the spectrum will be incorporated.

9.3.2 Power from pressure sensors

Owing to the difficulty with mounting an internal wave gauge in the spar buoy device, a pressure sensor was used to calculate the power absorbed by the devices. The orifices of the

five devices were calibrated determine the discharge coefficient, C_D. The calibrated value of C_D was 0.69 with values for the five plates within 1% of each other.

The pressure data was windowed to match the incident wave window and filtered with a low-pass digital filter to remove electrical noise and interference. The data was zeroed by removing the mean of the first half a second to ensure the pressure oscillates about the initial zero pressure difference and to account for any ambient changes. Flow rates were calculated using the incompressible flow model with discharge coefficients of alternating sign depending on the sign of the pressure. The power generated by the water surface motion, P, is the product of the volumetric flow rate, Q, and the pressure drop, Δp:

$$P = \Delta pQ = \Delta pA_o C_D \sqrt{\frac{2\Delta p}{\rho_{air}}} \quad \textbf{9-1}$$

where A_o is the area of the orifice and ρ_{air} is the density of the air, taken as 1.225 kg/m^3. The time average was calculated across the window to give an average power for each test performed.

The efficiency of the arrays was calculated in the form of a capture width ratio, Eqn 9-2. This is the ratio of the array power output, P, to the incident wave resource, P_{in}, normalised by the device maximum width, D. For both the rigid and the flexible arrays, the capture width ratio was found for each device in the array and summed to give a total for the whole array.

$$CWR = \frac{P}{P_{in}D} \quad \textbf{9-2}$$

9.3.3 Power from surface elevation

For the rigid coaxial devices, a wave gauge was installed inside the chamber. Using the internal wave gauge to record the surface elevation of the water in the chamber, the power, P, associated with the water movement is given by:

$$P = \Delta pA_c v = \Delta pA_c \frac{ds}{dt} \quad \textbf{9-3}$$

where Δp is the chamber gauge pressure, A_c is the cross-sectional area of the chamber and v is the velocity of water surface oscillation. The velocity of the water was found by calculating the derivative with respect to time of the position of the water surface, S.

9.3.4 Linearized Power Prediction – Irregular sea states

In order to contextualise the regular capture width curves, a linearized approach was used to approximate the potential annual energy extraction of each configuration at the target site. The spectral incident wave power of each sea state was multiplied by the frequency-dependent capture width to predict an array power output. This was summed across all sea states and multiplied by hours at each state to predict an energy extraction.

Incident wave spectra corresponding to the probability matrix are first transposed to amplitude spectra, in order to calculate an incident wave power at each discrete frequency.

The spectral energy density (S) is transposed to an amplitude spectrum (S_a) as follows, where Δf is the discretisation of the frequency space.

$$S_{a\,i,m} = \sqrt{2S_{i,m}\Delta f}$$

The energy of each frequency component (S_E) is then calculated in accordance with linear wave theory. The total energy per unit area (E) for each spectrum has been calculated by summing S_E over all frequencies, where N is the number of frequency components. As the amplitude spectrum is a function of the differential frequency component, halving the frequency bin size does not double the sum.

$$S_{E\,i,m} = \frac{\rho g(2 * S_{a\,i,m})^2}{8}$$

$$E_{i,m} = \sum_{f=0}^{N} S_{E\,i,m}$$

The incident wave power spectrum (S_P) as a function of frequency has been calculated by multiplying the energy spectrum by the group celerity (C_g) of each frequency component. This adds the time component and frequency dependency of the power. Again, the total power (P) per unit wave crest of the sea state is calculated from the sum of each power component.

$$S_{P\,i,m} = S_{E\,i,m}C_g(f)$$

$$P_{i,m} = \sum_{f=0}^{f=N} S_{P\,i,m}$$

The total seastate energy per unit area available per annum has then been calculated by multiplying the power matrix by the number of hours at each sea state from the probability matrix. Summing over all rows and columns of the energy matrix results in a total energy available (E_{Net}) over all sea states for the year.

$$P_{i,m} = \begin{pmatrix} P_{1,1} & \cdots & P_{1,j} \\ \vdots & \ddots & \vdots \\ P_{i,1} & \cdots & P_{i,m} \end{pmatrix}$$

$$Hrs_{i,m} = \begin{pmatrix} Hr_{1,1} & \cdots & Hr_{1,j} \\ \vdots & \ddots & \vdots \\ Hr_{i,1} & \cdots & Hr_{i,m} \end{pmatrix}$$

$$E_{Net} = \sum_{i=1}^{N}\sum_{m=1}^{n} P_{i,m} * Hrs_{i,m}$$

The capture width curves from regular experimental data were scaled up by multiplying the frequency axis by the Froude scaling factor of $40^{-0.5}$. In order to match the number of frequency components of the capture width curve and the incident wave power spectrum a linear interpolation between experimental data points has been made. The full-scale capture width curve has then been multiplied by the incident wave power spectrum to obtain a frequency dependent array power output for the specific sea state. This multiplication has been then repeated for all possible sea states within the probability matrix for all four configurations. Similar to the calculation of total power for a sea state, the total array power is then calculated as the sum of all power components across all frequencies, resulting in a power matrix for each configuration (P_A). This matrix is then multiplied by the hours matrix to calculate the total extracted energy for each sea state (E_{AExt}).

$$P_{A\,i,m} = \sum_{N=1}^{N} S_{P\,i,m} * CW_A$$

$$E_{A_{Ext}\,i,m} = P_{Ai,m} * Hrs_{i,m}$$

Where CW_A is the capture width curve from regular wave tests for configuration A and $P_{A\,I,m}$ is the scalar average power from configuration A for sea state i,m. The total efficiency of each array configuration is then the ratio of extracted energy (E_{out}) to the available incident energy (E_{in}).

$$\epsilon = \frac{E_{out}}{E_{in}} = \frac{\sum_{i=1}^{i=N}\sum_{m=1}^{m=n} E_{A_{Ext}\,i,m}}{E_{Net}}$$

The measured annual power output was the sum of the energy extracted at all possible sea states divided by the time from the probability matrix. The values per Configuration are reported in Table 9-3 as a fraction of the power as calculated from the irregular wave experiments.

TABLE 9-3 RATIOS OF PREDICTED (P_P) TO MEASURED (P_E) POWER OUTPUTS FOR IRREGULAR SEA STATES OF CONSTANT H_S = 0.05625 M

Tp [s]	Configuration A	Configuration B	Configuration C	Configuration D
1.20	1.12	0.98	0.99	0.99
1.57	0.92	0.97	1.02	1.00
1.93	0.95	0.99	1.03	1.04

As stated, this methodology assumes linearity. In order to check these assumptions, the method is used to predict the irregular sea states that were tested in the basin to make a direct comparison of predicted to measured values.

It can be seen from Table 9-3 that the linear approximation method makes a reasonable prediction of the irregular power outputs. Configuration A shows the most divergence, with the model over predicting the case of T_p = 1.20 s by circa 12% and under predicting the

T_p = 1.57 s and T_p = 1.93 s by 5~8%. This error may come from areas of the CWR curve that have not been tested in regular waves and therefore are neglected in the linear interpolation when the CWR curves were matched to the sea state frequency discretisation. Another source could be from differences in responses due to the presence of amplitudes at infinite frequencies responding differently to single frequency incident waves.

9.3.5 Mooring loads

The mooring line tension data was filtered in a similar manner to the pressure and position data with a median and fifth order Butterworth filter. Data was windowed to match with the windowed wave data before both time and frequency domain analysis.

When the cyclic characteristic of the tension is presented in the report, the pre-tension was subtracted and the root mean square (rms) of the time series was calculated. This rms value was divided by the rms value of the windowed wave time series to give a tension response per unit wave height.

Irregular sea state loads are also presented as amplitude spectra by using a discrete Fourier transform of the data.

9.3.6 Motion analysis

Qualisys Track Manager was used to capture the motion responses. These responses were separated into six degrees of freedom for each rigid body: one for each of the spar buoys and one for each of the rigid isolated and rigid array devices. The initial position was subtracted from the output in order to assess the motion responses relative to the initial position. For the regular wave cases, a response amplitude operator (RAO) was calculated using a time-domain method. The zero crossing points were located and the maximum and minimum points were found. The average peak and trough were used to calculate an average response for the given (i^{th}) degree of freedom (H_i). This response was then normalized by the incident wave height (H_w) to give the RAO:

$$RAO = \frac{H_i}{H_w}$$

The incident wave height was calculated from the empty basin tests. By doing this, the assumption is made that reflections from basin side-walls and beach remain constant for all incident wave fields. Thus the power produced by each array will be the result of the configuration changes, which in turn will have an effect on the localised wave field.

For the irregular cases the window corresponding to the repeat time is again selected and the rms of the output calculated (σ_i). This is then normalized by the rms of the incident wave time series (σ_w).

$$RAO = \frac{\sigma_i}{\sigma_w}$$

9.3.7 Uncertainty analysis

A sensitivity analysis of all the components contributing to the capture width calculation was performed and this was used to determine the largest sources of error and the error associated with the capture width calculation as shown in the example in Table 9-4.

TABLE 9-4 SENSITIVITY ANALYSIS ON UNCERTAINTY IN CAPTURE WIDTH CALCULATIONS

Variable	Nominal	Tolerance	Source	% Coefficient	$\frac{\Delta CW}{CW}$	ΔCW	%
p	95	±6.25 Pa	Datasheet	0.066	0.099	0.010	9.81
H	0.0343	±0.002 m	Figure 9-4 (Appendix)	0.058	0.105	0.011	10.78
CW	0.102	0.015 m	Root square sum	-	0.144	0.015	14.58

The sensitivity analysis in Table 9-4 shows the pressure transducer to be suitably matched to the capability of the repeatability of the wave conditions, as indicated by the percentage errors in the right-hand column. The analysis further shows the uncertainty in the capture width calculations using the specified instrumentation to be nearly 15% and the results will be discussed in light of this. While the error on the capture width measurements will increase as the pressures get smaller, the experiments at frequencies of interest were repeated up to three times.

To assess the experimental resolution an uncertainty analysis of the measured variables can be used to indicate the magnitude of the errors in the results. The capture width was initially calculated from the measured variables of incident wave height and internal chamber pressure. For the purposes of this example, the uncertainty in the incident wavelength and the orifice calibration coefficient is assumed to be negligible compared to that of the pressures and wave heights. Thus, the values of the group celerity, c_g and the calibration coefficient are absolute.

The flow rate, device output power, P_{out} and incident wave power, P_{in} are calculated as follows, where the ±Δ values show the measurement uncertainties:

$$Q = AC_d\sqrt{\frac{2p(\pm\Delta p)}{\rho_{air}}}$$

$$P_{out} = \frac{p^{\frac{3}{2}}(\pm\Delta p)AC_d\sqrt{2}}{\sqrt{\rho_{air}}}$$

$$P_{in} = \frac{\rho_{water}gH(\pm\Delta H)^2c_g}{8}$$

where ρ_{water} is the water density (taken to be 1000 kg/m^3), g is the acceleration due to gravity, taken to be 9.81 m/s^2 and H is the wave height. The uncertainty in the pressure measurement was obtained from the manufacturer's datasheet and was equal to ±6.25 Pa.

When calculating the time-averaged output power there will be an uncertainty in the measurement proportional to the uncertainty in the pressure measurements. In accordance with [17] the uncertainty for a given function is defined as:

$$\Delta y(x,z,b) = \sqrt{\left(\frac{\partial y}{\partial x}\Delta x\right)^2 + \left(\frac{\partial y}{\partial z}\Delta z\right)^2 + \left(\frac{\partial y}{\partial b}\Delta b\right)^2}$$

A relative error can be calculated by dividing both sides by the original function. If it is assumed that the main source of the uncertainty in the power calculation comes from the pressure measurement the equation simplifies to:

$$\frac{\Delta P_{out}}{P_{out}} = \sqrt{\left(\frac{\frac{\partial P_{out}}{\partial p}\Delta p}{P_{out}}\right)^2} = \frac{1.5\cancel{p^{0.5}AC_d\sqrt{2}\rho_A^{-0.5}}\Delta p}{\cancel{p^{3/2}AC_d\sqrt{2}\rho_A^{-0.5}}} = \frac{1.5\Delta p}{p}$$

This gives a relative error on every power measurement. The mean power output is then calculated:

$$\bar{P}_{out} = \frac{\sum_{t=1}^{N} P_{out\,t}}{N}$$

The absolute errors associated with each power output calculation are added in quadrature to give a total relative error on the average power output.

$$\Delta\bar{P}_{out} = \sqrt{\sum_{t=1}^{N}\left(\frac{\partial\bar{P}_{out}}{\partial P_t}\Delta P_t\right)^2} = \sqrt{\sum_{t=1}^{N}\left(\frac{\Delta P_t}{N}\right)^2}$$

Again, the relative error is obtained through dividing both sides by the original function.

$$\frac{\Delta\bar{P}_{out}}{\bar{P}_{out}} = \sqrt{\sum_{t=1}^{N}\left(\frac{\Delta P_t}{\sum P_{out}}\right)^2}$$

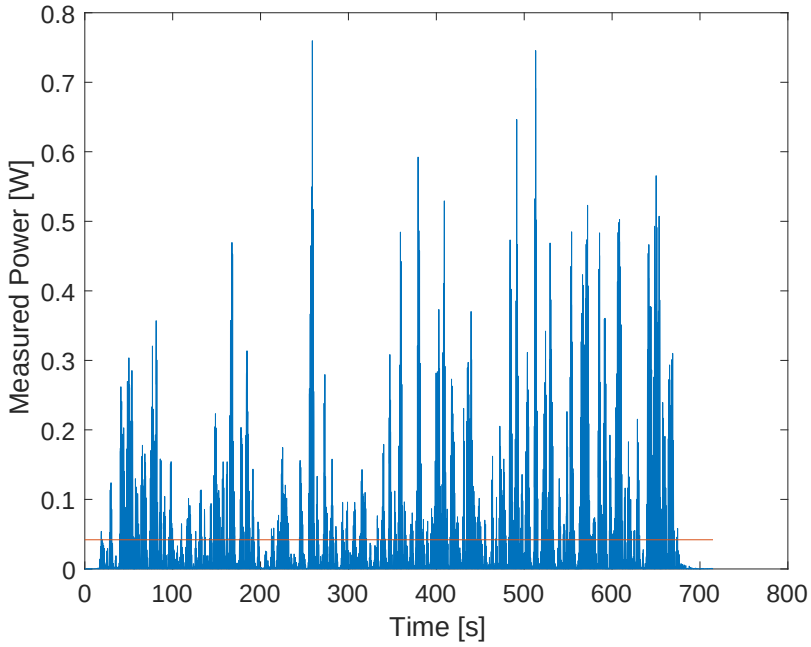

FIGURE 9-3 TIME SERIES OF TM3 DEVICE POWER OUTPUT WITH THE AVERAGE OVER TIME.

For irregular cases the *q factor* has been used to demonstrate the efficiency of the devices in the interconnected cases with respect to an isolated case. In this case the sum of the array power is normalized by the power output of a singular device multiplied by the number of devices in within the array (*N*).

$$q = \frac{\sum_{i=1}^{N} \bar{P}_{out\,i}(\pm\Delta\bar{P}_{out\,i})}{N * \bar{P}_0(\pm\Delta\bar{P}_0)}$$

The error calculated for the average power output from each device can be carried forward into the error calculation for the *q factor*. Therefore, the uncertainties are again added in quadrature.

$$\Delta q = \sqrt{\sum_{i=1}^{N}\left(\frac{\Delta P_i}{N\bar{P}_0}\right)^2 + \left(\frac{\sum \bar{P}_{out\,i}\Delta\bar{P}_0}{N{\bar{P}_0}^2}\right)^2}$$

The average power output shown in Figure 9-3 has an error band on the red line. As it is barely noticeable, it becomes obvious that the error on the average power output is very small.

A similar analysis can be carried out on the incident wave power. For this case, the error is associated with the measurements of the wave height. From running repeats of the same regular sea conditions one can ascertain the repeatability of the incident wave conditions. Figure 9-4 shows a plot of mean wave height values across three repeats carried out at a

frequency of 0.63 Hz and intended amplitude of 0.025 m. The error bars indicate the 95% confidence interval (assuming the deviation from the intended height to be normally distributed). In the worst-case scenario seen at Probe 8 the 95% interval equates to a repeatability value of H±0.0026 m. This frequency displayed the highest levels of variation due to the excitation of a cross wave due to the harmonics of the basin width. This being the case, this value of error is considered the worst case possible across the frequency space of testing.

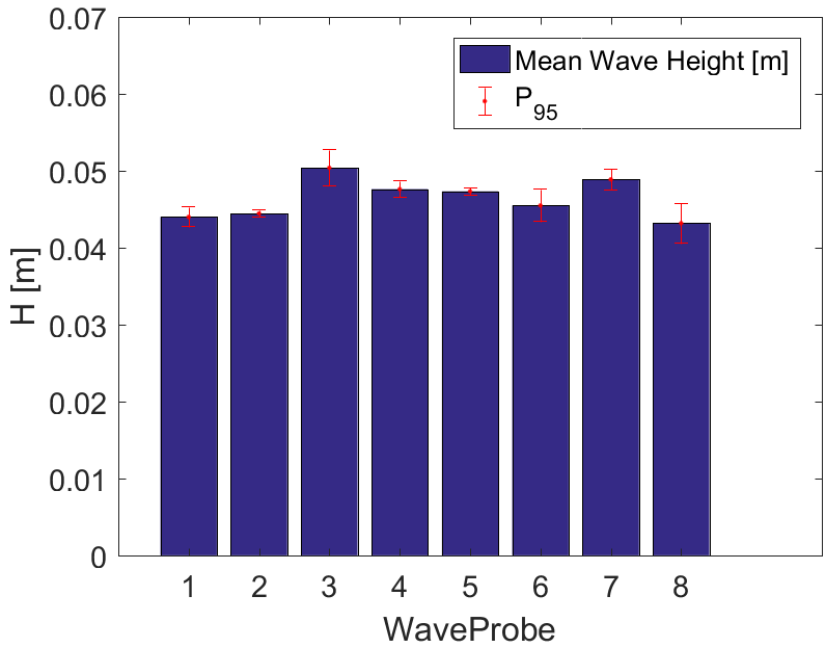

FIGURE 9-4 REPEATABILITY OF REGULAR WAVE CONDITIONS IN PLYMOUTH UNIVERSITY OCEAN BASIN.

The incident wave power is required for calculating the capture widths of the arrays in order to assess the efficiency of each. By differentiating the theoretical incident wave power the propagated uncertainty on the power can be predicted.

$$\Delta P_{in} = \sqrt{\frac{\partial P_{in}}{\partial \mathrm{H}} \Delta \mathrm{H}} = \sqrt{\frac{\rho g \mathrm{H} C_g}{4} \Delta \mathrm{H}}$$

and the relative error on the incident wave power

$$\frac{\Delta P_{in}}{P_{in}} = \frac{2}{H} \Delta \mathrm{H}$$

9.3.8 Data filtering

To remove noise and smooth the data several filtering techniques were employed. Initially a median filter was used to remove spikes, followed by a low pass, fifth order Butterworth filter.

The pressure data that had been recorded as a raw voltage output. This was translated to Pascals using the transfer function from the data sheet.

$$\frac{(P_{max} - P_{min})(V_o - 0.1V_s)}{0.8V_s} + P_{min} = P_A$$

Where P_{max}, P_{min} and P_A refer to the maximum, minimum working pressures of the sensor and the applied pressure respectively. In this case, the working pressures are ±2.5 KPa. V_s and V_o are the supply (five volt) and output voltages.

10 Additional results

10.1 Natural periods

10.1.1 Rigid devices

For each degree of freedom chosen, the device was displaced along the axis of the degree of freedom, released and allowed to come to rest. For the surge and heave motions, the device was pulled along the axis of the degree of freedom by a line attached to the side or to the base of the model, data recording commenced, and the model was released and allowed to come to rest. For the rotations, data recording was started and then the device was manually displaced on its top surface by a small amount. A zero-crossing technique was used to calculate the period of oscillation, T_n, over as many cycles as were present in the recording.

10.1.2 Spar buoy devices

In order to determine the natural characteristics of the spar buoy in each configuration, free decay tests of the moored devices were performed. The initial displacement was restricted to each degree of freedom by initiating the movement using a pulley system aligned with the axis of interest. The tests were repeated three times to ensure repeatability of calculation. Load, motion and chamber pressure were all measured during the tests, and the motions were used to calculate the natural period, logarithmic decrement, Λ and damping of the system. The logarithmic decrement was calculated by taking the natural logarithm of the ratio of the amplitude of the first and last peaks and dividing by the number of periods, n in the time series:

$$\Lambda = \ln\left(\frac{z(t)}{z(t + nT)}\right) n^{-1}$$

Where z is the vertical displacement of the device and can be replaced with the direction of the degree of freedom being tested. The total damping of the system, ξ_{tot} is the sum of the structural (ξ_0), radiation (ξ_w) and viscous (ξ_v) damping:

$$\xi_0 + \xi_w + \xi_v = \xi_{tot} = \frac{\Lambda}{T}$$

which is equal to the quotient of the logarithmic decrement and the average time difference between successive peaks in the motion, T.

TABLE 10-1 NATURAL PERIODS, LOGARITHMIC DECREMENT AND TOTAL DAMPING FOR THE ISOLATED SPAR BUOY (TM3) DEVICE WITH A 95% CONFIDENCE INTERVAL

	Natural Period [s]			
DoF	*T* [s]	Tol [±s]	**Λ [-]**	**ξtot [s^{-1}]**
Surge	16.23	0.01	0.29	0.02
Sway	16.02	0.03	0.23	0.01
Heave	1.53	0.02	0.86	0.56
Roll	5.71	0.77		
Pitch	5.57	0.07	0.10	0.02

Figure 10-1 shows that the heave decay tests had high repeatability, and this is shown in the low tolerance value given in Table 3-4. For other modes of motion, it was more difficult to limit motion to only one degree of freedom, resulting in difficulty calculating the natural period and damping properties.

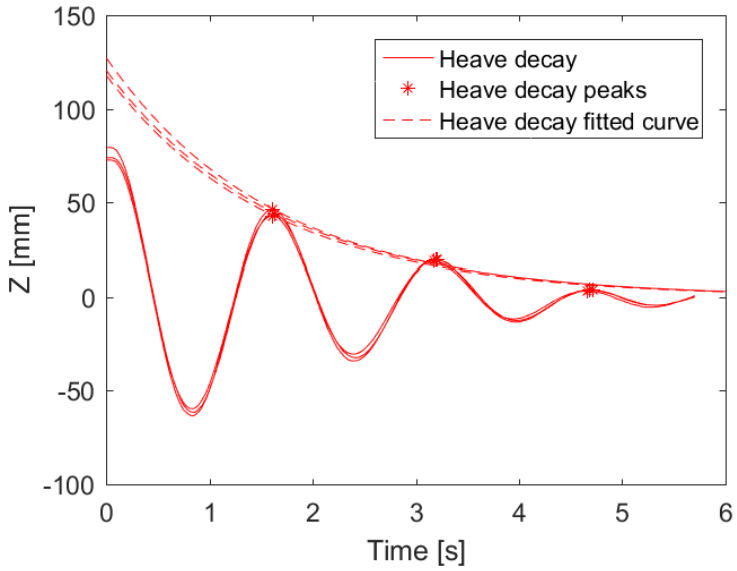

FIGURE 10-1 THREE REPEATS OF HEAVE DECAY TEST RESULTS FOR AN ISOLATED TM3 DEVICE.

TABLE 10-2 DECAY TEST RESULTS FOR ALL CONFIGURATIONS

		Natural Period [s]		Λ [-]		ξ_{tot}	
		TM3	TM2	TM3	TM2	TM3	TM2
Config A	Surge	16.47	15.80	0.32	0.40		0.0194
	Heave	1.58	1.61	0.82	0.79	0.52	0.49
Config B	Surge	23.17	22.02	0.56	0.45	0.02	0.02
	Heave	1.48	1.48	0.73	0.71	0.49	0.48
Config C	Surge	24.84	24.26	n.d	n.d	n.d	n.d
	Heave	1.47	1.46	0.71	0.67	0.48	0.46
Config D	Surge	15.99	Unstable	0.14	n.d	0.01	n.d

	Heave	1.47	1.48	0.71	0.71	0.48	0.48

10.2 Draught and waterline placement for rigid devices

During testing, the isolated device and the array of devices were both seen to change their position in the water. This was caused by water ingress; water entered small gaps within the model walls, which led to the sinking of the models up to the point at which the model was saturated. The assembly of the base unit was changed in light of this, so the change in draught was reduced for the array compared to the isolated device. In both cases, this was mitigated by attaching additional foam to the device: around the base for the isolated device and around the central array supports for the array in order to achieve the desired draught.

For the isolated device, the distance between the CoM and the SWL had a target value of 657 mm [6] and to measure this, the mean of the first 3 s of the 6dof recording were used to determine the value of SWL-CoM. Figure 10-2 shows how this distance varied over two non-consecutive days of testing. The plot on the left of Figure 10-2 represents the last day of testing during the first week during which nine regular wave tests were performed. The device was left in the water over the weekend and the water ingress had caused the device to sink much lower by the start of the next week. The device was removed, allowing the entrapped water to escape and foam was attached to the base of the device. Owing to the difficulty in determining if all the entrapped water had escaped and knowing that over time it would seep back in, the process was fairly crude. The plot on the right-hand side of Figure 10-2 shows the variation in the SWL-CoM distance over the course of 9.5 hours after the foam had been attached to the device.

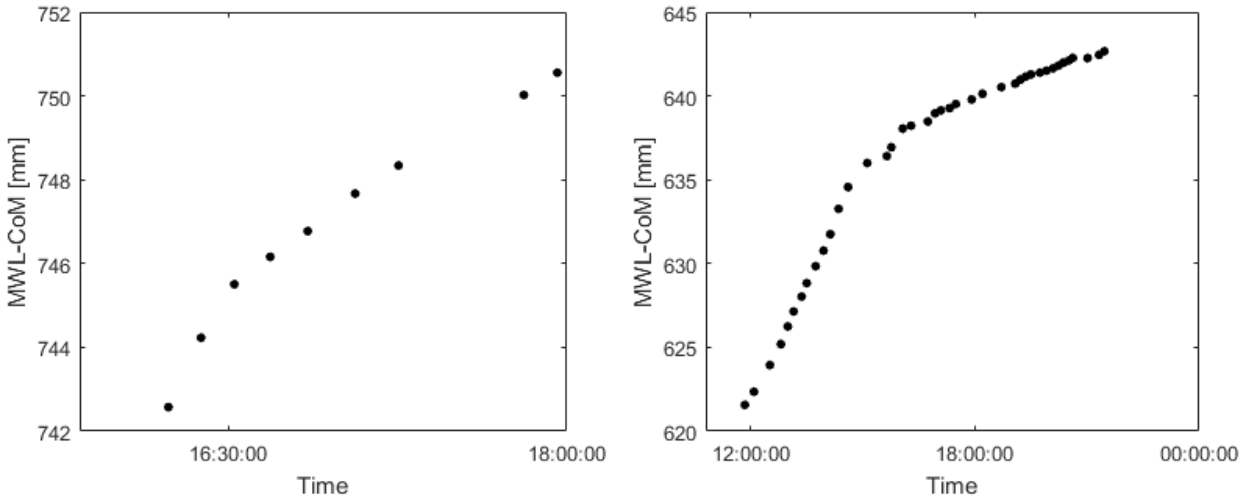

FIGURE 10-2 VARIATION IN THE DISTANCE BETWEEN THE STILL WATER LINE (SWL) AND THE CENTRE OF MASS (COM) FOR THE ISOLATED DEVICE ON TWO NON-CONSECUTIVE DAYS.

Figure 10-3 shows the distance between the still water line and the centre of mass for all experiments after the extra foam had been added to the isolated device and so includes the data in the right hand plot of Figure 10-2 but not those from the left-hand plot. After the first day, the rate of sinking was constant until the first survivability experiments, after which there was an increase in the SWL-CoM value.

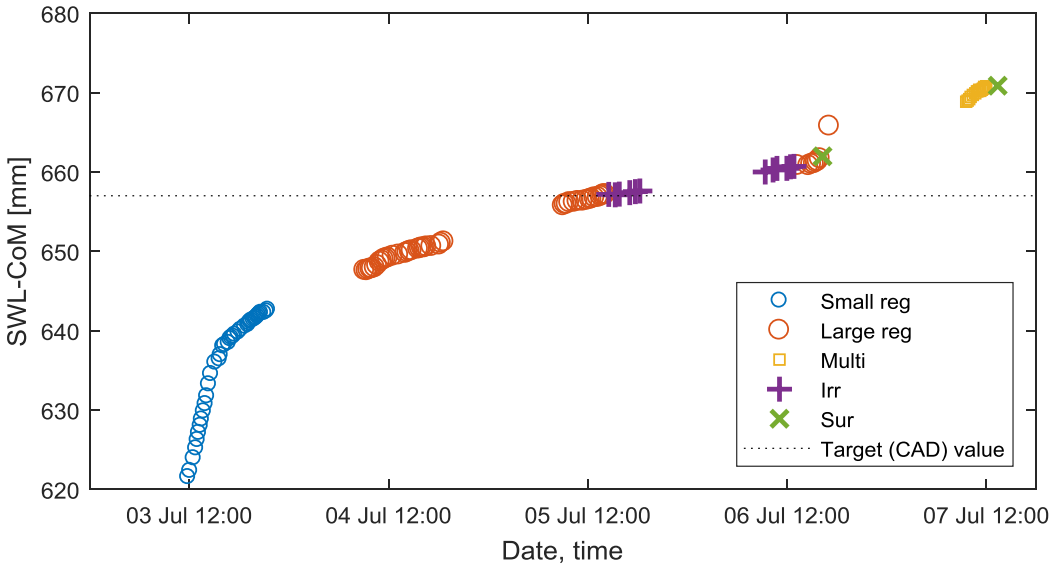

FIGURE 10-3 VARIATION IN THE DISTANCE BETWEEN THE STILL WATER LINE (SWL) AND THE CENTRE OF MASS (COM) ALL TESTS AFTER FOAM ADDED FOR ISOLATED DEVICE

The maximum and minimum values of SWL-CoM classified by experiment type are given in Table 10-4.

TABLE 10-3 VALUES OF SWL-COM FOR THE ISOLATED DEVICE

	Small [mm]	Large [mm]	Multi [mm]	Irregular [mm]	Survivability [mm]
Minimum	622	669	648	657	662
Maximum	751	671	666	661	671
Range	129	2	18	4	9
Total range	49				

For the array, experiments were only conducted after the extra buoyancy foam had been added and so the SWL-CoM values are more consistent over the tests as shown in Figure 10-4. For the array, the sinking was less than 10 mm per experiment group as summarised in Table 10-5.

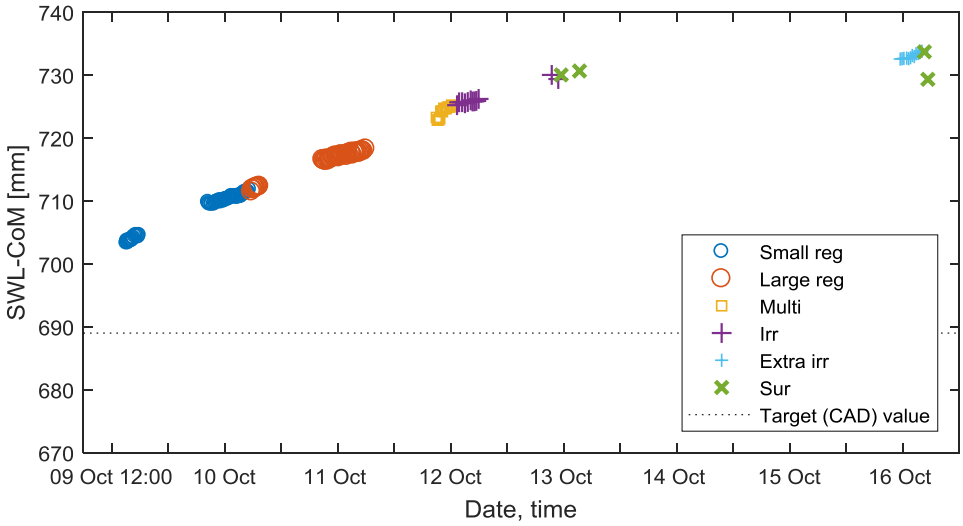

FIGURE 10-4 VARIATION IN THE DISTANCE BETWEEN THE STILL WATER LINE (SWL) AND THE CENTRE OF MASS (COM) FOR THE ARRAY EXPERIMENTS

10.2.1 Draught and waterline placement

During testing, the isolated device and the array of devices were both seen to change their position in the water. This was caused by water ingress; water entered small gaps within the model walls, which led to the sinking of the models up to the point at which the model was saturated. The assembly of the base unit was changed in light of this, so the change in draught was reduced for the array compared to the isolated device. In both cases, this was mitigated by attaching additional foam to the device: around the base for the isolated device and around the central array supports for the array in order to achieve the desired draught.

The maximum and minimum values of SWL-CoM classified by experiment type are given in Table 10-4 for the isolated device and in Table 10-5 for the array.

TABLE 10-4 VALUES OF SWL-COM FOR THE ISOLATED DEVICE

	Small [mm]	Large [mm]	Multi [mm]	Irregular [mm]	Survivability [mm]
Minimum	622	669	648	657	662
Maximum	751	671	666	661	671
Range	129	2	18	4	9
Total range	49				

For the array, experiments were only conducted after the extra buoyancy foam had been added and so the SWL-CoM values are more consistent over the tests as shown in Figure 3-2. For the array, the sinking was less than 10 mm per experiment group as summarised in Table 10-5. Typically, the minimum value of the SWL-CoM occurred at the start of the experimental

session and the maximum occurred at the end, indicating that the model was sinking over time.

TABLE 10-5 VALUES OF SWL-COM FOR THE ARRAY

	Small [mm]	Large [mm]	Multi [mm]	Irregular [mm]	Irregular bonus [mm]	Survivability [mm]
Minimum	712	718	725	730	734	734
Maximum	703	711	723	725	733	729
Range	8	7	2	5	1	4
Total range	22					

The point of examining the SWL-CoM value and the sinking of the models is to allow the results from the experiments to be reported and interpreted in light of them. For the isolated model, the range of SWL-CoM values was 129 mm during the small regular waves, indicating that this needs to be taken into account when examining the CWR. As such, all the isolated device experiments are plotted in such a way that the SWL-CoM value can be seen.

For each of the devices, the performance was quantified using the capture width ratio, CWR. The incident resource used for the calculations of CWR took data from a point up-wave[2] of the arrays measured in an empty basin. The decision to use empty basin test was based on not wanting to include the effects of the arrays themselves in the measurement. Had the devices been in the basin, the measurements would have included the reflected and radiated waves produced by the devices and so would not be representative of the incident wave field. Removing the reflections from the data using a method such as that described in [18] was considered but it would not have been possible to distinguish between waves emanating from the devices and those reflected from the basin's own spending beach. The amount of reflected energy from the beach is frequency dependent but is typically no more than 10% in the majority of the parameter space tested in this work [19]. As reported in [20], empty basin data is considered appropriate for heaving devices, however as both the arrays' devices moved by considerable amounts during experimentation, a fixed point measurement will represent a compromise. Thus, the exact values of the CWRs should be treated with caution and only used for general analysis.

Despite the uncertainty in the measurement of the CWRs, the power generated by each array was normalised by the same conditions, and so the performance differences between the configurations may be assumed to be real.

10.3 Motions of the spar buoy devices

[2] This should have been done with a gauge placed at the location of the device rather than up-wave. While the values would change by a small amount by using a gauge at the location of the device this would only be by a small amount and does not change any of the general trends or any of the conclusions drawn.

10.3.1Isolated compared with Configuration A

The surge response for the isolated device and central device within the individually moored array was the same, within the limits of repeatability, the same. For nearly all frequencies, the all surge motions were smaller than the incident wave motion (RAO<1) and in general, as the wave frequency increased, the surge RAO decreased.

The sway RAOs, Figure 10-5, show that sway motions were much smaller than the incident wave amplitudes, which is expected since there should be no wave motion along the sway axis. With RAO values and wave amplitudes so small, the results approached the limit of the motion tracking system and so only reporting general trends may be appropriate. The isolated device appeared to sway less with increasing frequency, while the central device seemed to have a more constant response with frequency.

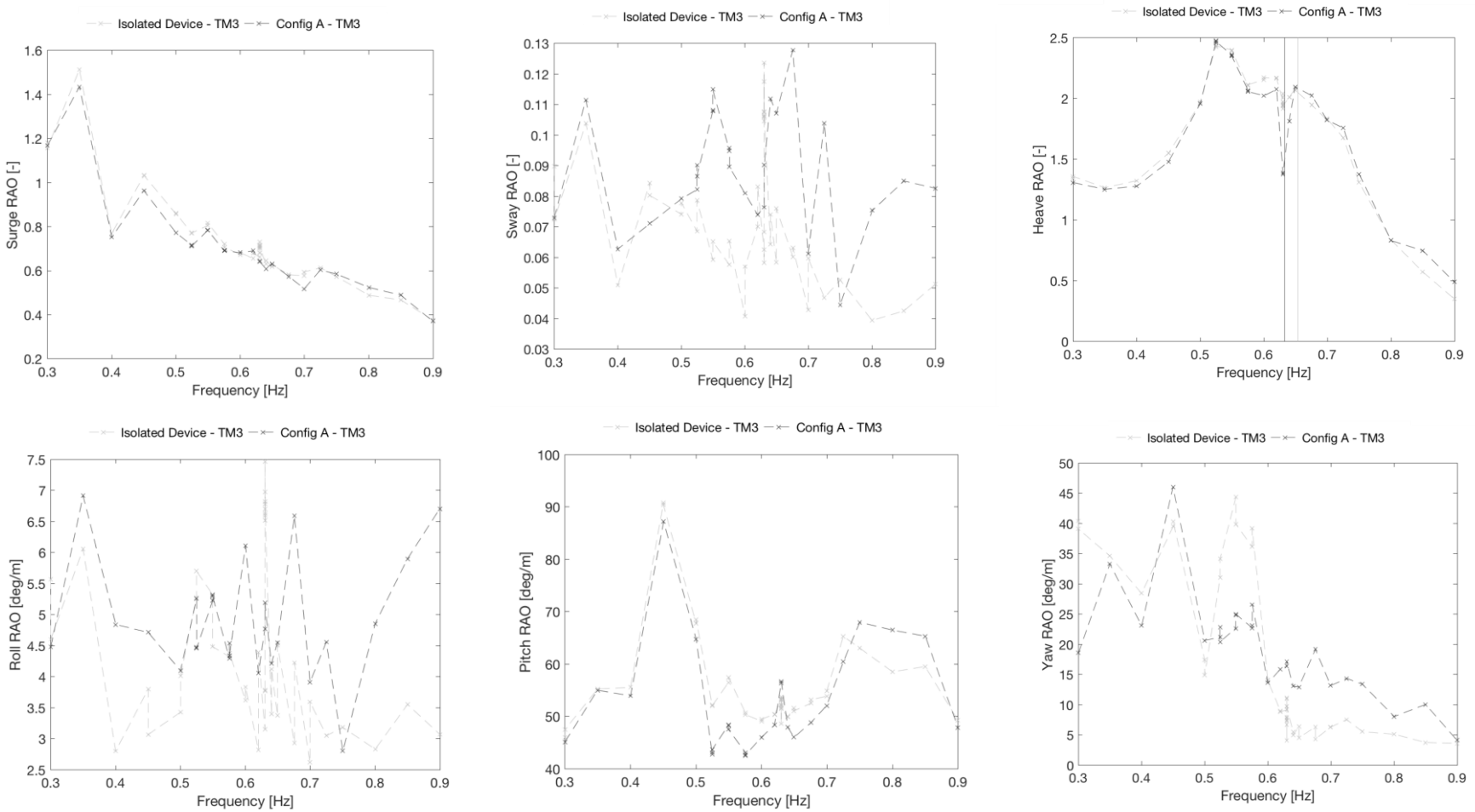

FIGURE 10-5 RAOS FOR THE ISOLATED DEVICE AND FOR THE CENTRAL DEVICE (TM3) IN THE INDIVIDUALLY MOORED ARRAY (CONFIGURATION A)

To compare the array configurations, devices were separated into two groups: the inner device in the array (central device, TM3) and the outer devices (TM1, TM2, TM4, TM5). Owing to TM1 moving in and out of the calibrated motion tracking region, its motion uncertainty was too great to be used. The motions of the inner device and the average motion of the outer devices (ignoring TM1) are plotted in Figure 10-6.

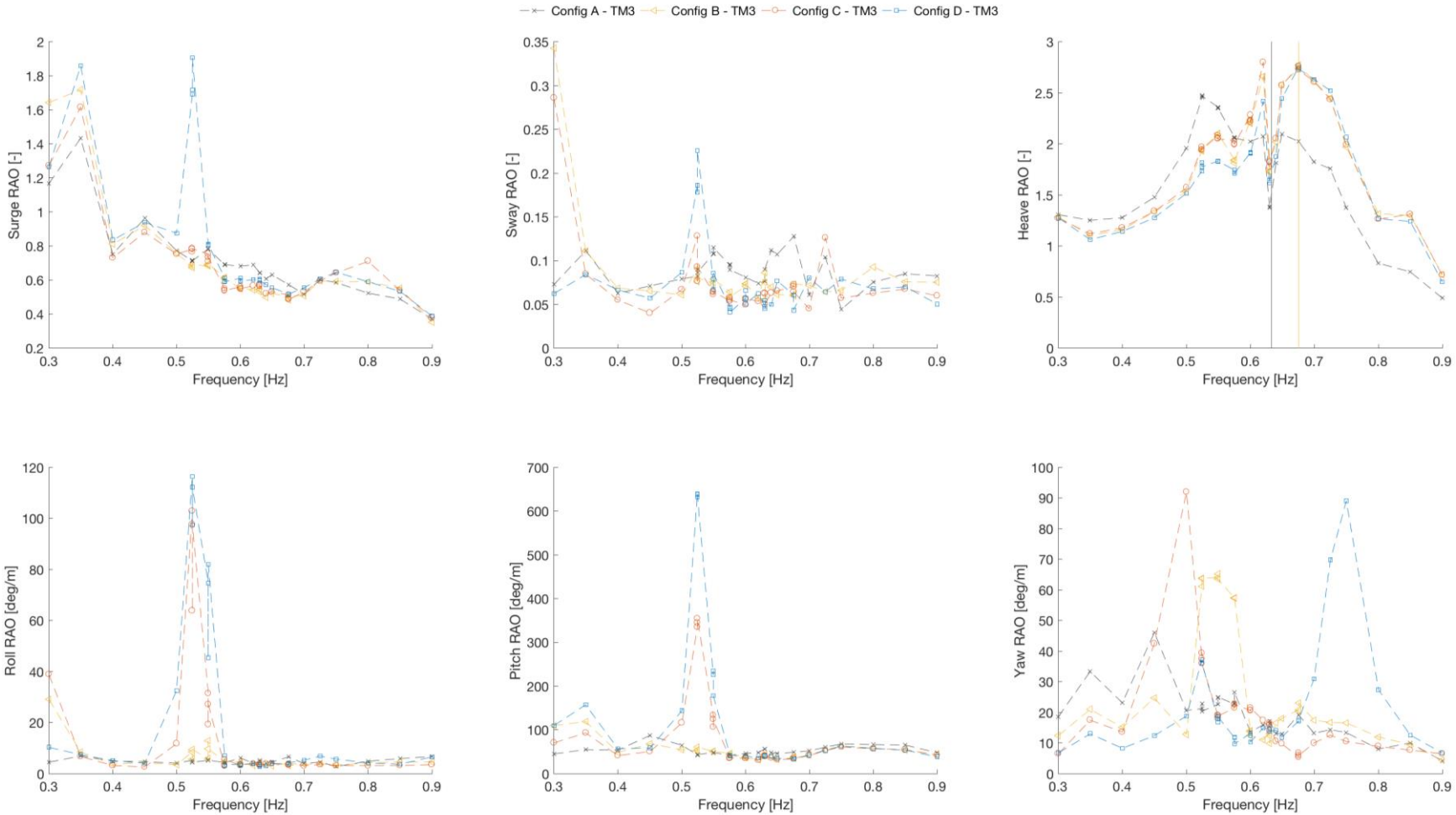

FIGURE 10-6 TIME-DOMAIN RESPONSES OF THE CENTRAL DEVICE, TM3, FOR REGULAR WAVES OF CONSTANT HEIGHT (*H* = 0.05 M)

A discrete Fourier transform was used to examine the motions in the frequency domain. As mentioned on page 31, energy was found in the surge, heave and pitch motions at frequencies lower than the incident wave frequency. Figure 10-7 shows the results for the central device (TM3) for each array configuration. The magnitude of the response, represented by the colour, shows that a constant surge response is noticed in all the configurations at around $f = 0.2$ Hz, becoming magnified as more interconnecting lines are removed. This is a low-frequency mean drift of the moorings. The peak of this response was around 0.2 Hz, which was close to the pitch and roll natural frequency of the device. At this point, the incident wave frequency was approximately three times the pitch natural frequency.

In the pitch response of Configurations C and D for TM3, there was a clear low-frequency response with a large magnitude compared to the motion at the wave frequency. This response was larger in Configuration D, in which the perpendicular interlinking lines were removed (see Figure 2-6 on page 9) allowing the devices to pitch and roll more easily, than in Configuration C. The outer devices had similar responses albeit with smaller magnitudes than that of the central device since without seabed lines, the central device was less constrained in pitch than the outer devices. This highlights a key outcome of the regular tests: the design of the interconnecting lines is extremely influential as coupled resonances have been shown to have very large effects on the non-linear motion of the devices.

The time series of the Configuration D pitch motion indicated that the pitch response was not stationary but increased in magnitude over time. Further testing is necessary to investigate the long-term pitch and roll responses.

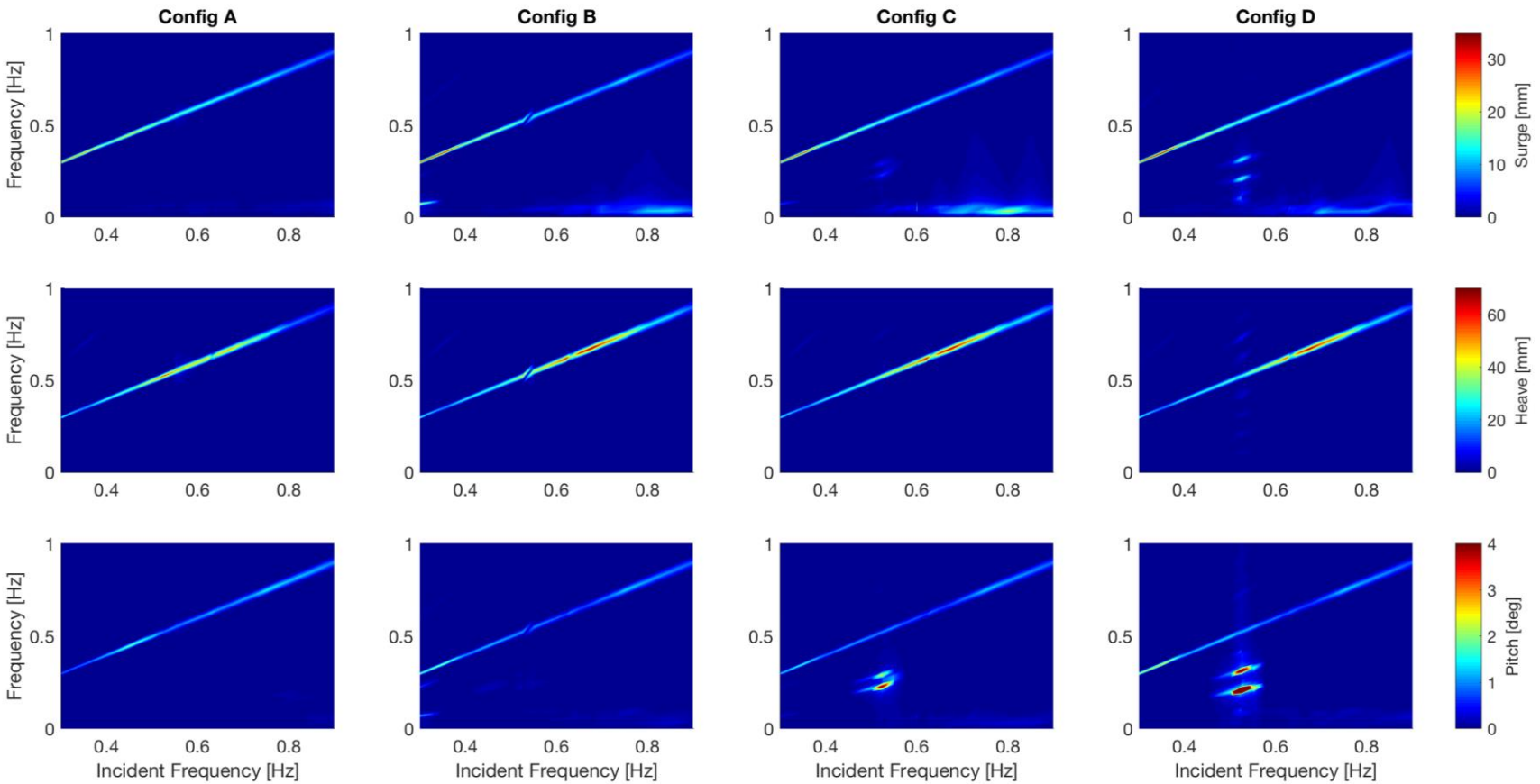

FIGURE 10-7 FREQUENCY-DOMAIN RESPONSE OF THE CENTRAL DEVICE, TM3, IN REGULAR WAVES OF CONSTANT HEIGHT (H = 0.05 M)

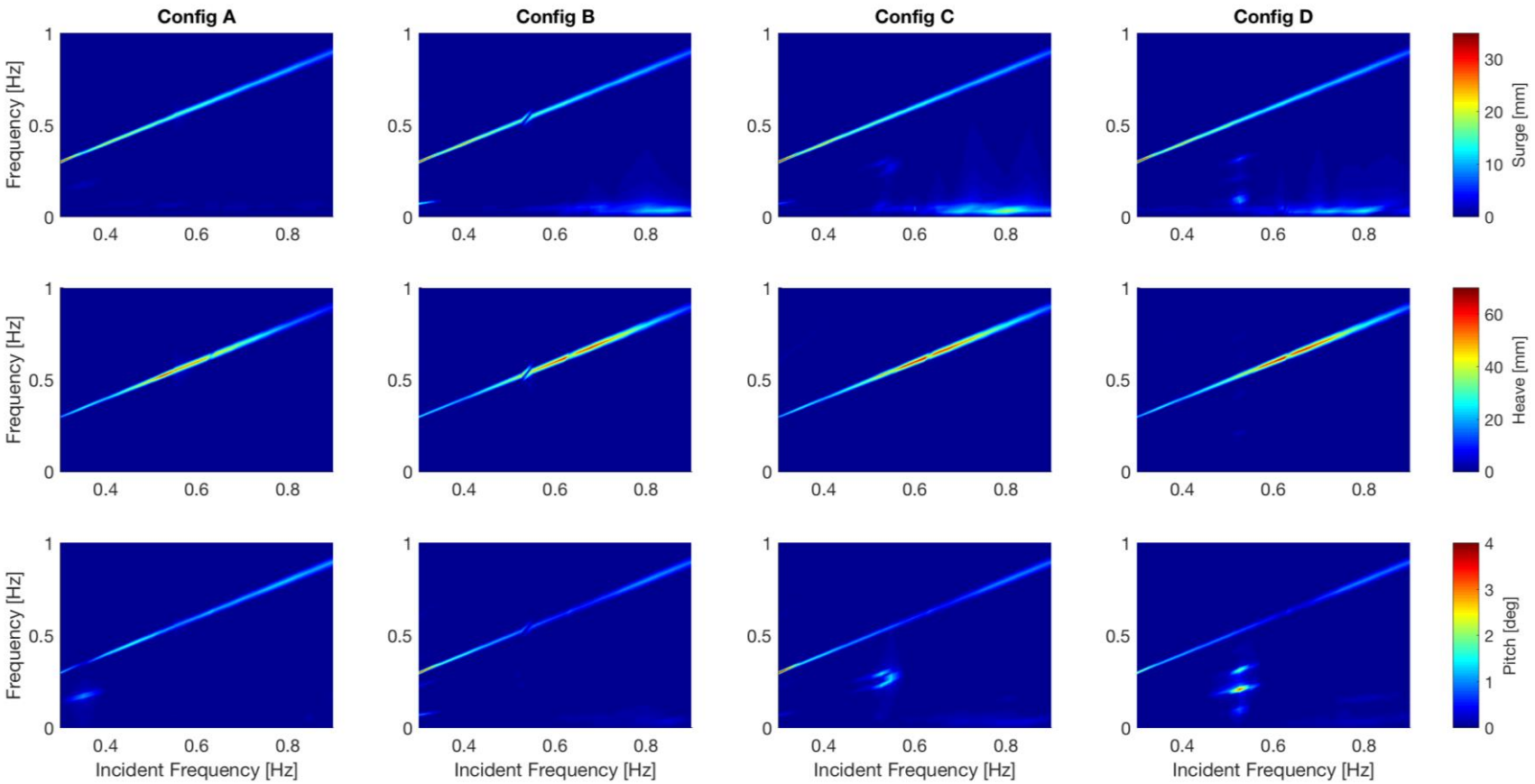

FIGURE 10-8 FREQUENCY-DOMAIN RESPONSE OF THE CORNER DEVICE, TM2, FOR REGULAR WAVES OF VARYING INCIDENT WAVE FREQUENCY AND CONSTANT AMPLITUDE (H = 0.05 M)

Figure 10-9 shows the RMS motion RAOs for TM2 and Figure 10-10 shows the range of RAO motions for TM3. A very clear difference between the interconnected and individually moored cases can be seen in the heave response of TM2, Figure 10-9. The spatial differences in the heave response appear to be very similar for all cases, linking to the similar power outputs for all the interconnected cases. The interconnected cases seem to all have a similar heave response that is greater than the individually moored case in all the irregular cases tested. These correlates well with the CWR curves, knowing that the device performance is closely linked to the heave response. The heave response of the isolated device is nearly identical to the average heave response of Configuration A.

Between the interconnected cases Configurations B and C seem to behave very similarly in all modes of motion with comparable averages and similar spatial variations. This suggests that moving from a double bottom mooring line to a singular one does not have significantly affect the motions of arrays.

For the case of T_p = 1.93 s, a slight decrease in average heave and an increase in pitch is noticed, relating to the drop in performance with respect to the other configurations. It appears from Figure 10-10 that the homogeneity of the array motions is inversely proportional to the number of interconnections as shown by the increase in shaded area as connections are removed.

In all modes of motion the shaded areas suggest that an individually moored array behaves more homogeneously than interconnected cases, where the magnitude of the motion in question varies spatially across the array.

There is a very noticeable difference between the interconnected and individually moored cases with regard to the surge response. The interconnections significantly reduce the constraint in surge in all the irregular cases tested.

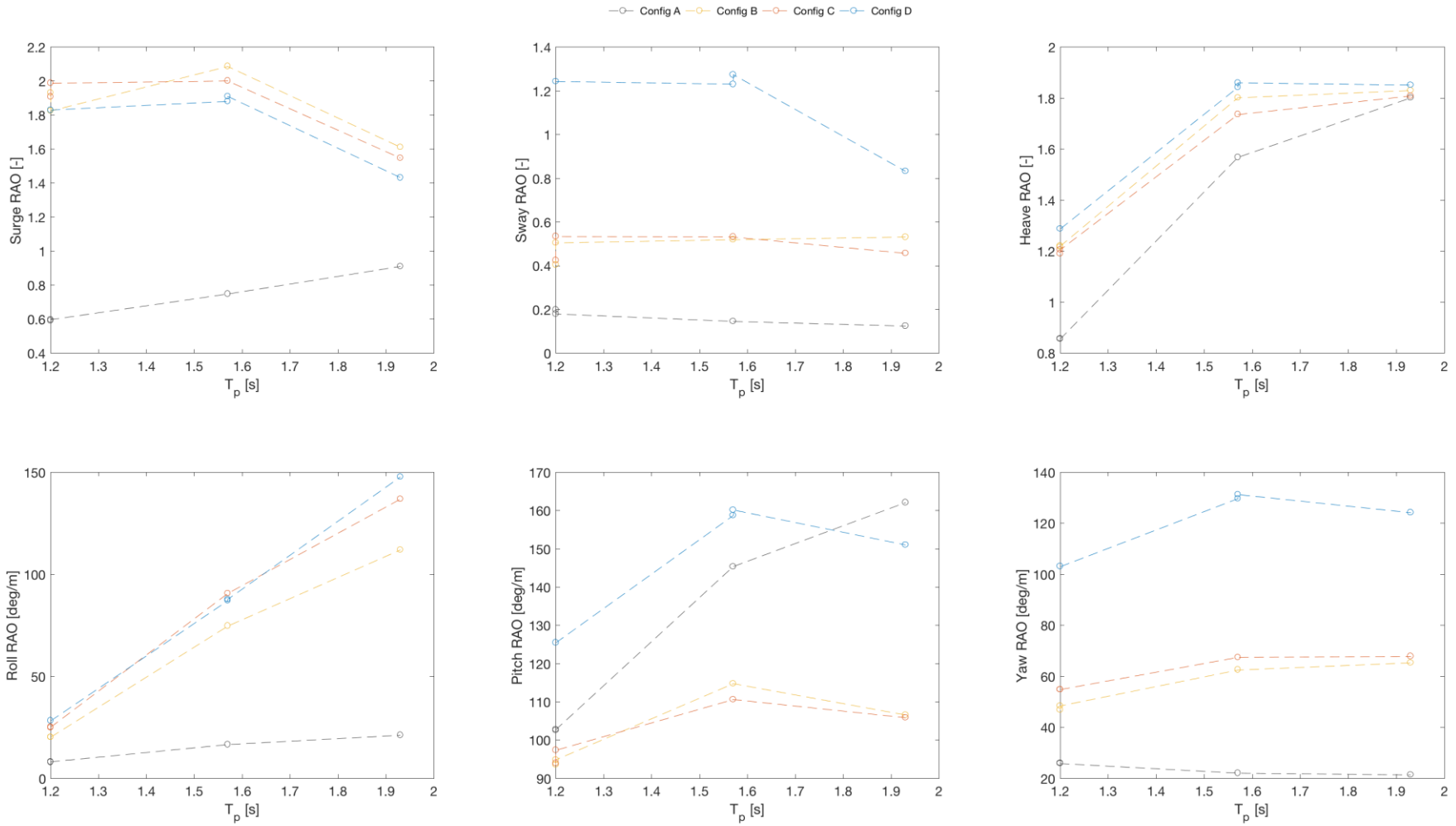

FIGURE 10-9 ROOT MEAN SQUARE MOTION RESPONSES OF TM2 IN IRREGULAR SEA STATES OF CONSTANT H_S = 0.05625 M

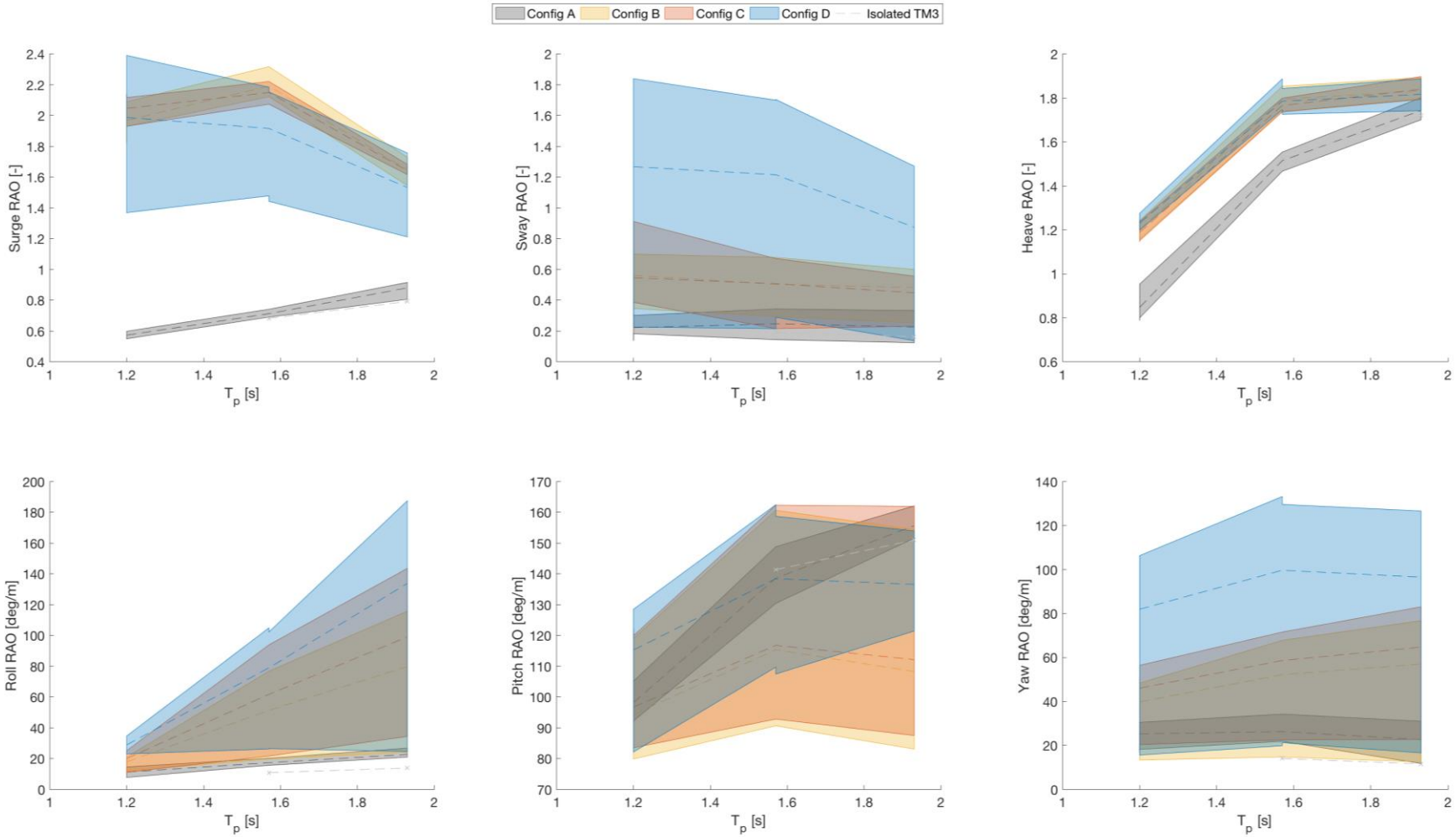

FIGURE 10-10 ARRAY MOTION RESPONSES SHOWING THE MEAN (DASHED LINES) AND THE MAXIMUM AND MINIMUM DISPLACEMENT (SHADING) FOR THE CENTRAL DEVICE (TM3)

10.4 Loads

Figure 10-11 shows the loads on the mooring line that had the most up-wave anchor point (line 3c, see Figure 2-6 or Section 8). It can be seen from Figure 10-11 that there was very little difference between the cyclic tension response of the most up-wave mooring line for the isolated case and the central device of Configuration A. This suggests that the similar seabed mooring lines could be utilized regardless of the intended placement of the device (within a compact array or an isolated case). A reduction in the tension was evident around f = 0.63 Hz, particularly for Configuration A. This links to the reductions in performance and motion response seen in previous sections and are linked to the basin resonances that are excited by the width of the array and the basin.

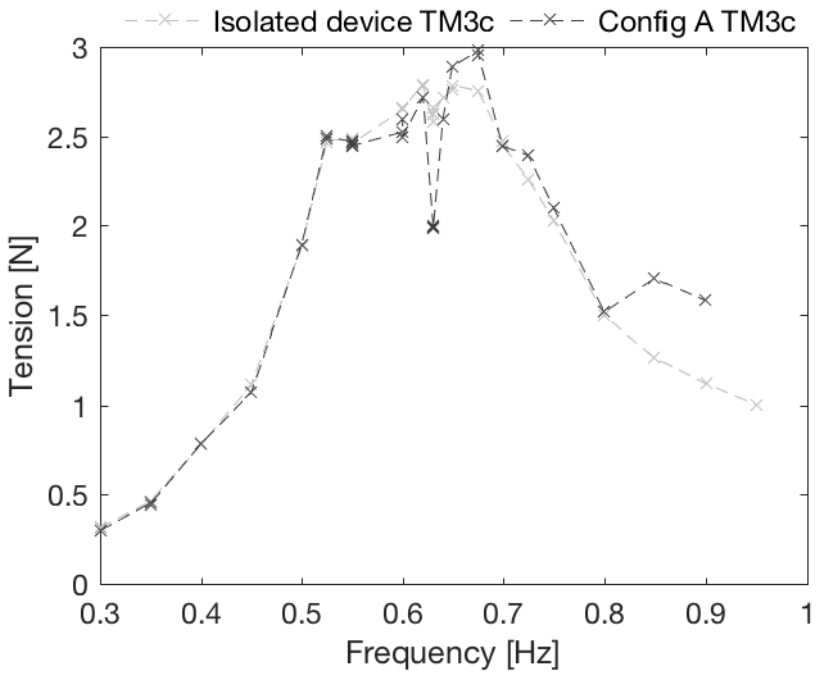

FIGURE 10-11 AMPLITUDE OF CYCLIC TENSION RESPONSE OF THE MOST UP-WAVE MOORING LINE TO REGULAR WAVES OF VARYING FREQUENCY AND CONSTANT AMPLITUDE

At higher frequencies, f > 0.8 Hz, the central device of Configuration A had slightly larger cyclic tensions compared to those of the isolated device. Linking the tensions back to the motion responses of the devices, shown in Figure 3-15 in the main body of the report and in Figure 10-5 on page 83, it does not appear that the surge motion contributed substantially to the cyclic tension in the front line. As one might expect, the pitch and heave responses appeared to be the main contributors to the cyclic tension; the heave response for Configuration A increased in a similar manner at the higher frequencies.

Table 10-6 shows the average cyclic tension of the front-most line for the isolated device and for the individually moored configuration; the presence of the other devices within the array

made little difference to line tension of the central device, with differences up to 0.5 N, or around 2% across all extreme cases.

TABLE 10-6 CYCLIC LINE TENSION FOR THE FRONT-MOST SEABED LINE OF THE ISOLATED TM3 DEVICE AND CONFIGURATION A TM3 DEVICE

Return period/Configuration	Isolated	A
10 years	27.89	27.57
50 years	25.12	25.59
100 years	24.06	24.56

In comparison to the operational sea states, the magnitude of the array effects was around five times smaller for the extreme cases than the irregular ones. This may be because the larger motions of the devices dominated the load response and so array effects were masked or perhaps that the array effects that contribute to the line tensions are non-linear with respect to the incident wave conditions, so that they were not captured by the current analysis. Further testing would allow this phenomenon to be investigated.

10.5 Phase shift of waves

In order to check the phase difference postulation, one can assume that the surface elevation of the internal water column will be phase shifted by $\pi/2$ with respect to the internal cylinder pressure. To test this linear assumption, the orifice piston test rig can be used, as both the internal pressure and the piston position is known. The Fourier transform is taken of both the pressure and the piston displacement, subtracting the phase angles from the peak responses, as shown in Figure 10-12.

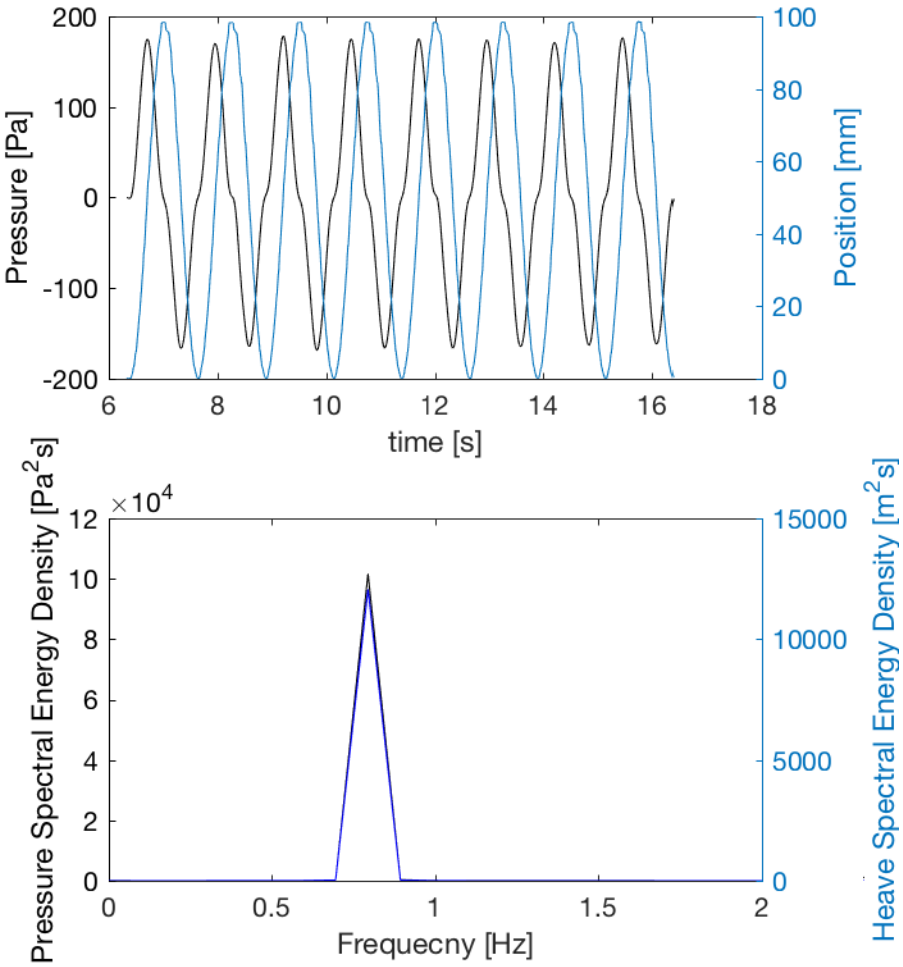

FIGURE 10-12 PHASE RELATION BETWEEN THE POSITION OF THE PISTON HEAD AND THE INTERNAL CHAMBER PRESSURE IN THE TIME AND FREQUENCY DOMAINS

Results from testing at five frequencies between 0.2 Hz and 1 Hz show that indeed the phase difference between the piston head and the pressure is close to π/2, with all results being within 2%. This shows the process to be relatively linear within the frequency space of the experiments. It is therefore acceptable to apply this phase offset to the measured pressure data in order to further analyse the phase difference between the device heave motion and the water column motion, with regard to the power output of the device. The same method has been used with data from the regular wave tests as explained above to obtain a prediction for the water surface level within the water column from the measured pressure data. The process was repeated to find the phase angle of the device heave response and the two were subtracted from one another. Thus, showing a phase difference between the water column and the device heave response, where one complete heave cycle is separated by a 2π phase difference.

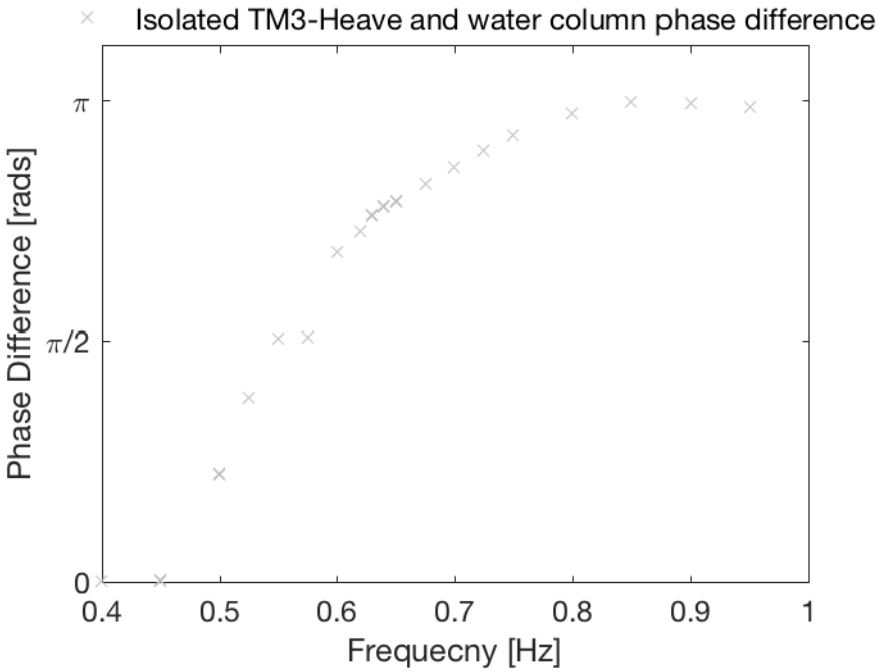

FIGURE 10-13 PHASE DIFFERENCE BETWEEN THE INTERNAL WATER COLUMN AND THE DEVICE HEAVE MOTION FOR AN ISOLATED DEVICE IN REGULAR WAVES OF VARYING FREQUENCY

It can be seen from Figure 10-13 that at the higher frequencies tested the phase angle difference between the water column and the device heave response is tending towards π. This is where the water column and the device heave is close to 180° out of phase, thus in a beneficial state for energy extraction. The resultant air passing through the turbine will be the volume of air associated to the device heave displacement *plus* the displacement of the water column. Conversely, at the lower frequencies tested, the heave of the device and the water column are nearly exactly in phase with one another. As a result, the only air being forced through the orifice is due to the heave of the device *minus* the height of the water column. As suggested above, it can be seen that the magnitude of the heave response between the individually moored and the interconnected arrays are not significantly different for the central device, Figure 3-19, and the outer devices Figure 10-6. However, the capture width ratios in Figure 3-16 do appear to be very different in magnitude. This is due to the frequency of device heave. It can be seen from Figure 10-13 that at the higher frequencies where the interconnected arrays show their peak heave response, the phase difference between the water column and the heave of the device is likely to be closer to 180° out of phase than at the frequency of the individually moored case. As a result, a larger volume of air is being forced through the orifice of the interconnected arrays than the individually moored case, thus resulting in a higher power output.

TABLE 10-7 LINE TENSION ROOT MEAN SQUARE DIVIDED BY SURFACE ELEVATION ROOT MEAN SQUARE. COLOUR CODING INDICATES THE MAGNITUDE OF THE CYCLIC LOADING PER CONFIGURATION.

	Return Period [years]	H_s [m]	T_p [s]	312	313	314	315	316	317	532	534	533
Config A	10	0.3	2.72	38.21	24.48	24.45	24.82	24.08	27.57	25.77	24.06	27.79
	50	0.325	2.91	40.92	22.90	22.25	22.62	22.71	25.59	23.49	22.50	25.49
	100	0.35	3.06	43.69	21.61	21.04	21.41	21.56	24.56	22.32	21.60	24.42
Config B	10	0.3	2.72	46.12	72.43	91.74	95.24	60.26	72.15	23.32	12.73	19.61
	50	0.325	2.91	44.93	67.57	93.55	98.76	53.09	63.96	20.24	12.85	19.01
	100	0.35	3.06	44.93	67.02	91.53	97.25	53.68	62.26	20.06	12.45	18.82
Config C	10	0.3	2.72	76.32	77.87	91.95	85.93	72.84	76.65	29.66	21.64	18.03
	50	0.325	2.91	73.69	75.80	91.28	84.56	72.00	68.89	24.54	20.80	21.04
	100	0.35	3.06	67.35	75.38	92.09	83.39	70.44	66.08	24.03	21.09	20.09
Config D	10	0.3	2.72	56.85	62.44	76.74	61.69	NA	77.39	57.38	31.38	NA
	50	0.325	2.91	53.35	63.14	72.85	57.51	NA	73.37	55.38	30.59	NA
	100	0.35	3.06	55.78	59.83	75.31	53.72	NA	75.76	61.29	31.33	NA